Frequency Combs for Spectroscopy and Optical Metrology

Md Imrul Kayes

Department of Electrical and Computer Engineering
McGill University
Montréal, QC, Canada

January 2019

A thesis submitted to McGill University in partial fulfillment of the requirements of the degree of Doctor of Philosophy

Abstract

Since their inception, optical frequency combs have created novel avenues for numerous applications such as molecular spectroscopy, atomic clocks, coherent communications, and microwave photonics. The future of frequency combs lies in exploring different comb generation technique, customized for specific applications. This thesis explores the synthesis of novel optical frequency combs in the near infrared wavelength region and the applications of such combs in the field of high-resolution spectroscopy and precise distance measurement. First, the generation of an electro-optic frequency comb with adjustable central wavelength and frequency spacing is experimentally demonstrated. This frequency comb is sourced from a single mode Brillouin fiber laser having an ultra-narrow linewidth that improves the overall phase noise performance of the comb spectral lines. A combined effect of electro-optic modulation, dispersion compensation, and fiber nonlinearity convert the continuous wave laser into a wideband optical frequency comb encompassing the C-band. Next, this frequency comb is used for a high-resolution distance measurement system that operates from the repetition rate modulation of the comb signal. The repetition frequency of the electro-optic comb is adjustable with a high dynamic range. Such broad tunablity of the repetition rate facilitates the measurement of distances with µm level precision. Such a system is also capable of motion tracking thanks to the rapid scan rate of the repetition frequency. Next, the application of electro-optic combs in high-resolution Fourier transform spectroscopy is demonstrated by measuring absorption lines of a chemical sample at 1.55 µm. The pulse train from a frequency comb, subject to a repetition rate modulation, stores the spectral response of a sample when sent to a length imbalanced interferometer. Such a system is equivalent to a dual-comb spectrometer but without the need for a complex phase matching mechanism.

Finally, a novel laser resonator is developed for high-resolution dual-comb spectroscopy at 1.9 µm. This resonator supports two counter-propagating laser oscillations sharing a common cavity which relaxes the phase matching requirement for dual-comb spectroscopy. A proof-of-concept experiment demonstrated the measurement of absorption lines of ambient water vapor with a 100 MHz resolution. This approach holds great promise for dual-comb spectroscopy in the mid-infrared region where many chemicals have strong fundamental transitions.

Résumé

Depuis leur tout début, les peignes de fréquences optiques ont pavé la voie à de nombreuses applications tel que la spectroscopie moléculaire, les horloges atomiques, les communications cohérentes ainsi que la photonique appliquée aux micro-ondes. L'avenir des peignes de fréquences se trouve dans l'exploration de différentes techniques de génération de peignes spécialisés pour des applications spécifiques. Cette thèse explore la synthèse de nouveaux peignes de fréquences optiques dans l'infrarouge proche, ainsi que les applications de ces peignes dans le domaine de la spectroscopie à haute résolution et la mesure de distances de haute précision. En premier lieu, la génération d'un peigne de fréquence électro-optique à longueur d'onde centrale ajustable et à espacement de fréquence est démontré expérimentalement. Ce peigne de fréquence provient d'un laser à fibre Brillouin monomode à bande très étroite qui permet d'améliorer la performance globale du bruit de phase des lignes spectrales du peigne. Un effet combiné de la modulation électro-optique, de la compensation de la dispersion et de la non linéarité de la fibre convertit le laser à bande continue à un peigne de fréquence optique large bande englobant la bande C des télécommunications. Par la suite, ce peigne de fréquence est utilisé pour un système de mesure de distance haute résolution qui opère à partir de la modulation du taux de répétition du signal du peigne. La fréquence de répétition du peigne électro-optique est ajustable avec une plage dynamique élevée. Ceci permet de faciliter la mesure de distances avec un niveau de précision de l'ordre du micromètre. Un tel système est également capable de suivre le mouvement grâce au taux de balayage rapide de la fréquence de répétition. En deuxième lieu, l'application d'un peigne électro-optique dans la spectroscopie haute résolution par transformation de Fourier est démontrée

par la mesure des lignes d'absorption d'un échantillon chimique à 1.55 µm. Le train d'impulsions d'un peigne à fréquence, sujet à la modulation du taux de répétition, contient la réponse spectrale d'un échantillon lorsqu'envoyé dans un interféromètre à bras asymétriques. Un tel système est équivalent à un spectromètre double-peigne sans le besoin d'un mécanisme d'adaptation de phase complexe. En dernier lieu, un nouveau résonateur laser est développé pour la spectroscopie haute résolution double-peigne à 1.9 µm. Ce résonateur supporte deux oscillations laser contre-propagatrices partageant une cavité commune. Cela permet d'assouplir l'exigence relative à l'adaptation de phase pour la spectroscopie double-peigne. Une preuve de concept a permis de démontrer la mesure des lignes d'absorption de la vapeur d'eau ambiante avec une résolution de 100 MHz. Cette approche s'avère très prometteuse pour la spectroscopie double-peigne dans l'infrarouge moyen où de nombreuses substances chimiques ont de fortes transitions fondamentales.

Dedication

I dedicate this thesis to my parents, Tasmina Akter and Golam Azam, who always inspired me to be a better person. Their dedication, hard work, and sacrifice made me who I am today. My studies from elementary to graduate school would not have been possible without their unconditional love, support, and sacrifice. They always inspired me to pursue a career in science, which fueled my ambition to become a scientist one day.

Acknowledgments

I want to thank my supervisor Prof. Martin Rochette for exceptional support, mentorship, and guidance. He offered me valuable feedback on the manuscript for which I am eternally obliged. I also want to thank my colleagues in the nonlinear photonics group for all the fun and lovely memories during my time here. I want to offer special gratitude to Dr. Nurmemet Abdukerim for many thoughtful insights for my experimental projects over the years. I also want to say special thanks to my colleagues in the photonics system group for their friendship and support. I want to acknowledge Prof. David Plant and Prof. Lawrence Chen for lending me many types of equipment over the years for my experiments. I want to thank Prof. Andrew Kirk and Prof. Odile Liboiron-Ladouceur for serving in my supervisory committee. I want to thank all my friends from Bangladesh and North America for cheering me every step of the way during this period. I want to offer my gratitude to my uncle, Capt. Mominul Hoq for his continual love and care since my kindergarten years. I thank my younger brother Fahad for his unconditional support during these last five years, especially for looking after my parents while I am away. Finally, I would like to thank my wife Moon for her love, care, and understanding during this most important period of my career. She also helped with some of the illustrations for this thesis for which I am grateful.

Table of Contents

List of Acronyms

BFL	Brillouin fiber laser
BPF	Band-pass filter
BW	Bandwidth
CW	Continuous wave
CNT	Carbon nanotube
DCS	Dual-comb spectroscopy
ECL	External cavity laser
EDFA	Erbium-doped fiber amplifier
EDF	Erbium-doped fiber
EO	Electro-optic
ESA	Electrical spectrum analyzer
FBG	Fiber Bragg grating
FSR	Free spectral range
FP	Fabry-Perot
FT	Fourier transform
FWM	Four-wave mixing
FWHM	Full-width half-maximum
HITRAN	High-resolution transmission molecular absorption database
HNLF	Highly nonlinear fiber
LIDAR	Light detection and ranging
MLL	Mode-locked laser

MPD	Maximum path delay
MZI	Mach-Zehnder interferometer
NIST	National Institute of Standard and Technology
OSA	Optical spectrum analyzer
OFC	Optical frequency comb
OSCAT	Optical sampling by laser cavity tuning
OSNR	Optical signal to noise ratio
PC	Polarization controller
RF	Radio frequency
SMF	Single-mode silica fiber
SNR	Signal to noise ratio
SCS	Single comb spectroscopy
SESAM	Semiconductor saturable absorber mirror
TOD	Tunable optical delay

List of Tables

List of Figures

Chapter I.

Introduction & Background

The development of frequency combs has been ongoing since 1970, thanks to a pioneering contribution by John Hall and Theodor Hansch [1]. Their remarkable works on laser stabilization and frequency comb synthesis made it possible to accurately determine the number of light oscillations per second leading to a frequency ruler that is million times more precise than previous spectroscopic measurement of wavelengths of light. Since then, frequency combs have completely transformed the field of precision laser spectroscopy by combining the field of ultrafast science, nonlinear optics, and optical frequency metrology. After that, frequency combs have found groundbreaking applications in the diverse fields of precision measurement, microwave photonics, coherent communication, and nonlinear physics. A stabilized mode-locked frequency comb has a frequency uncertainty below 10^{-9}, which outperforms the previous state of the art optical clocks based on atomic transitions [2]. Direct comb spectroscopy involves probing a sample directly with frequency combs, which provides better precision, acquisition time, and sensitivity with respect to incoherent light sources [3]. For remote sensing of greenhouse gases, frequency combs have shown excellent results with dual comb spectroscopy [4]. Frequency combs have also been used to synthesize high-quality THz microwave signal, especially mm-wave [5]. Due to having hundreds of spectral lines, frequency combs have the potential to replace traditional laser sources of coherent optical communication systems [6]. Furthermore, the phase coherence between comb lines makes such a system more effective for nonlinearity compensation in wavelength division multiplexing (WDM) systems using digital signal processing. Historically mode-locked lasers (MLL) have been the prime source of the optical frequency comb. However, frequency comb can also be synthesized by other techniques like difference frequency generation, optical parametric oscillation, Kerr comb generation, and electro-optic modulation. Each method comes with its own set of advantages and challenges depending on the application. Frequency stabilization of free-running frequency comb was a key to its early success in precision spectroscopy and optical metrology. However, complete stabilization of carrier envelop phase and repetition frequency requires complex electronic feedback systems which prevent its widespread use outside of lab environments. There are many less-demanding applications of frequency combs that do not warrant such complex stabilization scheme. This thesis is focused on such stabilization free frequency combs and their application in optical metrology and spectroscopy.

In this chapter, a brief background on the basics of frequency combs is presented, followed by a brief introduction of different comb generation technique. After that, relevant backgrounds on Brillouin scattering, optical sampling, Fourier transform spectroscopy are presented. Then, the main thesis contributions are listed, along with an outline of the thesis.

1.1 Basics of Frequency Combs

An optical frequency comb is composed of a series of equidistant narrow spectral lines in the frequency domain. There are two characteristics of a multi-wavelength source that qualifies it to be a frequency comb. First, in the spectrum, the frequency lines must be separated from each other by a constant frequency difference known as frequency pitch or repetition frequency (f_{rep}). Second, all the spectral lines must have a stable phase relationship with each other. In the case of MLLs, the frequency pitch or spectral separation between adjacent spectral lines are determined by the resonant cavity modes or free spectral range of the laser cavity. In the time domain, such combs produce a train of short optical pulses. Spectral lines of an optical frequency comb act like a spectral ruler, which means the frequency of any spectral component of the comb can be known by knowing f_{rep} and the order of comb line (*n*). For combs generated by mode-locked lasers, another parameter called carrier-envelop frequency offset (δ) should also be known. In the mode-locked laser cavity, due to dispersion, the carrier wave propagates with phase velocity, while the envelope propagates with the group velocity. Therefore, the peak electric field is shifted by a constant phase ($\Delta\Phi$) from the peak of the envelope, which translates into a carrier envelop offset frequency. So, the frequency of an arbitrary comb line is given by,

$$f_n = nf_{rep} + \delta \tag{1.1}$$

where δ is given by,

$$\delta = \frac{\Delta\emptyset}{2\pi} f_{rep} \tag{1.2}$$

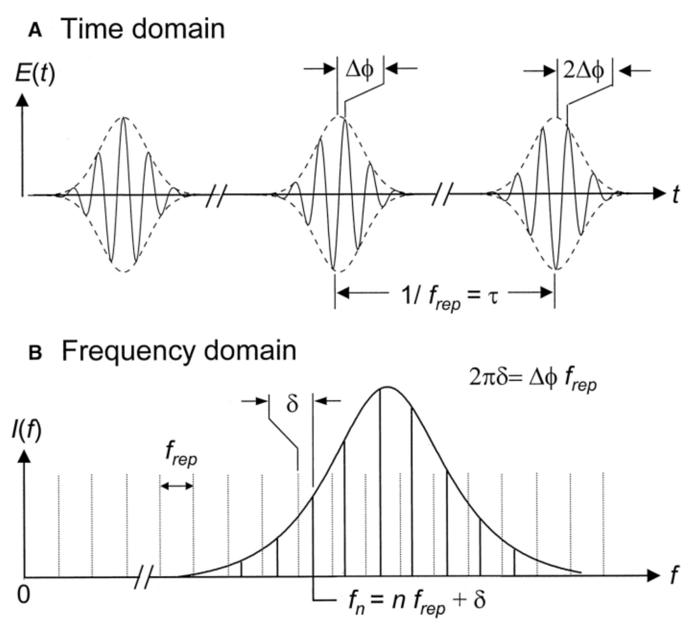

Figure 1.1. An optical frequency comb in both time and frequency domain [7].

1.2 Frequency Comb Synthesis

Since its advent, optical frequency combs are creating new avenues of application in different fields from optical communication to precision spectroscopy. Further extension of frequency comb generation technique with broader bandwidth and more power per spectral lines will be instrumental to the future development in this field. Furthermore, efficient generation of comb with a low frequency uncertainty at the near and mid-infrared region is very important for many applications, especially frequency comb spectroscopy. Because many molecules undergo a vibrational transition in this region.

Depending on the application and operational wavelength, several methods of frequency comb synthesis have been presented over the years. Every approach has its limitations and advantages. The most common techniques for comb synthesis are based on mode-locked lasers [8], difference frequency generation [9], optical parametric oscillation [10], and Kerr comb generation [11]. In the context of the research presented in this thesis, only mode-locking, and Kerr combs are discussed here.

1.2.1 Mode-locked Lasers

Mode-locked lasers are the most popular ways of generating frequency comb [12]. A strong optical field pumps a broadband gain medium in a resonator, and the cavity loss is periodically modulated to produce such mode-locked pulse sources. There are two ways to modulate the cavity loss, active and passive mode-locking. For active mode-locking, the loss is controlled externally using an electro-optic modulator in the cavity. In passive mode-locking, the loss is modulated by an in-cavity saturable absorber (SA) whose transmission is a nonlinear function of pulse intensity. Therefore, the SA suppresses the low power wings of a periodic pulse that leads to mode-locking operation with ultra-short pulses.

It is helpful to visualize the mode-locking resonator having an optical gate that periodically opens for a short amount of time synched with the cavity round-trip time. So, a CW signal passing through the gate experiences less loss at certain points of time leading to a steady build-up of a single pulse in the cavity. This circulating pulse outputs a steady pulse train when coupled out from the cavity. The inverse of cavity round-trip time sets its repetition frequency or free spectral range (FSR).

In the frequency domain, the mode-locking laser resonator contributes to many longitudinal modes that are separated by FSR of the cavity. Without any modulation of loss, power within the cavity builds up with pumping until gain saturates. When the round-trip gain equals the resonator loss, a few longitudinal modes start to lase, leading to a steady state CW operation. When a periodic loss modulation is introduced, many longitudinal modes can cross the lasing threshold leading to a stable frequency comb operation. Figure 1.2(a) shows the schematic of a mode-locked laser cavity.

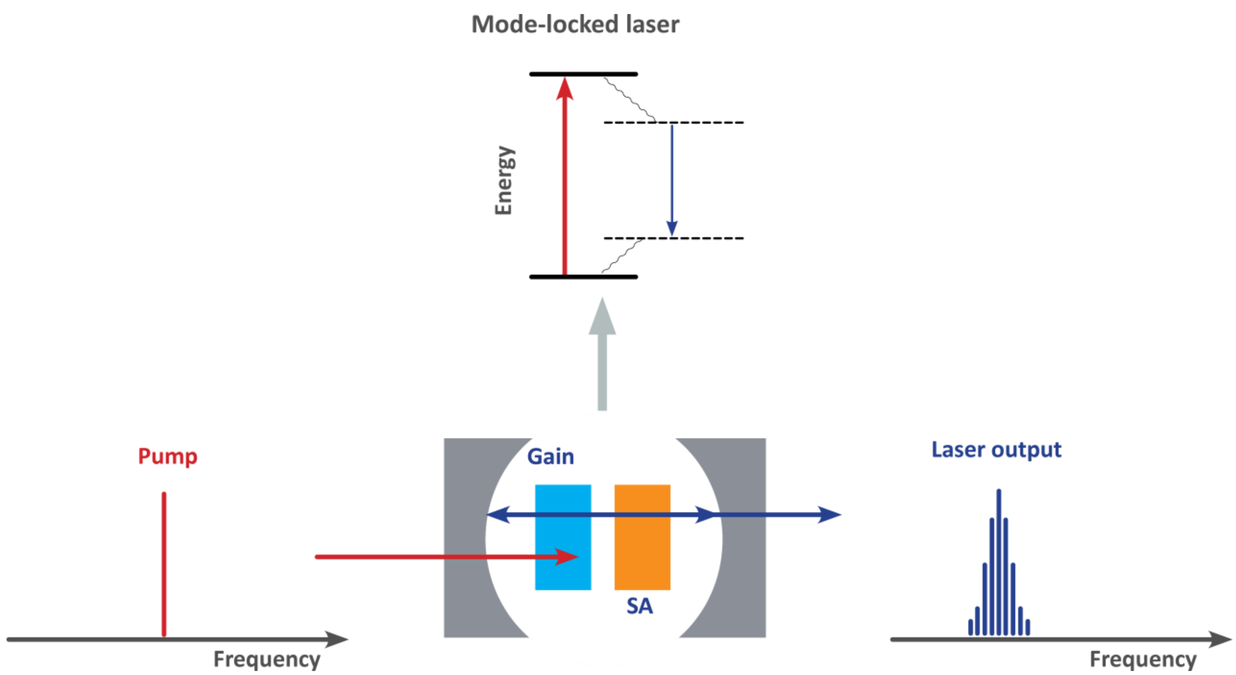

Figure 1.2. Principle of the mode-locked laser [13].

The Haus master mode-locking equation governs the behavior of an actively mode-locked pulse train [14].

$$\frac{1}{T_R}\frac{d}{dT}a(T,t) = (g-l)a(T,t) + \frac{g}{\Omega_g^2}\frac{d^2}{dt^2}a(T,t) - \frac{1}{2}M\Omega_m^2 t^2 a(T,t) \qquad (1.3)$$

Here a is the pulse envelop that depends on both a short-term time t and long-term time T that corresponds with the round-trip time. Ω_g is the gain bandwidth, g is the saturated gain coefficient, and l is the unsaturated loss of the cavity. The last term of equation (1.3) represents the mechanism for active modulation of resonator loss. M is the modulation depth, and Ω_m is the modulation frequency. For passive MLLs, the loss modulation function of the SA is given by [14],

$$s(t) = \frac{s_0}{1 + {I(t)}/{I_{sat}}} \tag{1.4}$$

where $s(t)$ represents absorption, s_0 is the unsaturated loss, and $I(t)$ is the time-dependent intensity. I_{sat} is the saturation intensity of the SA, defined by the optical intensity required to reduce the saturable absorption to half of its original value. The solution of equation (1.3) after incorporating the passive loss modulation function from equation (1.4) is given by,

$$a(t) = A_0 \operatorname{sech}\left(\frac{t}{\tau}\right) \tag{1.5}$$

where A_0 and τ are related to the amplitude and width of the pulse envelope, respectively. So, the power profile of a passively MLL pulse is expected to take on a $sech^2$ shape. The passive MLLs have a pulse-shaping effect as well, which is suitable for generating ultrashort pulses with high peak power. The choice of SA plays an important role in defining the output pulse characteristics. For ultrashort pulses, it is desirable to use a fast SA having a recovery time much shorter than intended the pulse width. For strong pulse shaping, it is desirable to have a high modulation depth, which is defined by the ratio between saturated and unsaturated loss.

Another important component of an MLL resonator is the gain medium which sets its operational wavelength. Different material like chalcogenide, thulium, and erbium can be used as the gain medium in near and mid-infrared [15]. The physical length of the resonator determines the repetition rate of an MLL. Therefore, the tuning range is very limited since changing the length beyond a limit may disrupt the cavity equilibrium and change the carrier wavelength. The resonator itself is very sensitive to outside disturbances. In a nutshell, the strict stability requirement of the laser cavity and less flexible frequency pitch tunability are two main limitations of such frequency combs.

1.2.2 Kerr Comb Generation

Kerr comb generation technique uses the Kerr nonlinear effect to produce a frequency comb. Kerr nonlinear effect involves self-phase modulation, cross phase modulation, and four-wave mixing (FWM). The FWM is a third order nonlinear effect ($\chi^{(3)}$) in an optical fiber [16]. It occurs when two different frequency components propagate together in a nonlinear medium. If the two input frequency components are f_1 and f_2 respectively, a refractive index modulation occurs at their difference frequency creating two additional frequency components f_3 and f_4 as follows,

$$f_3 = f_1 - (f_2 - f_1)$$
$$f_4 = f_2 + (f_2 - f_1)$$

The efficiency of the FWM process depends on the relative phases of the participating frequency components, making it a phase sensitive phenomenon [17]. By satisfying a phase-matching condition, its effect can accumulate over a long optical fiber. It usually happens if the frequency components are close to each other, and chromatic dispersion of the optical fiber has a flat profile.

There are two types of FWM process. When four different frequency components are interacting in an FWM process, it is called a non-degenerate FWM. On the other hand, there is a possibility that two of the four frequency components have the same frequency, which is called a degenerate FWM process. For example, a strong CW pump wave can give rise to a signal and an idler wave on both sides of its frequency under the degenerate FWM. The FWM mechanism is related to both the self-phase modulation and cross-phase modulation and differs only in terms of the degeneracy of the wave involved.

The FWM process can be described by pulse propagation for several fields ($i, k=1, 2, 3..$, $i \neq k$) leading to a set of coupled nonlinear Schrödinger equations [18],

$$\frac{\partial A_i}{\partial z} + \beta_{1i}\frac{\partial A_i}{\partial t} - \frac{j\beta_{2i}}{2}\frac{\partial^2 A_i}{\partial t^2} + \frac{\alpha_i}{2}A_i = -jn_2 k_i(f_{ii}|A_i|^2 + 2f_{ik}|A_k|^2) \quad (1.6)$$

where A is the electric field, β_1 is inverse of group velocity, β_2 is dispersion parameter, α is attenuation constant, n_2 is nonlinear index coefficient, k is the wavenumber, and f is the mode overlap integral. The last term in equation 1.6 describes the FWM interaction.

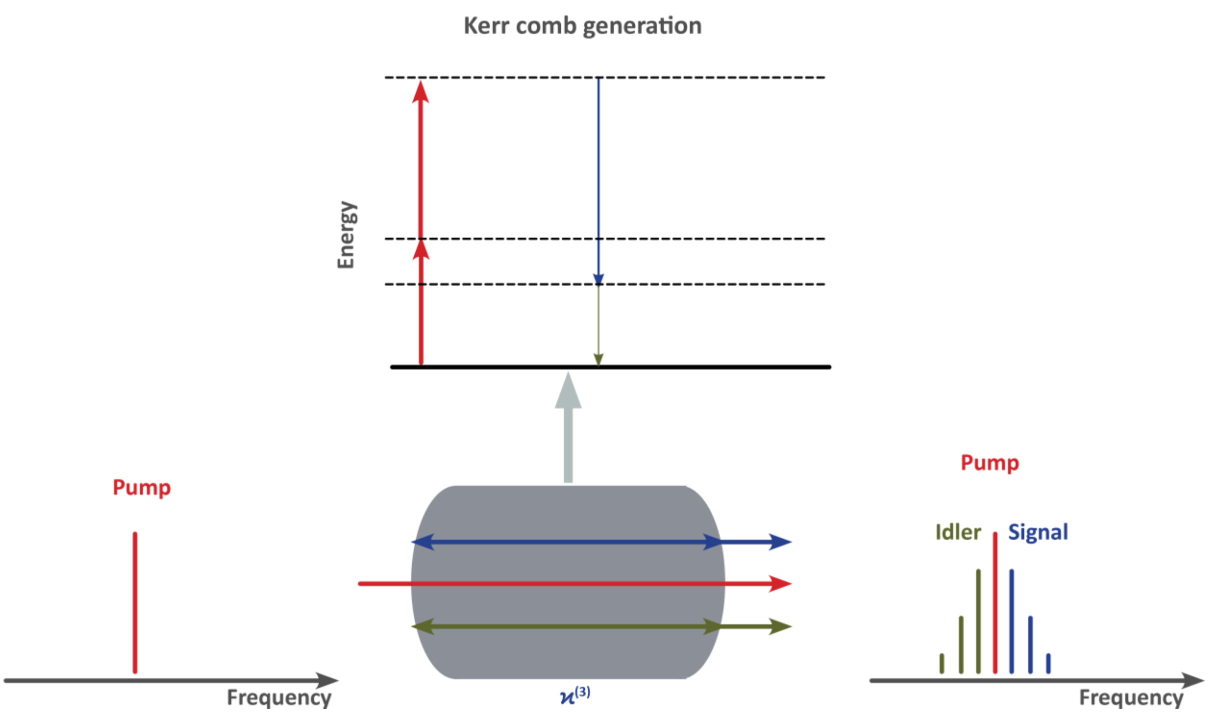

Figure 1.3. Generation technique of a Kerr frequency comb [13].

Kerr comb generation technique is shown in figure 1.3. The third order nonlinearity of the resonator gives rise to degenerate FWM by a strong CW pump field, which excites the nearby resonant cavity modes [16]. The signal and idler wave then initiates cascaded FWM in the cavity to generate a parametric frequency comb. If the finesse of the resonator is very high as in the case of micro-resonators, the threshold of such parametric processes remains very low. Also, the cascading non-degenerate mixing of the signal, idler and pump waves make sure that the generated spectral lines remain phase-locked automatically due to the FWM mechanism. If dispersion and nonlinearity induced phase shifts are appropriately balanced, this method can efficiently generate such wideband comb that can cover an entire octave [19]. This method generates frequency comb with high mode spacing, which has important applications in spectroscopy and optical metrology. Large mode separation also ensures high powers per mode, which in turns result in a high optical signal to noise ratio. Different micro-resonator based parametric comb has been demonstrated in the literature that uses whispering gallery modes of the cavity [20]. However, an all-fiber implementation of such an approach is limited due to the low Q factor of fiber-based cavity.

1.3 Electro-Optic Frequency Comb

A variation of the Kerr comb generation technique has been shown to generate frequency comb in the near infrared region. While the previously described process in figure 1.3 uses a third-order nonlinear media in a cavity to create a frequency comb, a cavity-less set up is also possible to effectively generate a wideband frequency comb. In a laser resonator, the physical length of the cavity needs to be changed to tune the repetition rate, which limits its tuning range. On the other hand, the cavity-free approach has been shown to produce hundreds of spectral lines for a frequency comb with a variable repetition rate [21]. This technique is known as frequency comb generation using parametric gain. Two CW lasers at near-infrared are used to produce a beating signal in the time domain. This beating signal is compressed by an optical fiber with anomalous dispersion to generate pulses. This pulse train then produces a non-degenerate FWM to generate frequency comb in a specially designed highly nonlinear fiber (HNLF) having zero dispersion at the wavelength of interest [22]. Figure 1.4 shows the block diagram for generating such frequency combs [23].

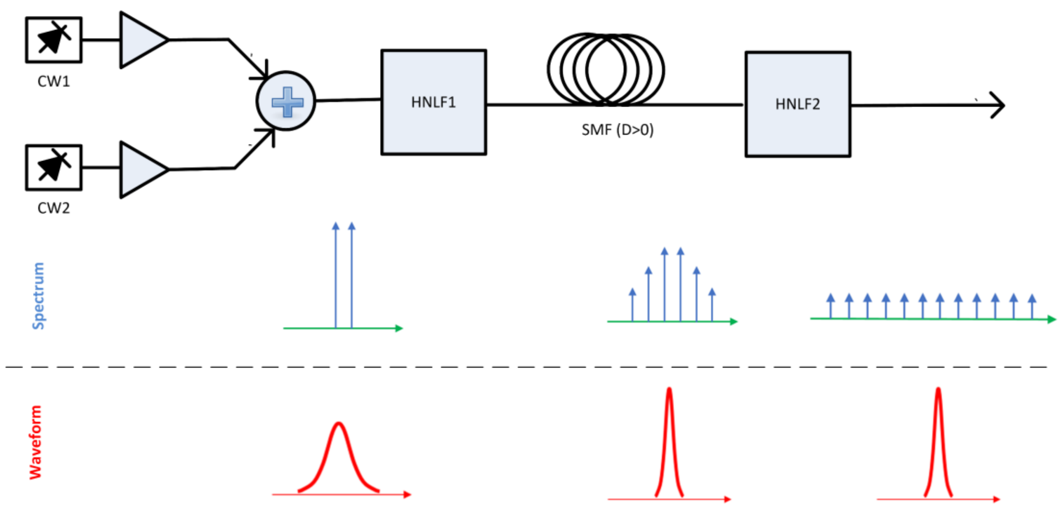

Figure 1.4. Multistage frequency comb generation from CW lasers. The beating signal between two injection-locked lasers is chirped and then compressed to generate a narrow pulse train. Efficient nonlinear mixing of this pulse train creates a wideband frequency comb.

The limitation of this approach is that there needs to be a stable phase relationship between the two CW lasers. It is achieved by a process called 'injection locking' that increases the complexity of the setup. Moreover, the repetition rate of such dual-pump seeded combs is on the order of ~100-200 GHz [22], unsuitable for applications in high-resolution spectroscopy. On the other hand, there is another approach that requires only one CW laser without the need for injection locking. This method uses the electro-optic (EO) effect to introduce phase and/or intensity modulation and generate phase-matched sidebands to seed the comb generation process [24]. This class of frequency combs is called electro-optic frequency Comb**,** which will form the central topic of this thesis. The repetition rate of such combs can range between 0.1-50 GHz [25] [26], making them suitable for a wide range of applications. Most of the works presented in this thesis are dedicated to the synthesis and application of such combs. A typical block diagram of an EO comb generation process is shown in figure 1.5. The setup consists of two sections, a pulse generation stage and a nonlinear mixing stage. The pulse generation stage converts the CW laser into a pulse train. After that, the signal undergoes nonlinear broadening in the nonlinear mixing stage. The working principle of such EO comb generation process is described below.

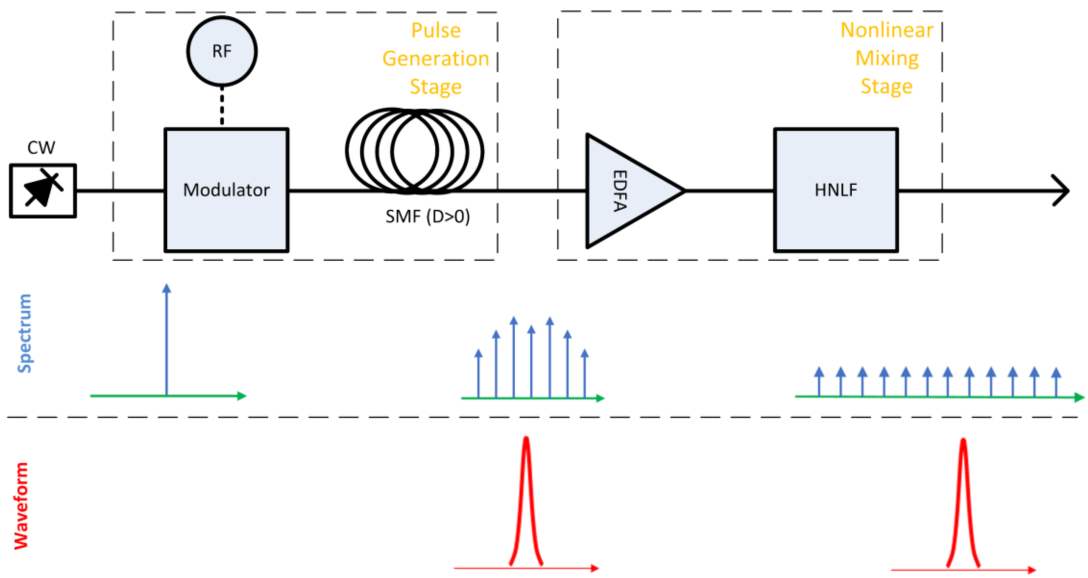

Figure 1.5. Schematics of EO comb generation setup. A combination of pulse generation and nonlinear broadening creates a frequency comb from a CW laser.

1.3.1 Pulse Generation stage

The analytical equation of a CW optical signal after phase modulation is given by,

$$S(0,t) = S_0\, exp\left[-j\pi\left(\frac{V_0}{V_\pi}\right) sin(2\pi f_m t)\right]$$

where f_m and V_0 is the frequency and peak driving voltage of the phase modulating RF signal, respectively. V_π is the half-wave voltage of the phase modulator, and S_0 is the electric field amplitude of the input CW signal. Phase modulation introduces a periodic variation in the signal phase known as frequency chirp. The instantaneous phase (θ) and chirp (C) of the modulated signal are given by,

$$\theta(t) = -\pi\left(\frac{V_0}{V_\pi}\right) 2\pi f_m cos(2\pi f_m t)$$

$$C(t) = \frac{d\theta(t)}{dt} = \pi\left(\frac{V_0}{V_\pi}\right)(2\pi f_m)^2 sin(2\pi f_m t) \qquad (1.7)$$

So, the phase modulation introduces both up (positive) and down (negative) chirp in the CW signal. The amount of chirp is proportional to the amplitude and frequency of the RF signal. The chirped signal is then sent to an SMF-28 fiber with length *L,* which introduces a chirp compensation by operating in the anomalous dispersion regime with a second-order dispersion parameter β_2. The part of the signal carrying up-chirp is compressed, and the part carrying down-chirp is stretched, leading to pulse formation. The repetition rate of such a pulse train is determined by the operating frequency of the EO modulator(s). The analytical expression of such a pulse in the frequency domain is given by,

$$\dot{U}(L,f) = \dot{U}(0,f)\exp(j\beta_2 L f^2)$$

The optimum chirp compensation occurs when the dispersion introduced by the fiber equals to the maximum chirp imposed by the phase modulator. Therefore, the optimum length (L_{opt}) of the fiber needed for the narrowest pulse train has to satisfy the following condition [24],

$$\frac{1}{\beta_2 L_{opt}} = \pi\left(\frac{V_0}{V_\pi}\right)(2\pi f_m)^2$$

$$L_{opt} = \frac{V_\pi}{\beta_2 \pi V_0 (2\pi f_m)^2} \tag{1.8}$$

Therefore, the optimum length of the fiber is inversely proportional to the frequency and amplitude of the RF signal. For a given length of dispersion compensating fiber and repetition frequency, the amplitude of the RF signal is estimated from equation 1.8. Moreover, higher RF frequency induces higher chirp in the CW signal, leading to narrower pulse train, and wider spectrum. The phase noise of the RF signal has to be negligible with respect to the phase noise of the CW pump laser. The frequency response of the phase modulator needs to be linear because nonlinear modulator imposes nonlinear chirp, which cannot be compensated properly with a standard SMF-28 fiber.

1.3.2 *Nonlinear Mixing Stage*

Narrow pulses, generated in the pulse generation stage, are amplified with a high-power optical amplifier and sent to an HNLF to initiate an FWM process to generate new frequency tones. HNLFs have a low dispersion slope and a zero dispersion wavelength close to the CW laser wavelength which satisfies the phase matching condition for the nonlinear mixing process. The high nonlinear coefficient of an HNLF also contributes to an efficient nonlinear broadening of the spectrum through both FWM and self-phase modulation. The self-phase modulation occurs when an ultrashort pulse modulates the refractive index of a medium by optical Kerr effect, which manifests as a phase shift of the signal [27].

The simulated temporal and frequency domain picture of the optical signal after the HNLF is shown below after solving the nonlinear Schrödinger equation described in equation 1.6 as per Appendix A.

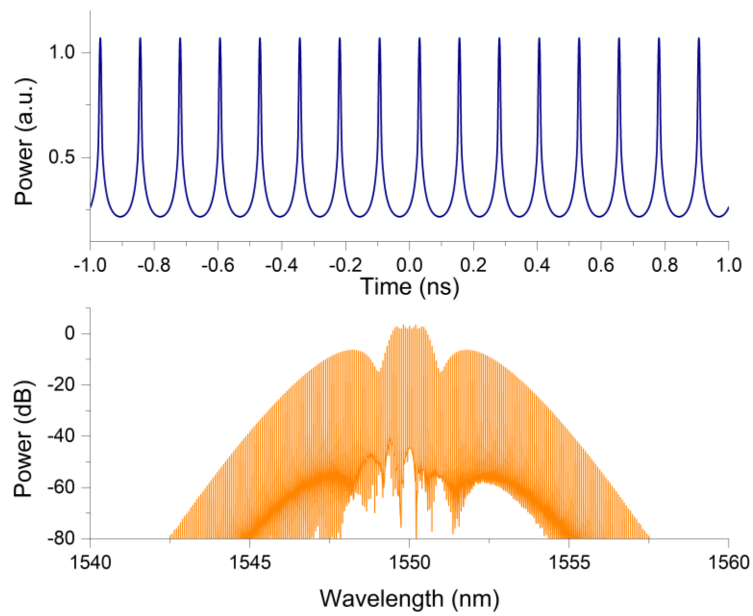

Figure:1.6. The simulated time domain and spectrum of an EO frequency comb generated after the nonlinear mixing stage.

Since there is no laser cavity involved, changing the repetition frequency of an EO comb does not affect the carrier wavelength, which is controlled by an external CW laser. Therefore, both the carrier wavelength and the repetition frequency of an EO comb are independently tunable.

These two independent degrees of freedom do not exist in an MLL.Unlike MLLs, EO combs have GHz repetition frequency, which increases the optical signal to noise ratio per spectral lines. The repetition frequency is tunable over a large dynamic range making it useful for application in optical metrology and spectroscopy using the OSCAT method. The tuning range of the repetition frequency is limited by the operating frequency range of the EO modulators. EO combs are easy to generate in the telecom wavelengths due to the availability of suitable CW laser and EO modulator. The nonlinear mixing process also induces a chirp on the comb signal via self-phase modulation with a nonlinear phase shift. Therefore, it is possible to increase the comb bandwidth by cascading multiple pulse generation and nonlinear mixing stages together. Compared to other frequency combs, EO combs are simple, robust, and less sensitive to environmental noises, which makes them ideal candidates for applications outside the laboratory environment.

1.4 Brillouin Scattering in Optical Fibers

Brillouin scattering is a third order nonlinear effect where an incident photon is converted into a backscattering photon of slightly lower energy [28]. The process of electrostriction is responsible for coupling the optical fields and acoustic waves. In optical fibers, this effect occurs spontaneously at low optical power resulting in back-reflection of forward propagating CW signal. The back-reflected signal is also known as the Stokes wave. At sufficiently high power above the threshold, most of the incident optical power is reflected backward by the spontaneous Brillouin scattering effect. The frequency of the reflected signal is slightly lower than that of the incident signal, which is determined by the frequency of the acoustic phonons. The difference in frequency between the incident and the reflected wave is called the Brillouin frequency shift (BFS). The BFS is determined by,

$$\nu_B = \frac{2n\nu_a}{\lambda} \tag{1.9}$$

where n is the group index of the medium, ν_a is the frequency of the phonon, and λ is the wavelength of the incident wave. For standard silica fibers, Brillouin shift has a typical value around 10-11 GHz at 1550 nm. The 3-dB bandwidth of the Brillouin gain spectrum is ~30 MHz, determined by the lifetime of the acoustic phonons.

1.4.1 Brillouin Fiber laser

It is possible to put a Brillouin gain medium in a ring resonator to create a Brillouin fiber laser (BFL), as shown in figure 1.7. Here, a high power CW laser is sending pump wave into a ring cavity through an optical circulator. A long optical fiber, HNLF is acting as the Brillouin gain medium which starts to backscatter the forward propagating pump after it reaches the threshold for Brillouin scattering. The backscattered Stokes wave circulates in the cavity and starts to lase, once the net gain of the cavity overcomes the loss. Because of low resonator loss and narrowband gain spectrum of the fiber resonator, BFL has a relatively low pump threshold for silica fiber at 1550 nm. The most useful property of a BFL is its ability to reduce the linewidth of the pump laser, as shown in the theoretical analysis of a BFL by ref [29]. The linewidth reduction ratio is given by,

$$\frac{\Delta\nu_{pump}}{\Delta\nu_{BFL}} = \left[1 + \frac{\pi\Delta\nu_B}{\tau_c}\right]^2 \tag{1.10}$$

where $\Delta\nu_B$ is the FWHM of the Brillouin gain spectrum, and τ_c is the cavity loss rate. Therefore, BFL is an excellent candidate for creating a spectrally pure laser source.

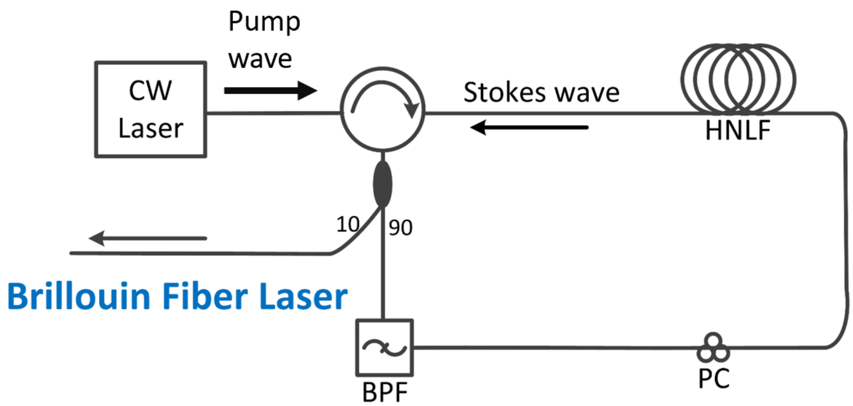

Figure 1.7. Schematic of a Brillouin fiber laser resonator. BPF: bandpass filter, PC: polarization controller, HNLF: highly nonlinear fiber.

1.4.2 Cascaded Brillouin scattering

Increasing pump power beyond the Brillouin threshold increases the power of the resulting Stokes signal. If the power of the back-propagating Stokes signal exceeds the threshold, it initiates a 2nd order Stokes signal in the forward direction. This process is called cascaded Brillouin scattering. It is possible to build a Brillouin laser operating over several Stokes orders. Since all the Stokes waves are phase matched, they interact with each other because of FWM and produce anti-Stokes waves at the lower wavelengths. The number of generated Stokes and anti-Stokes lines depends on the Brillouin threshold of the gain medium and the pump power. Figure 1.8 shows the experimental setup of a cascaded Brillouin laser cavity. Here, the Brillouin gain medium is placed with a mirror so that both the pump and 1st order Stokes propagates in the counter-clockwise direction in the ring resonator. A combination of stimulated Brillouin scattering and FWM creates a series of Stokes and anti-Stokes spectral lines separated from each other by BFS, ~10.86 GHz in case of the silica fiber at 1550 nm. Since all these spectral lines are phase matched, they form an optical frequency comb.

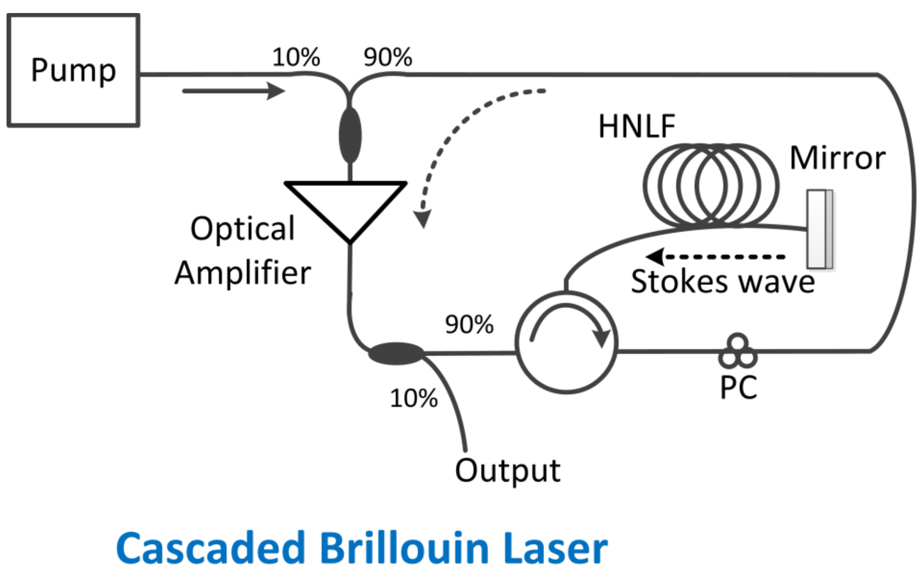

Figure 1.8. Schematic of a cascade Brillouin laser cavity.

Prior to the works presented in this thesis, the author demonstrated the synthesis of an optical frequency comb (OFC) using cascaded Brillouin scattering in a highly nonlinear fiber [30]. By leveraging the inherent phase relationship between the pump, Stokes, and anti-Stokes waves, a narrowband optical frequency comb was generated as shown in the experimental block diagram in figure 1.8. Figure 1.9 shows the experimental results for both time and frequency domain signal of the resulting frequency comb. However, the frequency combs by cascaded Brillouin scattering suffers from two serious drawbacks. First, the repetition rate is not tunable since the BFS of the gain medium determines it. Second, the spectral separations between the subsequent Stokes wave are not truly constant. According to equation 1.9, BFS is inversely proportional to the pump wavelength. Let us assume that, the wavelengths of the pump and 1st order Stokes wave is λ_p and λ_{s1} respectively. Now if the BFS for the 1st order Stokes is ν_{B1}, then the BFS for the 2nd order Stokes will be ($\nu_{B1}.\lambda_p/ \lambda_{s1}$). Therefore, a higher order Stokes line will have a less spectral separation between them comparing to a lower order Stokes line. These unevenly spaced spectral lines of such a frequency comb are unfit for applications in optical metrology and spectroscopy.

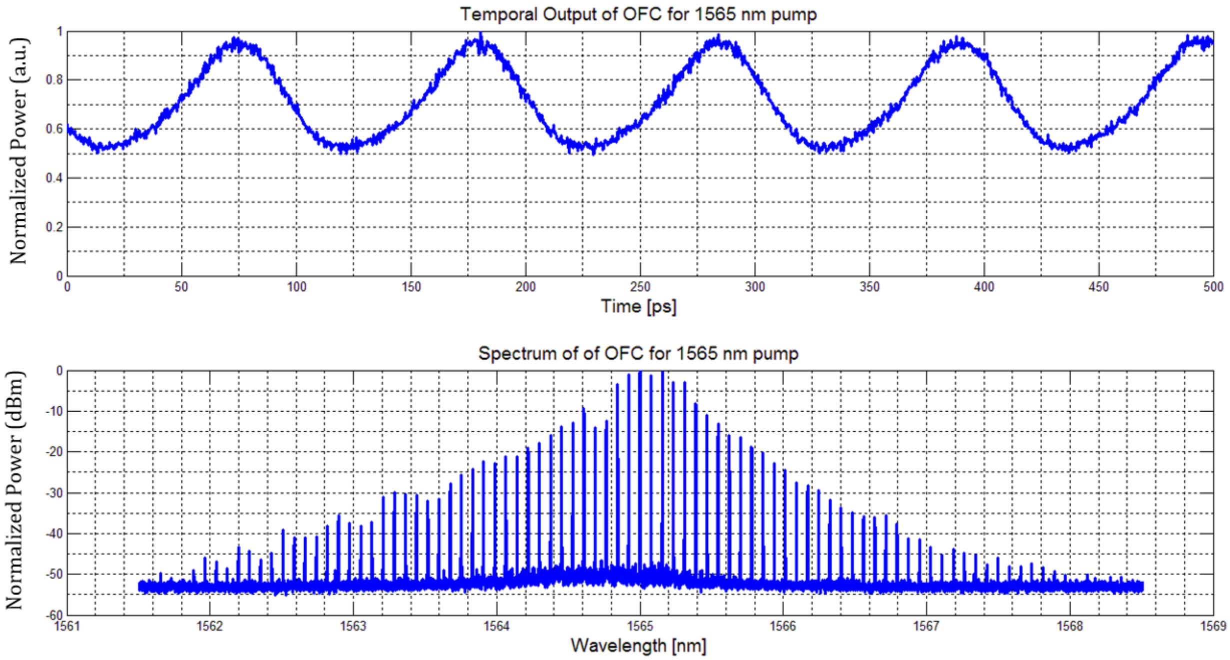

Figure 1.9. Time and frequency domain signal of the frequency comb generated from a cascaded Brillouin laser cavity.

1.5 Optical Sampling Theory

Autocorrelation of an optical signal in the time domain contains information about the amplitude and phase of its power spectral density function according to Wiener–Khinchin theorem [31]. Therefore, the autocorrelation technique is very useful for molecular spectroscopy and precise distance measurement. Autocorrelation of an optical pulse train can be easily achieved by sending it to an interferometer having a tunable optical delay (TOD) in one arm. By changing the effective optical path difference between the two arms of the interferometer, it is possible to generate autocorrelation trace of the signal under test by a method called optical sampling. To carry out high-resolution measurement of spectroscopy and optical metrology, it is necessary that the TOD has both a fast scan rate and broad scan range. Unfortunately, TOD modules are based on mechanical movement of a target mirror, incapable of achieving both the speed and the range [32].

In 2010, a novel scheme of optical sampling had been proposed, which overcomes the limitations posed by the tunable optical delay [33]. Here, pulses from an MLL is sent to an interferometer having a large length mismatch between its two arms. The repetition rate of the MLL pulse train is swept periodically, which creates a scan of the relative path difference between pulses traveling in both arms. Since the repetition rate of an MLL is changed by tuning the length of the laser cavity, this method is called optical sampling by laser cavity tuning (OSCAT). Figure 1.6 shows the working principle of this technique. The signal from a pulsed source is split into two paths, A and B. Signal traveling in path B experiences a relative delay concerning path A due to the presence of a pulse buffer (fixed optical delay line). The number of pulses in the delay line is a function of the period of the pulse train and length of the delay. Let us assume that the number is m. Then, signals from both paths are recombined with a 3-dB coupler and recorded with a photodetector. In this configuration, a reference pulse $i+m$ coming from path A will reach the detector at the same time as pulse i of path B, as shown in the figure. This is why a change of instantaneous repetition rate of the pulse train will introduce a relative path delay between these two pulses. Therefore, if the repetition rate of the pulse train is scanned from f_{rep} to $f_{rep}+\Delta f$, the maximum temporal offset between these two pulses at the photodetector is given by [33],

$$\Delta t = m\left(\frac{1}{f_{rep}} - \frac{1}{f_{rep} + \Delta f}\right) \tag{1.11}$$

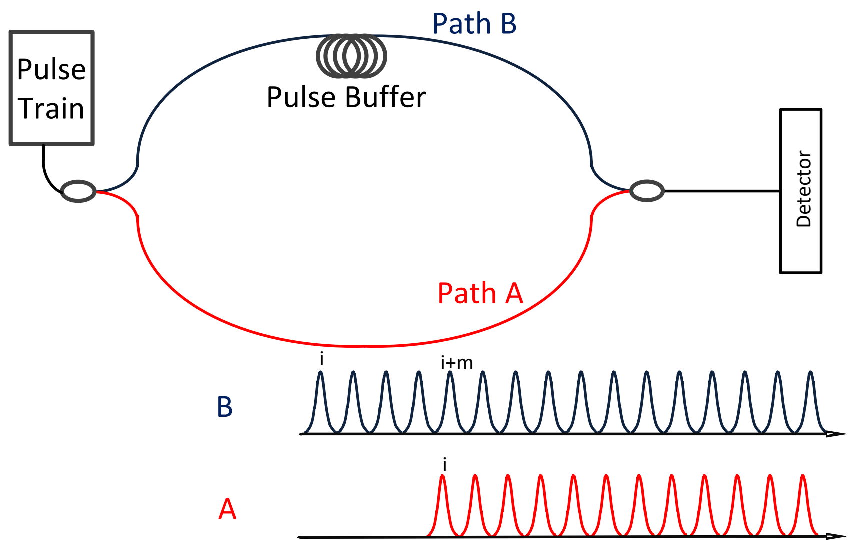

Figure 1.6. The principle of OSCAT theory.

So, a simple frequency scan can replicate the effect of a tunable delay line in the OSCAT method. It should be noted that the temporal offset scales with *m*. Therefore, a large temporal scan is possible with a short frequency scan overcoming the speed-range trade-off for a TOD based optical sampling [34]. To achieve an arbitrary temporal scan range ΔT, the length of the delay line needed for an OSCAT method is given by,

$$L = \frac{\Delta T . c_0 . (f_{rep} + \Delta f)}{\Delta f . n} \tag{1.12}$$

where *n* is the refractive index of the delay line, and c_0 is the speed of light in vacuum.

Most of the OSCAT based time-resolved experiments in the literature use MLLs as the pulse source. However, pulse train can be generated without a laser cavity, for example, with electro-optic frequency combs, described in section 1.3. In these cases, no cavity tuning is required to sweep the repetition rate of a pulse train. Therefore, a more appropriate name for OSCAT should be ‘optical sampling by sweeping repetition rate.’ However, in the remaining script, OSCAT shall be used interchangeably for both MLL and EO comb based optical sampling methods. The main advantage of EO-OSCAT technique is its broader dynamic range of f_{rep} sweeping, as listed in the following table.

The maximum dynamic range of f_{rep} sweep	Distance Measurement	Spectroscopy
MLL-OSCAT	3.5 kHz [35]	1 MHz [36]
EO-OSCAT	10-100 MHz	10-100 MHz

Table 1.1: Different dynamic range of repetition frequency sweep for OSCAT based methods.

The required dynamic range of OSCAT for a given application depends on the target resolution and measurement speed. The broader dynamic range of f_{rep} benefits all the OSCAT applications since it can achieve sufficient resolution with a shorter length mismatch in the interferometer, as described in section 3.2 and 4.2.

1.6 Fourier Transform Spectroscopy

Fourier transform (FT) spectroscopy is capable of recording broadband spectra of a sample without the need of a broadly tunable laser source. The essential components of an FT spectrometer are a polychromatic light source and an interferometer, followed by a photodetector, as shown in figure 1.7. The light coming from the source is divided into two paths and then combined at the output. One arm of the interferometer contains a scan mirror, which acts as a TOD. The optical path difference between the two arms of the interferometer is scanned continuously by moving the mirror position. Therefore, the superimposed signal at the output interferes constructively or destructively, depending on the instantaneous phase difference between the two arms. The output signal is called an interferogram. The intensity of the interferogram is a function of the mirror position (x), which is given by [37],

$$I(x) = \int_{-\infty}^{+\infty} S(f) \cos(2\pi x f) \, df \qquad (1.13)$$

where $S(f)$ is the optical spectrum of the light source. The frequency of the oscillation depends on the scan mirror velocity and the optical frequency of the input light source. Therefore, this process is capable of encoding the high optical frequencies in the form of low-frequency oscillation. This is why the bandwidth requirement of the photodetector of FT spectrometer is very low (~kHz). *I(x)* is only one half of a Fourier transform pair, where the other half is given by,

$$S(f) = \int_{-\infty}^{+\infty} I(x)\cos(2\pi f x)\,dx \tag{1.14}$$

Equation 1.13 and 1.14 show the relationship between the interferogram and the spectrum. Therefore, the spectrum of the light source can easily be retrieved by Fourier transforming the measured interferogram.

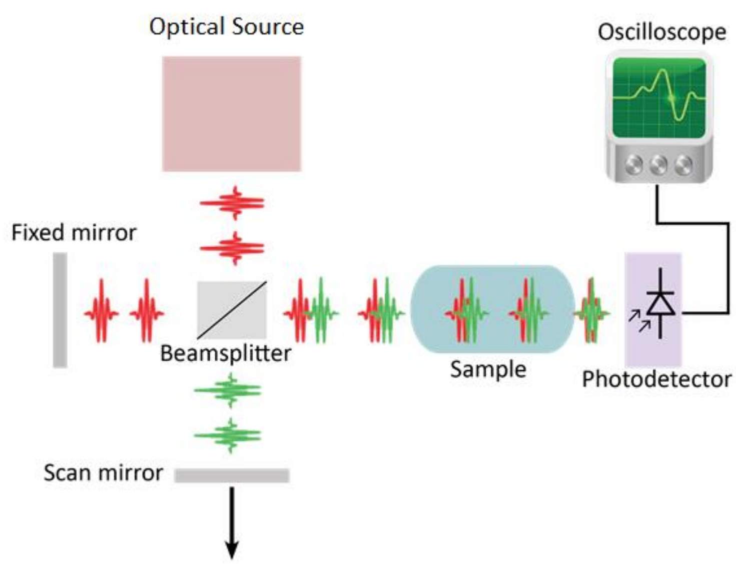

Figure 1.7. Schematic of a Fourier transform spectrometer.

The maximum scan range of the mirror determines the spectral resolution of an FT spectrometer, which has a typical value of ~nm. The scan velocity of the mirror determines the acquisition time of the measurement. Even though it is possible to increase the resolution by increasing the maximum mirror displacement, it is not as straightforward. Because a 5 GHz spectral resolution around 1550 nm would require a ~3 km long scan range [38]. Such a broad scan range imposes unrealistic scan velocity requirement even with an hour-long acquisition time.

Therefore, the traditional FT spectrometry suffers from two drawbacks, limited resolution and acquisition time [39]. Frequency comb based Fourier transform spectrometers can overcome these limitations, as discussed in chapter 4 and 5.

1.7 Main Contributions

The following summarizes the main contribution of this thesis. These contributions have been presented at international conferences and published in the form of journal papers except for chapter 3.

First, a technique to generate a wideband EO frequency comb has been demonstrated. The EO frequency comb shows excellent phase noise performance thanks to a Brillouin fiber laser that seeds the comb generation process.

Second, the application of an EO comb in optical metrology has been demonstrated by developing a high-precision distance meter. This meter is capable of measuring distances up to 200 m with ±5 µm accuracy with an acquisition time of 30 ms.

Third, a Fourier transform spectrometer has been developed that operates from repetition frequency modulation of an EO comb. This spectrometer is used to measure high-resolution spectra of an $H^{13}C^{14}N$ reference gas cell in the C band.

Finally, a novel Thulium fiber laser cavity has been designed to create a bi-directional mode-locked laser at 1.9 µm. The two OFCs originated from the cavity have a passive mutual coherence due to common mode noise rejection. These free-running combs are then used to perform high-resolution dual-comb spectroscopy without phase stabilizing mechanism for measuring absorption lines of ambient water vapors.

1.8 Outline of the Thesis

The main goal of this thesis is to synthesize optical frequency combs and apply them in optical metrology and spectroscopy. The thesis is organized as follows:

- Chapter 2 presents the synthesis of a wideband EO comb from a single-mode Brillouin fiber laser using electro-optic modulation and parametric gain of highly nonlinear fibers. Following the general description of the Brillouin fiber laser cavity, it details the construction of a compound ring cavity to ensure a single longitudinal mode operation. The operation of a fiber Fabry-Perot filter and Sagnac loop interferometer combination to suppress many longitudinal modes in the Brillouin gain spectrum is experimentally demonstrated. Then, the characterization of the ultra-narrow linewidth of the Brillouin laser by a modified self-heterodyne method is described that shows a linewidth reduction of the pump laser by a factor of 16. After that, the steps to convert a CW Brillouin laser to a frequency comb using EO modulation, chirp compensation, and nonlinear mixing are detailed. The experimental results containing the time and frequency domain signals of the OFC are presented showing 10-ps pulse train and 32-nm spectral bandwidth. Finally, the linewidth characterization of the comb signal is described showing spectral preservation of the seed laser in the comb generation process.

- Chapter 3 presents the application of an EO comb for high precision distance measurement. The operating principle of distance measurement by repetition rate modulation of a pulsed laser coupled to a length-imbalanced interferometer is described in detail. The advantages of an EO comb over an MLL as the pulsed laser source are explained with theoretical analysis, and additional improvements of the measurement algorithm are proposed. Following the schematic and description of the experimental setup, this chapter presents the results showing a measurement accuracy of 5 µm and a dynamic range of 200 m. The motion tracking of a moving object by the proposed method is also described, showcasing its potential in the field of light detection and ranging (LIDAR).

- Chapter 4 presents the operation of a Fourier transform spectrometer near 1550 nm, enabled by repetition rate modulation of an EO comb. Using the same principles of optical sampling described in chapter 3, it details the formation of spectrum sensing interferogram that originates at the output of a length imbalanced interferometer due to pulse walk-off.

Then, the advantages of the proposed method over dual-comb spectroscopy and MLL-based method are explained. Following the schematic and description of the experimental setup, this chapter describes the process of obtaining the spectral response of a chemical sample from an interferogram. The results show the measurement of high-resolution absorption lines of an $H^{13}C^{14}N$ reference gas cell between 1533-1541 nm. The obtained spectra are verified by comparing them with the HITRAN database.

- Chapter 5 describes the operation of a bi-directional Thulium laser for dual-comb spectroscopy to detect ambient water vapor at 1.9 um. Following the theory of dual-comb spectroscopy, it details the advantage of the two MLLs sharing the same cavity to overcome its stringent phase matching condition for high-resolution spectroscopy. The novel design of the bi-directional laser cavity is described along with the resulting spectra of the dual-comb signal. Then, the schematic of the dual-comb spectroscopy experiment is described, which captures the series of interferogram after the bi-directional laser signal passes through a water vapor sample. The algorithm for the processing interferograms to obtain high-resolution spectral response is described. Finally, the experimental results showing narrow absorption lines of water are shown, which matches well with the HITRAN database.

- Chapter 6 summarizes this thesis and suggests some future works in some related areas.

List of Publications

Relevant journal publications

- **M. Imrul Kayes** and Martin Rochette, “Optical frequency comb generation with ultra-narrow spectral lines,” Optics Letters 42(14), 2718-2721 (2017).

  Contributions:

  M. Imrul Kayes: Formulated the concept, performed experiment and prepared the manuscript

  Martin Rochette: Prepared the manuscript and supervised the project

- **M. Imrul Kayes** and Martin Rochette, “Precise distance measurement by a single electro-optic frequency comb," Photonics Technology Letters 31(10), 775-778 (2019).

  Contributions:

  M. Imrul Kayes: Formulated the concept, performed experiment and prepared the manuscript

  Martin Rochette: Prepared the manuscript and supervised the project

- **M. Imrul Kayes** and Martin Rochette, “Fourier Transform Spectroscopy by Repetition Rate Sweeping of a Single Electro-Optic Frequency Comb,” Optics Letters 43(5), 967-970 (2018).

  Contributions:

  M. Imrul Kayes: Formulated the concept, performed experiment and prepared the manuscript

  Martin Rochette: Prepared the manuscript and supervised the project

- **M. Imrul Kayes,** Nurmemet Abdukerim, Alexandre Rekik, and Martin Rochette, “Free-Running Mode-Locked Laser Based Dual-Comb Spectroscopy," Optics Letters 43(23), 5809-5812 (2018).

  Contributions:

  M. Imrul Kayes: Formulated the concept, performed experiment and prepared the manuscript

  Nurmemet Abdukerim: Bi-directional laser cavity design

  Alexandre Rekik: Bi-directional laser cavity optimization

  Martin Rochette: Prepared the manuscript and supervised the project

- Nurmemet Abdukerim, **M. Imrul Kayes,** Alexandre Rekik, and Martin Rochette, "Bidirectional mode-locked thulium-doped fiber laser," Applied Optics 57(25), 7198-7202 (2018).

  Contributions:

  Nurmemet Abdukerim: Formulated the concept, performed experiment and prepared the manuscript

  M. Imrul Kayes: Performed experiment

  Alexandre Rekik: Laser cavity optimization

  Martin Rochette: Prepared the manuscript and supervised the project

Relevant conference publications

- **M. Imrul Kayes** and Martin Rochette, "Optical Frequency Comb Generation via Cascaded Brillouin Scattering in a Nonlinear Media," at Photonics North, Nonlinear-4-29-6, Ottawa, Ontario, June 2015.

  Contributions:

  M. Imrul Kayes: Formulated the concept, Performed experiment and prepared the manuscript

  Martin Rochette: Prepared the manuscript and supervised the project

- **M. Imrul Kayes** and Martin Rochette, "Low noise frequency comb generator," at Photonics North, Nonlinear-10-6, Québec city, Québec, May 2016.

  Contributions:

  M. Imrul Kayes: Formulated the concept, performed experiment and prepared the manuscript

  Martin Rochette: Prepared the manuscript and supervised the project

- **M. Imrul Kayes** and Martin Rochette, "Fourier Transform Spectroscopy via a Single Electro-Optic Frequency Comb," at IEEE Photonics Conference, WH3.5, Orlando, Florida, Oct 2017.

  Contributions:

  M. Imrul Kayes: Formulated the concept, performed experiment and prepared the manuscript

  Martin Rochette: Prepared the manuscript and supervised the project

- **M. Imrul Kayes,** Nurmemet Abdukerim, Alexandre Rekik, and Martin Rochette, "Dual Comb Spectroscopy with Free-Running Bidirectional Mode-Locked Laser at 1.9 μm," in Conference on Lasers and Electro-Optics, SW4L.6, San Jose, California, May 2018.

Contributions:

M. Imrul Kayes: Formulated the concept, performed experiment and prepared the manuscript

Nurmemet Abdukerim: Bi-directional laser cavity design

Alexandre Rekik: Bi-directional laser cavity optimization

Martin Rochette: Prepared the manuscript and supervised the project

Chapter II.

Low Noise Optical Frequency Comb Synthesis

[1]In this chapter, we demonstrate the synthesis of an electro-optic frequency comb source that generates 500 ultra-narrow spectral lines with a spectral linewidth of 1.5-3 kHz, spanning over the C-band. The source originates from a single-mode Brillouin laser processed with phase modulation, pulse compression, and four-wave mixing. As a result, the narrow linewidth of the Brillouin laser improves the phase noise of every spectral line of the frequency comb.

2.1 Introduction

Of particular interest for coherent optical communication systems, OFCs play an important role when locked on a single phase reference [40]. In this context, it is desirable that the phase noise, and the associated spectral width of the in-phase spectral lines, is kept to a minimum to ensure minimizing the bit error ratio of channels corrected by digital signal backpropagation [41] [42].

[1] The content of this chapter has been subjected to publication in **M. Imrul Kayes** and Martin Rochette, "Optical frequency comb generation with ultra-narrow spectral lines," Optics Letters 42(14), 2718-2721 (2017).

On top of that, OFCs with low phase noise should also improve the signal to noise performance of other frequency comb applications such as spectroscopy, sensing, microwave synthesis, optical waveform generation, and physical sciences [43] [44].

MLLs have been the most popular frequency comb generation process in the literature since the 1990s, as mentioned in chapter 1. This approach, unfortunately, leads to limited frequency pitch tunability caused by stabilization constraints of the MLL cavity. Moreover, mode-pulling effects and chromatic dispersion in the cavity distort the frequency pitch uniformity of such combs. It turns out that for most applications, the frequency pitch tunability and uniformity are an asset. To overcome this, a cavity-free configuration driven from a low power continuous-wave (CW) pump has been proposed in the literature [45]. This approach enables a variation of the frequency pitch, only limited by the frequency range of a phase modulator. Other reported works with a similar electro-optic comb generation technique make use of multiple numbers of modulators and dispersion engineered highly-nonlinear fiber (HNLF) to produce wideband combs [46] [47]. Besides, no special emphasis has been given to reduce the linewidth of the seed laser.

In this chapter, we exhibit the operation of an OFC source with ultra-narrow and in-phase spectral lines in a cavity-free configuration. To ensure the generation of an OFC with narrow spectral lines, the first element of the optical processing chain is a single longitudinal mode Brillouin fiber laser that conveys low phase-noise to the OFC. Compression and mixing stages are cascaded to convert the Brillouin laser output into a full-fledged wideband OFC. The design of the source is also simplified with respect to previously reported ones as it makes use of off-the-shelf commercial HNLFs and a single phase modulator.

2.2 Brillouin Fiber Laser Synthesis

2.2.1 Experimental setup

Figure 2.1 presents a schematic of the BFL resonator, used to generate a single-mode Brillouin laser. The resonator is pumped with a primary source (PS) that consists of a CW external-cavity laser (ECL) followed by an EDFA with a noise figure of 4 dB. The ECL is an 8160B series Keysight tunable Laser with an optical signal to noise ratio (OSNR) of 60 dB, and a relative intensity noise of -145 dB/Hz up to 6 GHz. The PS generates Brillouin gain in a highly nonlinear fiber (HNLF-1) enclosed in a ring cavity. The linewidth narrowing effect of Brillouin scattering ensures that the linewidth of the BFL becomes significantly narrower than that of the pump laser [29]. An optical circulator with an insertion loss of 1 dB delivers the pump inside the resonant cavity. A counter-propagating Stokes wave circulates in the cavity when the pump power exceeds the Brillouin threshold of the HNLF1.

The 200 m long BFL cavity sustains a free-spectral range (FSR) of 1 MHz. With a Brillouin gain spectrum that has a 30 MHz full-width at half-maximum (FWHM), the BFL would be multimode unless additional filtering methods are implemented. The BFL single-mode operation is ensured from a series of two filtering mechanisms suppressing the many longitudinal modes of the compound ring cavity [48]. The filtering mechanism includes an in-fiber Fabry-Perot (FP) filter with 5 m long SMF-28 and a Sagnac loop interferometer with 4 m long unpumped Erbium-doped Fiber (EDF). The FSR in compound ring cavity depends on both the lengths of the primary and secondary cavity. The effective FSR of the compound cavity is given by,

$$FSR_{eff} = mFSR_L = pFSR_l \tag{2.2}$$

where, m and p are such integers which do not have a common factor, and FSR_L and FSR_l are the FSR of the main and FP cavity respectively. One way to attain a large effective FSR is to make the length of the FP cavity much shorter than the main cavity [49]. In that case, FSR_{eff} becomes approximately equal to FSR_l, which turns out to be 20 MHz in this experiment. Any $\mathrm{FSR_{eff}}$ from 0.5 to 1 time the Brillouin gain bandwidth ensures that only one longitudinal mode is excited within the Brillouin gain spectrum. Using a standard FP model, given in Appendix C, the resulting 3-dB linewidth, FSR, and suppression ratio of the compound cavity are found to be 4 MHz, 20 MHz, and 10 dB respectively from figure C1.

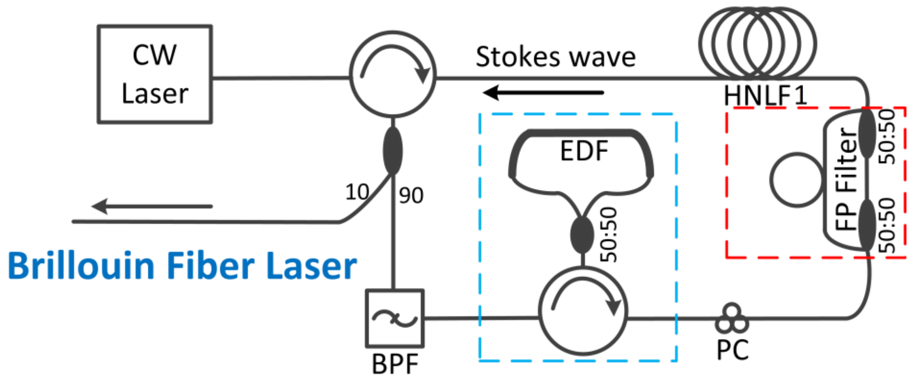

Figure 2.1. Schematic of the Brillouin fiber laser resonator having single longitudinal mode operation with a fiber Fabry-Perot filter and a Sagnac loop interferometer. BPF: Band-pass filter, EDF: Erbium-doped fiber, PC: Polarization controller.

The un-pumped EDF serves as an ultra-narrow filter. In the Sagnac loop, the standing wave generated in the EDF results into spatial hole burning and wavelength-selective saturable absorption [49] [50]. The central frequency of this filter automatically tracks the lasing wavelength ensuring stable single frequency operation [50]. To complete the BFL, an in-cavity band-pass filter with 200 GHz FWHM spectral width is used to suppress the out of band amplified spontaneous emission noise. A 10% coupler extracts a fraction of the Brillouin signal for the OFC section.

2.2.2 Result

An RF spectrum of the in-cavity signal is taken to observe longitudinal modes. For this purpose, the output of the 10% coupler is connected to a photodiode and an RF spectrum analyzer with a resolution bandwidth (RBW) of 1 kHz. Figure 2.2 shows RF spectra of the BFL with and without the use of the EDF and FP filters. The suppression of longitudinal modes using the FP filter and unpumped EDF is apparent in the figure. Longitudinal modes are attenuated by > 60 dB, which ensures single-mode operation for the resulting BFL.

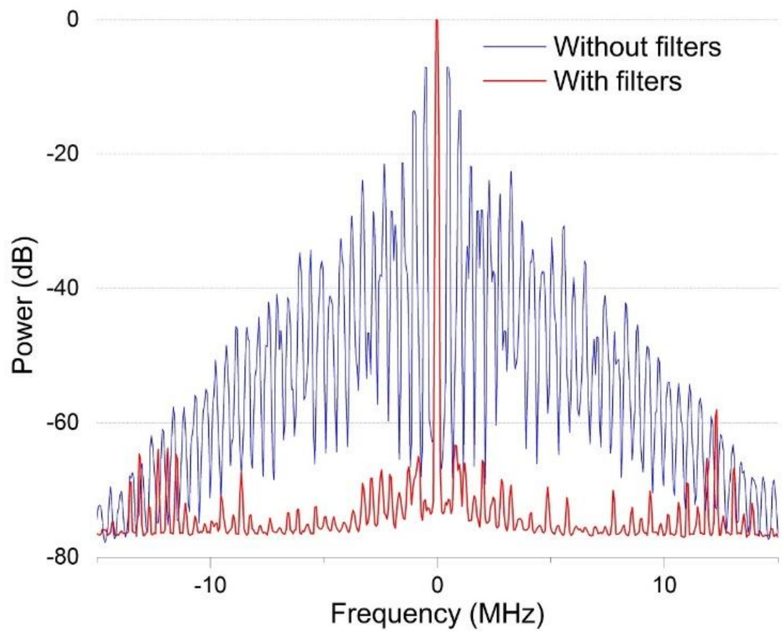

Figure 2.2. RF spectra are showing the suppression of longitudinal modes by the compound ring cavity inserted in the BFL.

The spectrum lineshape of the sources under test is measured using the self-heterodyne method, as shown in figure 2.3. For this purpose, the signal under test is split into two halves by a 3-dB coupler. One half is frequency-shifted by 200 MHz by an acousto-optic modulator, and the other half is de-correlated by propagation through 25 km long SMF-28 delay fiber. The signal under test and its frequency-shifted copy are then recombined with another 3-dB coupler to generate a beating spectrum at the photodetector. The spectrum of the photodetector current is probed with an electrical spectrum analyzer (ESA). Ideally, a length of hundreds of km of delay fiber is needed to resolve sub kHz linewidth. However, such a long fiber length imposes nonlinearity and frequency noise that prevents a stable beat signal.

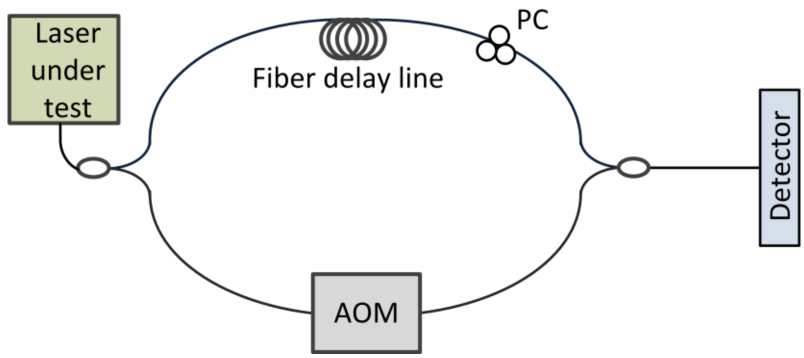

Figure 2.3. The methodology of the self-heterodyne technique for linewidth measurement. AOM: acousto-optic modulator, PC: polarization controller.

Fortunately, true FWHM value can still be extracted from the short-delayed self-heterodyne spectra in two ways. The first way is to fit the spectrum with a Lorentzian lineshape and infer the FWHM from its 20 dB linewidth [51]. Figure 2.4 shows the RF spectrum as measured for both the ECL and the BFL. The lineshape function of both signals is Lorentzian, and their bandwidth is measured at a -20-dB level for best precision. The 20 dB linewidth (FW20dB) of the laser spectrum leads to the FWHM linewidth from $FWHM = FW_{20dB} / 2\sqrt{99}$ [52]. The resulting FWHM linewidth of the ECL and BFL are 24 kHz and 1.5 kHz, respectively. The manufacturer provided value for the linewidth of the ECL is 10-100 kHz, which is confirmed in our measurement [53]. The linewidth of the BFL is narrower than the one of the ECL by a factor of 16, a significant reduction in terms of the spectral content of the noise. The BFL thus constitutes an interesting seed to use in a highly coherent optical frequency comb. The second way to extract FWHM linewidth is based on a short delayed self-heterodyne approach using the principle that the amplitude difference of the spectrum coherent envelope is related to the linewidth of the laser under test [54]. The linewidth is directly inferred from the power contrast in the first side-lobe of the envelope of the short delayed self-heterodyne spectrum. This approach also leads to an FWHM linewidth of 1.5 kHz, in agreement with the previous result obtained via self-heterodyne.

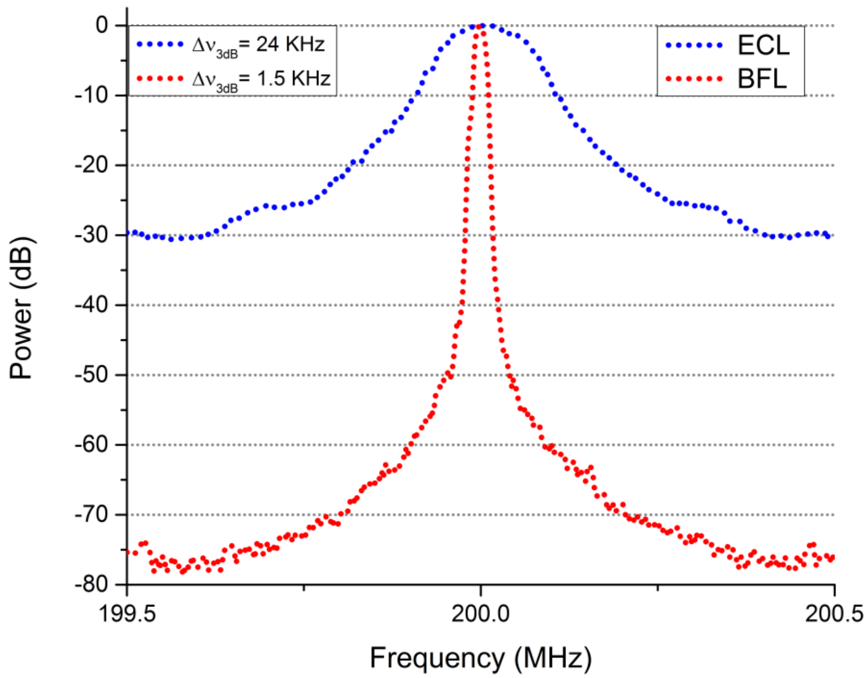

Figure 2.4. RF spectra of the PS and BFL signals from self-heterodyne.

Figure 2.5 shows the linewidth of the BFL as a function of output power. The BFL output power is varied by changing the input power of the PS. The BFL has a stable linewidth of 1.5 kHz independently of the output power, thus making a good candidate to generate a spectrally pure OFC. The laser linewidth is also stable the long term, as monitored by the evolution of the self-heterodyne beat signal over 48 hours. For calculating long term power stability of the Brillouin laser, the output power of the BFL was monitored for 48 hours. The variation of power level was minimal, only 1% of the nominal values.

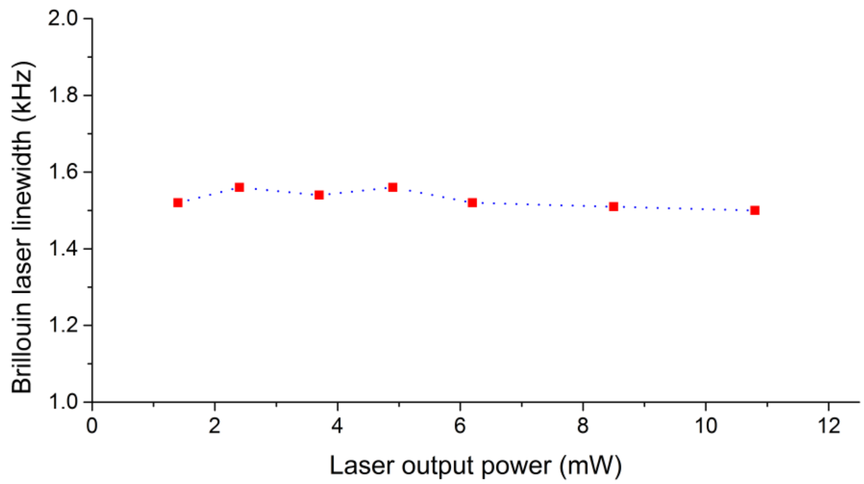

Figure 2.5. FWHM linewidth of the BFL as a function of output power.

2.3 Optical Frequency Comb

2.3.1 Experimental Setup

The single longitudinal mode BFL acts as a seed for the comb generation section, itself divided into two stages that are the pulse generation stage and the nonlinear mixing stage. Figure 2.6 shows the schematic of the experimental setup. In the pulse generation stage, the CW output from the BFL is positively chirped by a phase modulator with an 8 GHz electrical signal followed by propagation into a length of 10.4 km of SMF-28 fiber with anomalous dispersion at a rate of 18 ps/nm-km at a wavelength of 1550 nm. The optimum length of the SMF-28 is calculated from equation 1.8 and is a function of the modulation depth of the phase modulator and the frequency pitch. The dispersion of the fiber compensates the up-chirped portions of the CW signal and stretches the down-chirped portions of the CW signal. This results in a train of pulses at a repetition rate of 8 GHz and pulsewidth of 18 ps. The frequency pitch of 8 GHz, which is adjusted for the current setup, can be optimized for other values by changing the length of SMF-28 accordingly in the pulse generation stage.

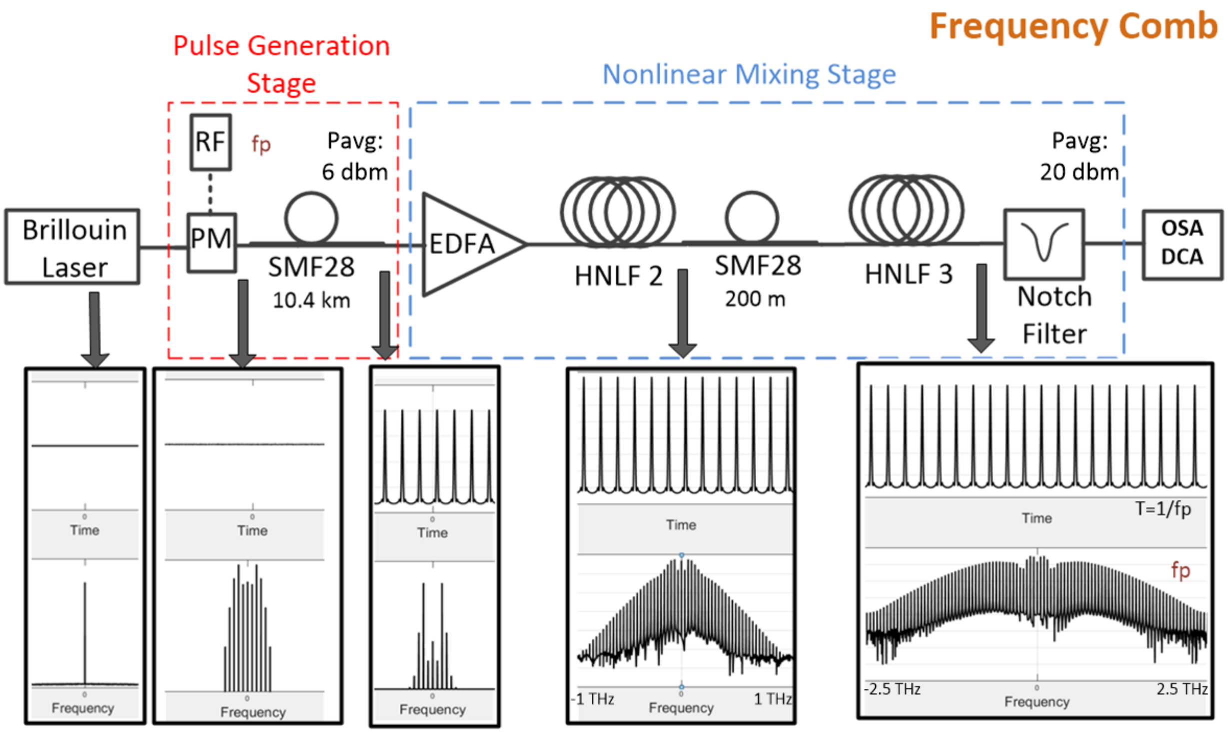

Figure 2.6. The process of generating an EO frequency comb from a CW Brillouin laser by dispersion compensation and nonlinear mixing. The simulated waveform and spectrum are for representation purpose only, and generated in *Matlab* using codes from the appendix B. PM: Phase modulator, RF: Radio frequency generator, EDFA: Erbium-doped fiber amplifier, OSA: Optical spectrum analyzer, DCA: Digital communication analyzer.

In the nonlinear mixing stage, pulses are amplified by an EDF to an average power of 500 mW and sent to HNLF 2 to trigger a narrowband OFC from FWM as described in section 1.3.2. This nonlinear process also chirps pulses via self-phase modulation with a maximum nonlinear phase shift of ~5 radians. The chirped pulses are recompressed by a second compression stage that includes a 200 m length of SMF-28 fiber. Finally, passing through HNLF 3 provides additional FWM and results in a wideband OFC made of narrow pulses in the time domain. Both HNLF 2 & 3 operate in normal dispersion to avoid modulation instability. Table 2.1 lists the parameters of all the HNLFs used in this experiment. The tunable notch filter, with 50 GHz FWHM, partially blocks the carrier at 1550 nm for temporal side-lobe suppression and spectral equalization [24]. The frequency pitch of the OFC is adjustable by changing the frequency of the electrical signal sent to the phase modulator. The temporal profile and the spectrum of the resulting

OFC are observed on a digital communication analyzer and an optical spectrum analyzer, respectively.

Fiber name	Length (m)	Dispersion (ps/nm/km)	Dispersion slope ($ps/nm^2/km$)	Nonlinear parameter (1/W-km)
HNLF1	200	-0.04	0.02	10.5
HNLF2	1007	-0.04	0.02	10.5
HNLF3	1007	-0.69	0.0074	12.5

Table 2.1. *Specifications of the highly nonlinear fibers used in the setup. The attenuation coefficient is 1 dB/km in all cases.*

2.3.2 Results

Figure 2.7 shows the optical spectrum and temporal profile at the output of the OFC. The optical spectrum is measured with an RBW of 0.80 pm. The OFC has a frequency pitch of 8 GHz and spans over a 15-dB bandwidth of 32 nm, resulting in (32*125/8) ~ 500 spectral lines. The optical signal to noise ratio is ~28 dB in the central region and drops to ~23 dB near the comb edges, as shown in the insets. In the time domain, a train of pulses with an FWHM duration of 8 ps is generated. For an average EDFA output power of 1 W, the carrier wavelength provides the maximum power of - 0.50 dBm whereas the short wavelength edge of the comb provides the smallest power with – 15.50 dBm. By cascading more compression and nonlinear mixing stages, one could further expand the wavelength span of the OFC [21]. The experimental results shown in figure 2.7 are in general agreement with the simulation, shown in the figure B1 in Appendix B. In the simulation, an ideal CW laser source and optical amplifier were assumed, which may explain the differences between both sets of results.

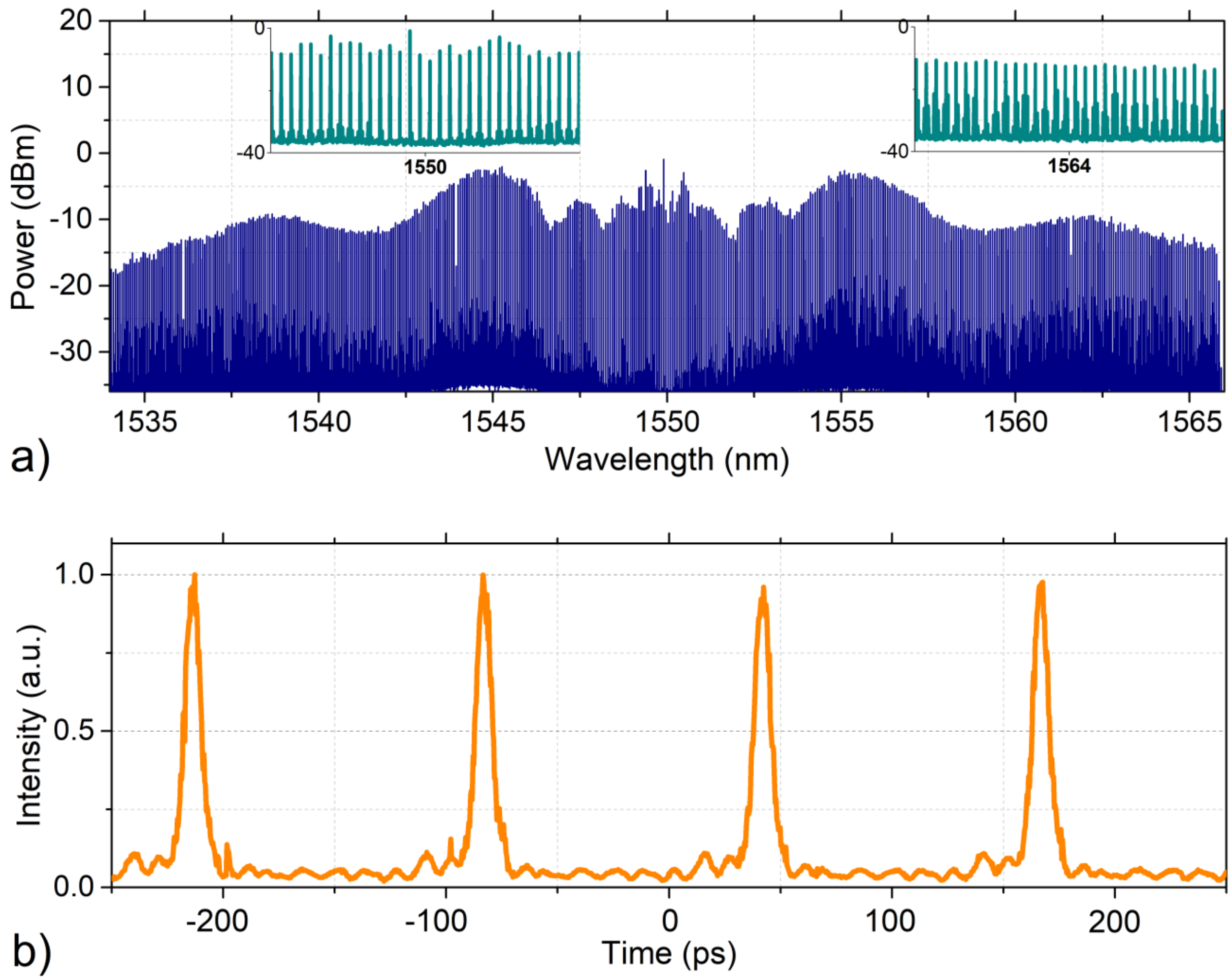

Figure 2.7. a) The spectrum of the frequency comb recorded in a high-resolution OSA. The insets show the zoomed-in 2-nm wide spectra at the center (1550 nm) and edge (1564 nm) b) Time domain trace of the frequency comb recorded in a DCA.

Now the question is whether the narrow linewidth of a BFL can be duplicated to every spectral line of the OFC, even at those with a large frequency offset with respect to the carrier frequency. To answer this question, the linewidth of the RF signal generator is measured directly from an ESA, resulting in an FWHM linewidth of $FWHM_{RF}$ = 5 Hz. Although this linewidth is negligible with respect to 1.5 kHz, the linewidth of an optoelectronic comb scales linearly with comb order contributed by the phase noise of the RF signal [55]. That is, the resulting linewidth of a spectral line of order n is expected to reach n × $FWHM_{RF}$. As a result, the outermost comb of order 250 increases the linewidth by 1.25 kHz, leading to a total linewidth of 2.75 kHz. Despite an increase of the linewidth at high comb order, the resulting linewidths remain advantageously narrower than commercial ECL linewidths of 10-100 kHz [56]. Furthermore, if the pump laser of the BFL has a sub-kHz linewidth, the resulting Brillouin laser will reduce that linewidth even further because of the linewidth narrowing effect.

The linewidth of the OFC is first measured by self-heterodyne. A tunable notch filter isolates groups of six spectral lines and self-heterodyne is performed on this signal. For six arbitrary spectral lines of the comb taken anywhere in the 8 nm emission spectrum around the carrier wavelength of 1550 nm, the linewidth measurement consistently leads to 1.5±0.1 kHz. The linewidth measurement approach using subsets of spectral lines has been simulated and confirms that the linewidth is invariant of the number of spectral lines used for the measurement, due to their phase matching and proximity to the carrier frequency. Figure 2.8 shows the typical linewidth of the OFC at ~1550 nm. This experimental measurement shows that low phase noise and mutual coherence are preserved among the individual frequency lines near the carrier frequency [22]. Ref [22] showed the preservation of 5 KHz pump linewidth in the resulting EO combs, where the current work showed the preservation of 1.5 KHz pump linewidth in the comb generation process. Since the phase noise of EO comb lines increases linearly with their order, the linewidth of the comb lines at the edge of the bandwidth shall broaden more than those at the center. Fabry-Perot filtering or injection locking is necessary to preserve strict coherence of the comb lines near the comb edge for more demanding applications [57].

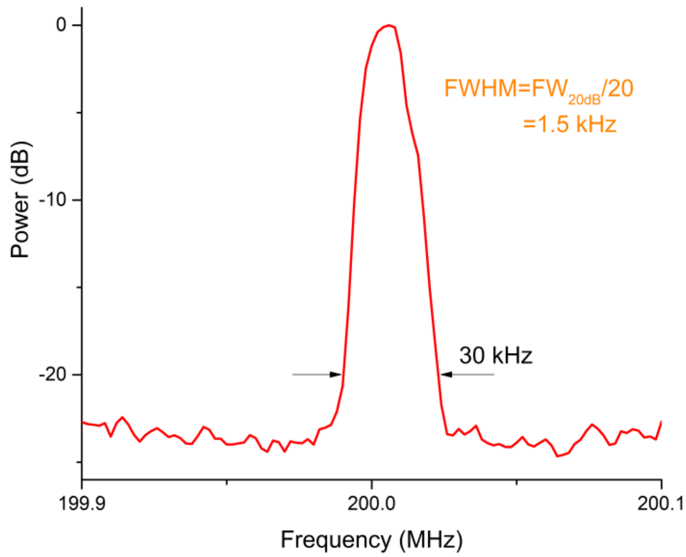

Figure 2.8. FWHM lineshape of the OFC within the 8 nm emission spectrum centered at 1550 nm. Taken with an ESA with RBW=300 Hz.

2.4 Summary

In summary, we have demonstrated the operation of a wideband optical frequency comb with low phase noise by utilizing the linewidth-narrowing effect of Brillouin scattering. This chapter describes the process of creating a low-noise fiber laser from stimulated Brillouin scattering, followed by the synthesis of a wideband frequency comb from this fiber laser source. The comb has 500 ultra-narrow spectral lines with FWHM of 1.5-2.75 kHz, covering a spectral span of 32 nm. The system includes a narrow-linewidth optical signal seeded from a Brillouin laser, and the comb is generated in a cavity-free configuration using the parametric gain of nonlinear fibers [58]. With appropriate dispersion engineering of the HNLFs, the span of an OFC as the one presented can be broadened beyond hundreds of nm [23]. The frequency tuning range is only limited by the operating range of the phase modulator, which is 2-12.5 GHz in our case. However, generation of wideband comb with smaller frequency pitch is difficult because pulses have a relatively broader pulse width after the compression stage, which results in smaller spectral bandwidth. To generate a smaller frequency pitch OFC with a wider bandwidth, pulse picking, or spectral Talbot effect may be used on a comb with repetition rate. OFCs, with such low phase noise, have potential applications in coherent optical communication, precision dual-comb spectroscopy, and high-quality microwave signal synthesis. In the current work, the phase noise performance is characterized by the linewidth measurement with the self-heterodyne method only. This method only provides information about the Lorentzian lineshape of the phase. Therefore, single sideband power spectral density measurement would be more appropriate for a complete and more accurate phase noise characterization since the self-heterodyne technique cannot measure the relative intensity noise and long term stability of a laser.

Chapter III.

Distance Measurement by Frequency Comb

[2]In this chapter, we present a precision distance meter that operates from sweeping the repetition rate of an EO frequency comb. The dynamic range and scan rate of such comb make it possible to measure absolute distances up to hundreds of meters with an accuracy of ±5 μm and acquisition time of 30 ms. The proposed technique requires no fiber stabilization system, making the device simple and cost-effective.

3.1 Introduction

From self-driving cars to space missions, from semiconductor chip production to micro electro-mechanical system production, the need for a simple, precise and fast device to measure arbitrary distances is paramount. The realm of distance measurement is wide and application-specific [59]. For LIDAR technology of self-driving cars, one might not be interested in sub-mm scale precision while nm precision is standard for semiconductor chip manufacturers. Therefore, many techniques for distance measurement have been proposed in the literature. Of these techniques, several are

[2] The content of this chapter has been submitted to publication in **M. Imrul Kayes** and Martin Rochette, "Precise distance measurement by a single electro-optic frequency comb," Photonics Technology Letters, vol. 31, no. 10, pp. 775-778 (2019).

based on the use of optical frequency combs [60]. These include time-of-flight distance measurements [61], pulse cross-correlation method [62], multi-wavelength interferometry [63] [64], and multi-heterodyne interferometry [65]. In multi-heterodyne interferometry, a frequency comb pair with offset repetition rate is used to demodulate the carrier phase information and measure a distance. However, this method implicitly requires phase matching between the two comb sources. Phase locking electronics is a solution to this requirement at the cost of making the system complex, expensive, and sensitive, preventing a widespread use in engineering applications. Dual electro-optic combs have been used to circumvent the phase matching requirements. The resulting interferogram still needs to be averaged over a long time to obtain a distance measurement accuracy at the µm range [66].

The OSCAT technique, described in section 1.5, may be used to simplify the interferometer design and overcome the need for phase-matching [33]. OSCAT has been used for applications including spectroscopy [67], vibrometry [68], imaging [69] and ranging [34]. This interferometric method operates from repetition rate modulation of a frequency comb. Pulses from a frequency comb are divided and recombined after passing through an interferometer that is imbalanced from two arms of unequal lengths. A change in repetition rate propagates through the shorter arm first, leading to two pulse trains with an offset repetition frequency momentarily present at the output of the interferometer. Therefore, the optical path delay between two pulses is scanned by periodically sweeping the repetition rate of the frequency comb. This results in a cross-correlational interferogram due to the sliding walk-off between the pulse pair. The peak position of the interferogram, produced by constructive interference between the pulse pair, is a function of length mismatch of the interferometer. Therefore, extracting the repetition rate at the peak of the interferogram provides a precise measurement of distance.

So far, researchers have only used mode-locked lasers (MLL) as a frequency comb source for OSCAT based distance meters. MLLs, unfortunately, limit the effectiveness and commercialization of this method. It is because they have a limited sweeping range for repetition rate, requiring the use of a long delay fiber for desired high-resolution and accuracy [35] [70]. Moreover, OSCAT systems are complex since the long interferometer arm needs active stabilization because a drift in fiber length directly impacts the measurement results [70]. This defeats the main purpose to originally switch from dual-comb systems, that is, to avoid electronic stabilization requirement. Moreover, OSCAT based methods require a preliminary rough measurement of the interferogram length-mismatch before enabling high-resolution distance measurement. These drawbacks severely limit the widespread use of MLL-OSCAT technology for distance measurement.

A great quality of EO combs is the flexibility of the repetition rate, which can be swept over a broad range compared to MLL [67]. This advantage allows OSCAT based meters to use a short delay fiber to achieve high-resolution measurement, without active length stabilization. In this chapter, we use EO combs to provide absolute distance measurements with an accuracy of ±5 μm over a range of 200 m and a measurement time of 30 ms. The proposed method does not need prior knowledge of initial length mismatch of the interferometer, another significant improvement over previous OSCAT based methods. This simple, robust, and field-deployable distance meter is a good alternative for applications with absolute accuracy in μm range.

3.2 Theory

An optical frequency comb with a repetition rate that is swept periodically leads to a temporal interferogram, after passing through an imbalanced interferometer [33]. This occurs from the recombination of two sets of delayed pulses with momentary distinct repetition rates. The center-burst of the interferogram includes a local peak corresponding to a specific instance of repetition frequency when the two pulse trains interfere constructively. Indeed, this position of the peak depends on the length of the delay fiber of the interferometer. For the peak to occur at a repetition frequency f_{rep}, the absolute length mismatch (L) between two arms is given by,

$$L = m.c_0/f_{rep}.n_g \tag{3.1}$$

where c_0 is the speed of light in free-space, n_g is the group index and

$$m = round\left(\Delta D/\lambda_{pp}\right) \tag{3.2}$$

is the number of pulses contained in the length of the delay. Here ΔD is the optical path difference between the two interferometer arms and λ_{pp} is the physical distance between two adjacent pulses in free-space. Therefore, a target mirror placed within the path of the delayed arm gets its position precisely measured from equation (3.1). The maximum path difference (MPD) between the pulse pair is given by [33],

$$MPD = \left|m.\Delta f/f_{rep}^2\right| \tag{3.3}$$

where Δf is the scan range of sweeping repetition frequency. To realize arbitrary distance measurement, the sweep range of the repetition frequency should be such as to cover the entire distance between two adjacent pulses. The condition is expressed by,

$$m.\Delta f > f_{rep} \tag{3.4}$$

Equation (3.4) serves to demonstrate the advantage of EO combs over MLL for distance measurement. The dynamic range of frequency sweeping (Δf) for an MLL is generally limited, for example, 2.1 kHz in ref [70] and 3.5 kHz in ref [35]. On the other hand, the effective sweep range of an MLL laser for OSCAT experiment may be increased using, e.g., a km long delay fiber as it multiplies the effect of frequency sweeping ($m.\Delta f$) [34]. However, the resulting interferogram requires stabilization of such long delay fiber for a reliable measurement. In contrast, the dynamic range of EO combs is high (10-100 MHz), enabling to scan the full range of delays with a short delay fiber without active fiber stabilization scheme.

EO combs also simplify this calculation of the number of pulses in the delay (*m*) which needs to be determined first to calculate *L* from equation (3.1). According to equation (3.2), the optical path difference ΔD between two arms of the interferometer should be measured first to determine m. This means that for each distance measurement, two separate measurement mechanisms are needed - a macro-measurement system that measures ΔD with low resolution and a micro-measurement system that uses *ΔD* to calculate *L* with high-resolution. This approach is certainly redundant since the same distance is measured twice to calculate the final value. Fortunately, EO combs successfully determine *L* in a single step because the periodicity of the resulting interferogram is related to m. If the sweep range of repetition rate is broad enough to generate two interferogram peaks at frequencies f_{rep1} and f_{rep2}, the path delay (*MPD*) between the two peaks is given by the inverse of the repetition rate. Then, according to equation (3.3),

$$1/f_{rep1} = \left|m.(f_{rep2} - f_{rep1})/f_{rep1}^2\right|$$
$$m = round\left|\frac{f_{rep1}}{f_{rep2}-f_{rep1}}\right| \qquad (3.5)$$

Therefore, no separate measurement of *m* is necessary for high-resolution distance measurement. Simply ensuring a broad sweep range is enough to calculate both *m* and *L* in a single step.

3.3 Experiment

Figure 3.1 shows the experimental setup for precision distance measurement. An electro-optic frequency comb [71] emits a train of optical pulses at a wavelength of 1550 nm. Pulses have a duration of 12 ps and a repetition rate of 10 GHz, as set by a radio frequency clock generator [63]. The pulse train is filtered by an anti-aliasing filter and then sent to an unbalanced Mach-Zehnder interferometer. The interferometer is made of two 3-dB couplers, a long arm, and a short arm. The long arm includes an 11.20 m delay fiber followed by a target mirror connected with a circulator. The target mirror is part of a motorized delay module that can precisely adjust the distance of the mirror. Signals in the long arm travel to the delay module and get reflected by the mirror. The reflected signal is recombined with the signal from the short arm with a 3-dB coupler. Both signals are sent to a photodiode from which an electrical signal is recorded with a real-time oscilloscope. The repetition rate of the frequency comb is swept in an analog fashion from the RF clock signal, leading to a periodic cross-correlational interferogram at the output port of the interferometer. The center-burst or peak of the interferogram correlates with the length mismatch of the interferometric arms. Therefore, if the mirror position changes, so does the peak position of the interferogram, leading to a new peak repetition rate.

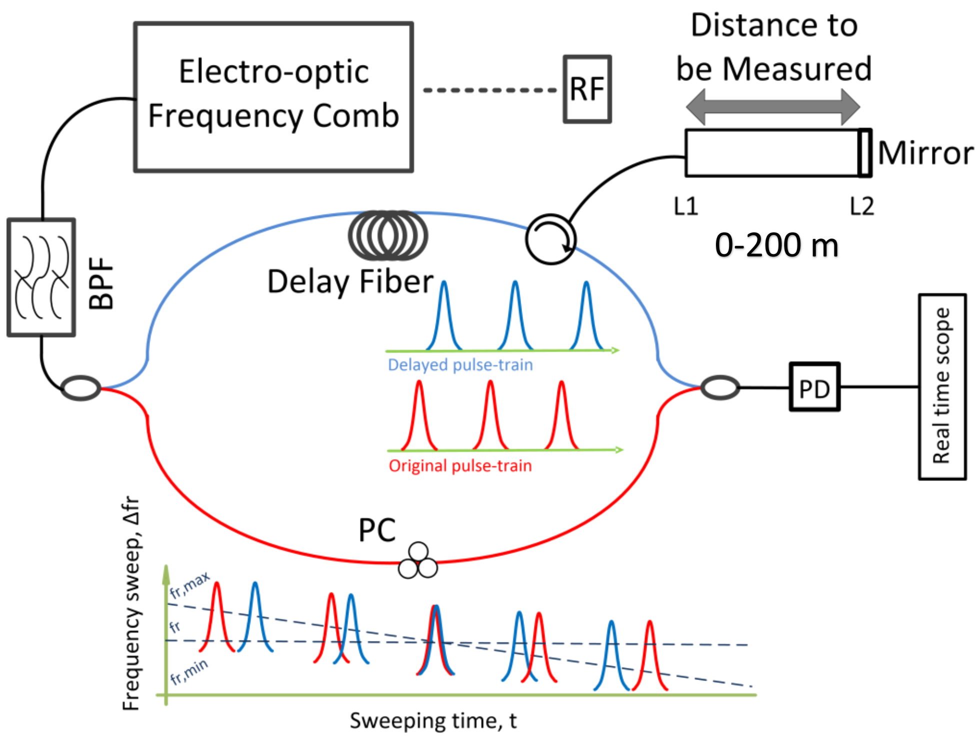

Figure 3.1. Block diagram of the experimental set up for absolute distance meter. RF: Radio frequency clock generator, PD: Photodetector, BPF: Band-pass filter.

3.4 Results

3.4.1 Distance Measurement

As a proof of concept, the target mirror is placed at a reference position L1 (see Fig. 1). To perform a high-resolution distance measurement, the frequency of the sinusoidal RF signal is swept periodically from 9.995 GHz to 10.25 GHz with a sweep time of 30 ms. The sweep time is limited by the maximum analog scan speed of the RF clock generator. As a result, two interferogram peaks are recorded in every 30 ms in the oscilloscope after each complete sweep. A trigger signal is also retrieved from the RF clock as a means to synchronize the interferogram acquisition. Several interferograms may be averaged to enhance the signal to noise ratio. Recorded interferograms are post-processed with *Matlab* to precisely determine the positions of both peaks. For this purpose, every interferogram frame is Hilbert transformed to retrieve the center of the envelope and determine its peaks. The repetition frequency at peak position is determined by interpolation within the known sweep range of frequencies. By retrieving the values of both peak positions, the relative distance for mirror position L is calculated from equation (3.5) and (3.1). For example, if the mirror is placed at the initial reference position *L1*, the values of f_{rep1} and f_{rep2} are ~10.0021543 GHz and ~10.018964643 GHz, respectively, which leads to m=595. From equation (3.1), the relative mirror distance is L=12.15 m, which accurately accounts for the 11.2 m delay line and the additional optical path of 0.95 m before the delay module. The relative mirror distance equals to the length mismatch of the interferometer.

Figure 3.2a shows the interferogram recorded at reference position *L1*. Figure 3.2(b-c) show interferograms recorded with the mirror displaced by 6 m and 12 m respectively from the reference. The displacement is performed by inserting additional optical patch-cords after the delay fiber. From equation (3.1), it is evident that length mismatch and repetition rate have an inverse relationship. Therefore, the peak of the interferogram shifts to lower frequencies whenever the optical delay is increased.

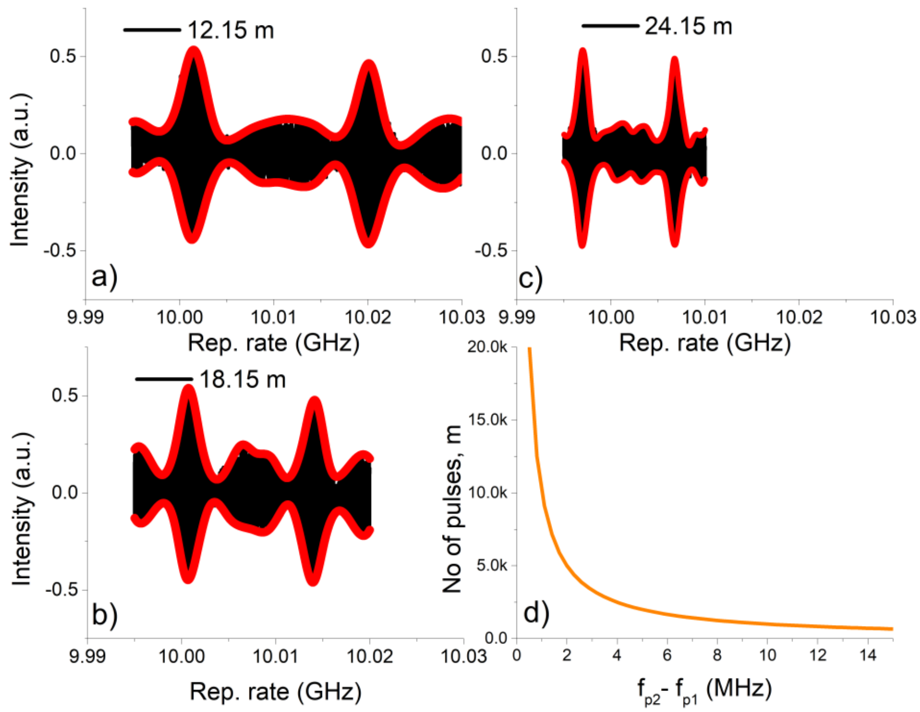

Figure 3.2. a-c) Interferogram acquired when the absolute mirror displacement is 12.15 m, 18.15 m, and 24.15 m respectively. d) Relationship between pulse number and peak repetition rate difference according to equation (3.5).

It is also apparent that the increase of the length mismatch decreases the period of successive interferogram and the peaks of the interferogram are obtained with a smaller range of frequency sweep. This is demonstrated in figure 3.2(d), showing the inverse relationship between the peak separation and pulse number, m.

The accuracy of the proposed distance measurement method is verified by mounting the target mirror on a motorized delay module (MDM). The MDM can change the mirror position over a maximum range of 120 mm with an accuracy of ±3 μm. Therefore, it can be used to increase the length of the delayed arm by a known and precise distance set by the user. For the purpose of accuracy measurement, the displacement of the target mirror is increased by the MDM in a step size of 0.6 mm with respect to reference position L1. For each increment, the corresponding increase in distance is measured from equation (3.1). These distance points are compared to their original values to check the accuracy of the proposed method.

Figure 3.3 shows the differences between the measured values and the reference values of mirror displacement. There are some variations in the measured value from the ideal zero position. The range of variation is ±5 µm with a relative precision of 0.2 µm, which sets the accuracy of the proposed distance measurement method. The relative precision is calculated by averaging the measured distance values 10 times at each position of the mirror. Similar results are obtained with a different starting position of the mirror. Here it should be mentioned that, since the delay module is accurate only up to 3 µm, the accuracy of the proposed method has the potential to reach even lower values with the use of an MDM providing better measurement accuracy.

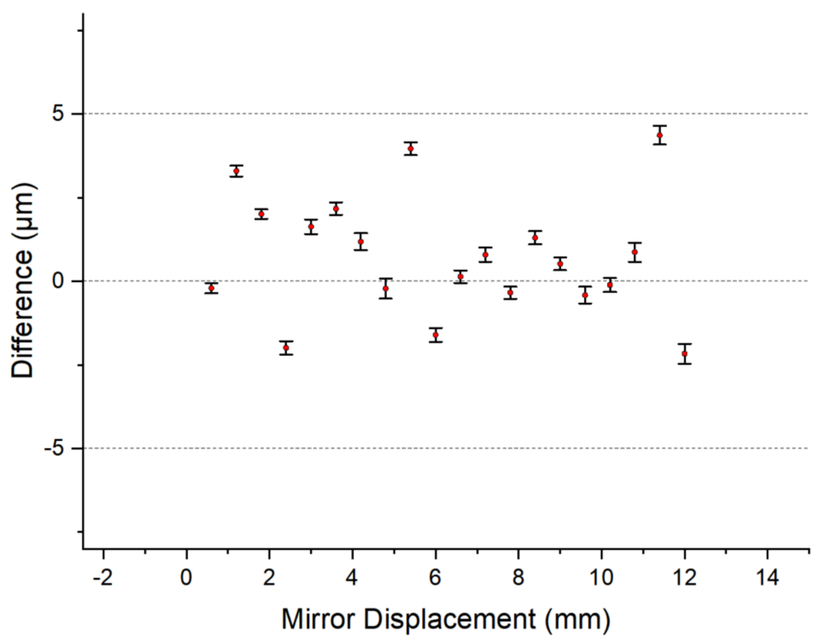

Figure 3.3. Comparison between the distance values measured using the proposed method and reference measurement. Values are in agreement within ±5 µm with the error bars showing a relative precision of 0.2 µm.

Several factors limit the accuracy of the proposed distance measurement method. The most dominant contribution comes from the uncertainty of repetition frequency. There are several sources such as accuracy of the RF signal frequency, precision of the oscilloscope time-base, carrier envelop offset frequency of the EO comb and accuracy of Hilbert transformation algorithm may affect the accurate determination of the repetition rate. The time-base accuracy of the oscilloscope (RIGOL MSO1000Z) is ±25 ppm. After each sweep, the number of samples per interferogram frame is 300K. Therefore, the contribution of frequency uncertainty from oscilloscope is calculated to be 750 Hz. The frequency uncertainty of the RF signal generator (Anritsu MG3690C) is dependent on aging, calibration, temperature variation, etc. For an aging rate of 0.1 ppm/year, the frequency uncertainty of a 10 GHz signal two years after calibration is 2 kHz. The carrier-envelop offset causes a positional uncertainty of the interferogram peak location equal to the quarter of the carrier wavelength [72]. This contributes to the repetition frequency uncertainty of 387 Hz. Therefore, without considering the accuracy of Hilbert transformation, the combined frequency uncertainty (*df*) equals 3.14 kHz. The positional uncertainty due to repetition rate uncertainty is calculated by differentiating equation (3.1) which is given by,

$$dL = \pm\left(m.\frac{c_0 df}{f_p{}^2.n_g}\right) \tag{3.6}$$

According to equation (3.6), the positional uncertainty (dL) is calculated to be ±3.7 µm, which is very close to the measured accuracy value of ±5 µm. The inaccuracy of the Hilbert transformation algorithm, the variation of environmental condition, dispersion, and refractive index uncertainty of the delay fiber may also reduce the accuracy of the measurement. According to equation (3.6), measurement error dL also depends on the measurement range, having a linear relationship with the absolute target distance [72].

The maximum measurable distance is determined by our ability to extract repetition rate values at the peaks of the interferograms. Therefore, the dynamic range of measurement is a function of the bandwidth of the oscilloscope (500 MSa/s) used in this experiment. As the target mirror displacement is increased, the two peaks move towards each other. At distances beyond 250 m, both peaks start to overlap, making the measurement of m uncertain according to equation (3.5). Finally, the bandwidth of the EO comb (BW_{10dB}=10 nm) also influences the dynamic range since the fringe of each interferogram is related to the width of the comb pulses. So, with an oscilloscope having infinite bandwidth, the dynamic range of the proposed method will be limited by the pulse width of the frequency comb signal.

3.4.2 Motion tracking

One major advantage of the proposed method is its rapid measurement capability. Since the interferograms are refreshed every 30 ms, this method would be able to track a moving object or a vibration [68]. With the help of the MDM, it is possible to make the target mirror move back and forth at different velocities. This is done by applying a sinusoidal voltage to the MDM, which proportionally changes the mirror position periodically. Several interferograms at different points of time need to be recorded to track this movement. For this purpose, 15 subsequent interferograms are captured over a 1 s period. Since the mirror is continuously moving, the absolute distance of the mirror is changed at each instance that gets recorded by the interferograms. By determining the repetition rate at each of the interferogram peaks, as previously described, it is possible to make a displacement-time plot for each speed setting. Figure 3.4 shows such graphs for 3 different velocities which are related to each other by a multiple of 2. The points for a specific velocity fits well with a sinusoidal curve, showing an accurate tracking of the motion. The slope of each curve at the linear section gives the speed of the motion that matches on point with the speed setting from the MDM.

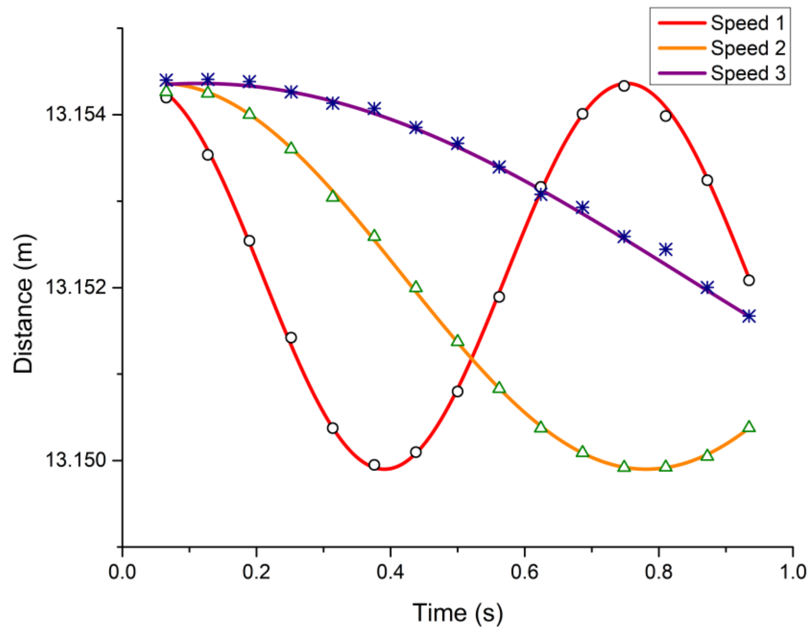

Figure 3.4. Motion tracking for three different speed settings of the motorized delay module. Since the mirror is moving continuously between two positions, the subsequent interferograms are shifted too, resulting in a sinusoidal track of the movement.

3.5 Summary

In conclusion, we have experimentally demonstrated a new method for absolute distance measurement with µm precision and arbitrary distances. Only a single EO comb is needed to produce a cross-correlational interferogram to sample a distance accurately. Any unknown distances up to 200 m can be measured by determining the instantaneous repetition frequency at the peak of the interferogram. Compared to MLL based OSCAT methods, this system is robust, simple, and inexpensive, and require no fiber stabilization scheme. Ref [72] reported an accuracy of ±3 µm over 80 m with an acquisition time of 1s per interferogram. Ref [73] reported an accuracy of ±3 µm over 75 m range with a measurement time of 1.5 s using a length stabilized delay fiber. Ref [35] has an accuracy of ±10 µm over 47 m range with an active length stabilized interferometer. All the above methods are powered by MLLs, requiring another range meter to determine *m* to calculate the high precision target distance, as explained in section 3.2. Ref [66] proposed a dual electro-optic comb based distance meter showcasing ±20 µm accuracy with 10 s of measurement time. On the other hand, the accuracy of the proposed method is experimentally determined to be ±5 μm, very close to the 3 μm accuracy of the motorized delay line. The acquisition time per interferogram frame is only 30 ms, making this measurement method faster than any other reported works based on OSCAT and dual-comb based distance measurement methods [65].

Chapter IV.

Single Frequency Comb Spectroscopy

[3]In this chapter, we demonstrate the operation of a novel Fourier transform spectrometer that operates from sweeping the pulse repetition frequency of an electro-optic frequency comb. Incorporating a length imbalanced interferometer, this single comb system is analogous to a conventional dual comb system, but with a greatly simplified design. The functionality of the spectrometer is demonstrated via the high-resolution spectrum measurement of an $H^{13}C^{14}N$ reference gas cell.

4.1 Introduction

For broadband molecular spectroscopy, the hundreds to thousands of sharp spectral lines make the OFC a suitable tool for spectrum sensing with high-resolution and high sensitivity [74]. However, to detail individual spectral lines, an optical spectrum analyzer with a resolution as high as the spectral lines under investigation must be used, which is typically expensive, if available. In the

[3] The content of this chapter has been subjected to publication in **M. Imrul Kayes** and Martin Rochette, "Fourier Transform Spectroscopy by Repetition Rate Sweeping of a Single Electro-Optic Frequency Comb," Optics Letters 43(5), 967-970 (2018).

case of traditional Fourier transform (FT) spectrometers, described in section 1.6, frequency combs can replace polychromatic light sources to offer an improved signal to noise ratio. However, comb sources do not overcome the two disadvantages of FT spectroscopy that are, an acquisition time that is limited by the scan velocity of a mechanical scan mirror, and an output resolution that is limited by the maximum path difference between two interferometric arms.

In response to this, dual-comb spectroscopy overcomes these limitations by employing two combs of slightly different repetition rates, which produces a cross-correlational interferogram at the sample, as shown in figure 4.1 [75]. Theory of the dual-comb spectrometry is out of scope for this chapter and described in detail in chapter 5. Dual-comb spectroscopy has ultrafast acquisition time, no mechanical moving part, and a resolution determined by the repetition frequency of the comb. However, the strict phase-matching requirements between both combs make this system complex, bulky, and not suitable for field use.

Electro-optic (EO) comb-based dual comb systems have greatly improved in the last few years [76] [77] [26]. Indeed, dual EO combs are seeded from one CW laser. This brings the main benefit of EO combs, that is, EO combs do not require phase matching in contrast to mode-locked based systems. However, for the optical bandwidth of EO combs to cover hundreds of nm, multiple sections of pulse compression, amplification, and nonlinear mixing are required, often via adding km-long optical fibers. Maintaining the coherence of two EO combs over such a long length of fiber is a challenging task, degrading the performance of dual-comb EO systems.

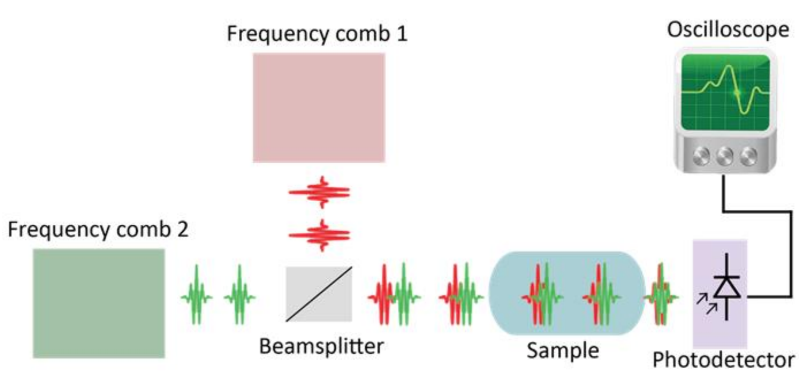

Figure 4.1. Schematic showing the principle of dual-comb spectroscopy.

Single comb spectroscopy with a sweeping repetition frequency is a simple and efficient alternative to the ones presented above [36]. It uses a length imbalanced interferometer to create two pulse trains of different instantaneous frequencies, a technique similar to OSCAT, described in section 1.5. Optical path delays between two overlapping pulse pair are scanned by changing the repetition frequency (f_{rep}) of the comb. Since one arm of the interferometer is shorter than the other, a change of the repetition frequency impacts the output of the shorter arm at first and momentarily, two pulse trains with a different repetition frequency are generated. The system becomes analogous to a dual comb system when the repetition frequency is varied continuously. This method was originally intended for mode-locked laser (MLL) based OFC where f_{rep} sweeping is achieved through varying the laser cavity length with a piezoelectric actuator [78]. However, the dynamic range of such f_{rep} sweeping is limited due to stabilization constraints of the MLL cavity. As a result, one needs a long (>200 m) delay line to achieve sufficient spectral resolution for spectroscopy. A long delay line is sensitive to ambient temperature variation and causes interferometric timing and phase fluctuation of the comb signal [36][58]. Two narrow bandpass filters must be used to track the timing and phase variation to compensate for the impairments of the delay line. By extracting the phases of the filtered signal, the phase and timing grids of the interferogram are corrected [79].

In contrast, single EO comb-based OSCAT systems are capable of high-resolution spectroscopy without the need for a long delay fiber. Also, in terms of Signal to noise ratio (SNR), single comb systems perform better than dual comb systems. For dual-comb spectroscopy, each interferogram must cover the complete optical path length difference set by the difference in repetition rate. For single comb spectroscopy, cyclic variation in repetition frequency means that a small and selectable pulse detuning range can be covered, and this translates into an improved SNR since all pulses are probing a specific spectral range of interest [79]. It is only in terms of acquisition speed that dual comb systems outperform single comb based systems, since the acquisition speed of a dual comb system is limited by the bandwidth of its detector (~ms) whereas the acquisition speed in a single comb system is limited by the tuning speed of its microwave source (~s).

In this chapter, we demonstrate the operation of a single EO comb based spectrometer (SCS) for the first time, to the best of our knowledge. The SCS overcomes the limitations of mode-locked laser based systems, bypassing the phase correction requirement by offering a greater dynamic range of repetition frequency sweeping. Greater dynamic range mitigates the delay length requirement for maximum resolution and minimizes the interferometric phase fluctuation. Moreover, this approach offers long term stability since there is no cavity involved in EO comb generation process [58].

4.2 Theory of Single-comb Spectroscopy

An OSCAT system mimics a dual comb system by using a periodic variation of the pulse repetition rate transmitted through an imbalanced interferometer. Due to the presence of a delay in one of the arms of the interferometer, a variation of the pulse repetition rate is transmitted through the short arm first, then through the long arm in second, with a delay that corresponds to the difference in arm’s lengths. Two pulse trains with different repetition rates thus reach the output of the interferometer and superimpose for a brief period of time. The OSCAT system gets completed with a smooth and cyclic variation of the comb repetition rate, resulting into a variation of the relative delay in between pulses coming from each interferometer’s arm, and thus forming an interferogram at detection as shown in figure 4.2.

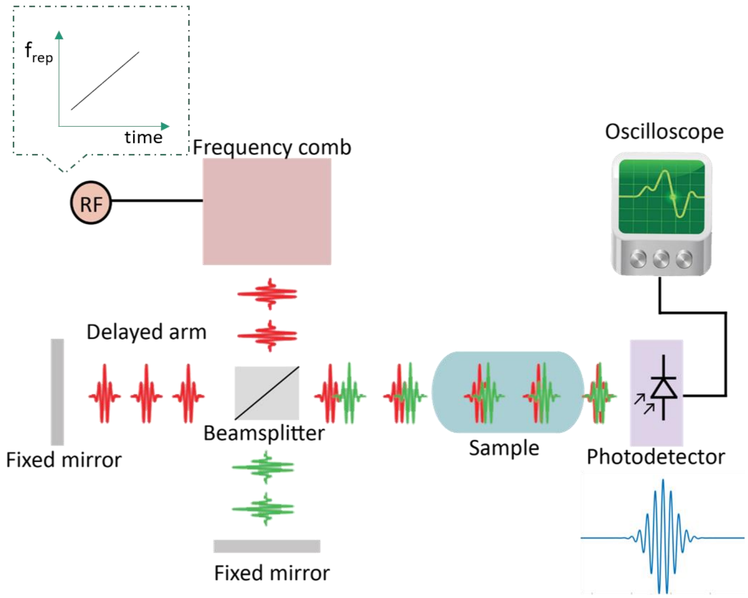

Figure 4.2. Schematic showing the principle of an OSCAT based spectroscopy.

Next, let us derive the relative time delay between a pulse pair for each incremental change in comb repetition frequency [36]. If L is the length mismatch between two arms, then the number of pulses stored in the delay fiber is given by, $N = L.f_r.n/c$, where c is the speed of light in vacuum and n is the group refractive index of the fiber. The repetition frequency at the peak position of the interferogram determines f_r. The time delay that separates a pulse and its delayed version after passing through the interferometer (pulse pair) is,

$$\tau = L.\frac{n}{c} = \frac{N}{f_r} \tag{4.1}$$

Thus, for each incremental change δf_r of repetition frequency, the resulting increment in time delay of the pulse pair is,

$$\delta\tau = -N.\frac{\delta f_r}{{f_r}^2} \tag{4.2}$$

The maximum optical path delay of the pulse pair after a full f_r scan is given by,

$$MPD = \delta\tau . n_{step} = -N . \delta f_r . \frac{n_{step}}{{f_r}^2} \tag{4.3}$$

where n_{step} is the number of frequency scan step. The spectral resolution (R) is given by,

$$\mathrm{R} = \max\,(f_r, MPD^{-1}) \tag{4.4}$$

which is determined by the inverse of MPD if not limited by repetition rate [79]. Thus, it is apparent that increasing the product $N . \delta f_r . nstep$ maximizes spectral resolution. In the case of MLL-based comb, the dynamic range of f_r sweeping is limited. Therefore, the only way for MLL based combs to maximize resolution is to increase N or L. This has been done in previous works using the OSCAT method [36] [79] [80]. The main drawback of this approach is the requirement of a long delay fiber that imposes phase and timing variation between pulse pairs, which subsequently needs to be corrected using two reference FBGs [79]. On the other hand, the use of an EO comb, increases the dynamic range ($f_r . n_{step}$) in sweeping pulse repetition rate and thus achieves high-resolution from a short delay fiber (<15 m). The spectral resolution of such method is determined by the comb repetition frequency, the acquisition time is determined by the scan speed of the repetition rate sweeping mechanism, and the absolute wavelength accuracy of the Fourier spectrum is determined by the uncertainty of the carrier wavelength.

4.3 Experiment

Figure 4.3 shows the experimental implementation of the SCS. An EO comb is generated by phase modulation, chirp compression, and nonlinear mixing of a continuous wave signal at a wavelength of 1540 nm [81]. The EO comb consists of a pulse train with a repetition frequency of ~10 GHz. The pulse width is 10 ps, and its full spectral width at 10 dB from the maximum is 30 nm with an OSNR > 20 dB throughout. Figure 4.4 shows the spectrum of the OFC. This OSNR value is good enough for our application since the maximum absorption depth among the spectral samples used, is <10 dB.

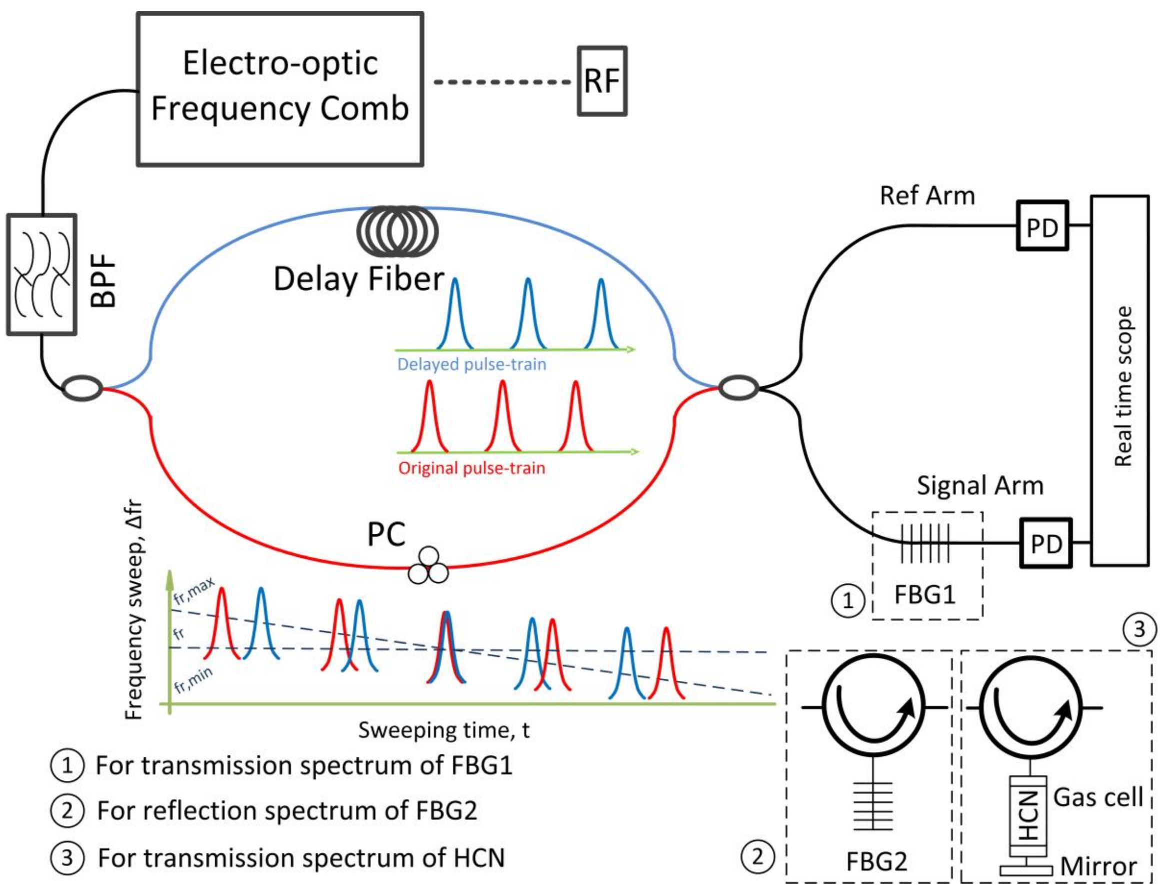

Figure 4.3. Experimental setup to demonstrate the concept of single comb spectroscopy with sweeping pulse repetition rate. Three samples are shown in the dashed boxes (FBGs and an $H^{13}C^{14}N$ gas cell) and numbered in accordance with the order of their presence in the article. BPF: Bandpass filter, PC: Polarization controller, FBG: Fiber Bragg grating, PD: Photodiode.

The repetition frequency is controlled by the sinusoidal signal of an RF clock generator and tunable over the 9-11 GHz range without significant change in optical bandwidth. Further reduction in repetition rate will reduce the optical bandwidth of the comb. A tunable bandpass filter truncates half of the optical spectrum from 1525 nm up to 1537 nm to prevent aliasing of spectroscopic measurement. Bandpass filtering would be unnecessary if an acousto-optic modulator were used in one arm, resulting in a two-fold increase in the effective bandwidth as is the case for EO dual comb systems [26] [77]. The filtered OFC signal is then sent to an imbalanced Mach-Zehnder interferometer (MZI). A polarization controller is used in one arm to maximize the beating signal amplitude at the output of the MZI. An optical fiber provides the net physical length difference between the MZI's arms, which is 12.15 m. After passing through the MZI, the resulting interferometric signal is divided into two halves, where one half is passed through the signal arm containing a spectroscopic sample to analyze, detected with a 100 MHz photodiode and recorded with a real-time oscilloscope of 1 GSa/s bandwidth. The other half of the interferometric signal is passed through the reference arm and detected by another photodiode to record the signal simultaneously without the sample.

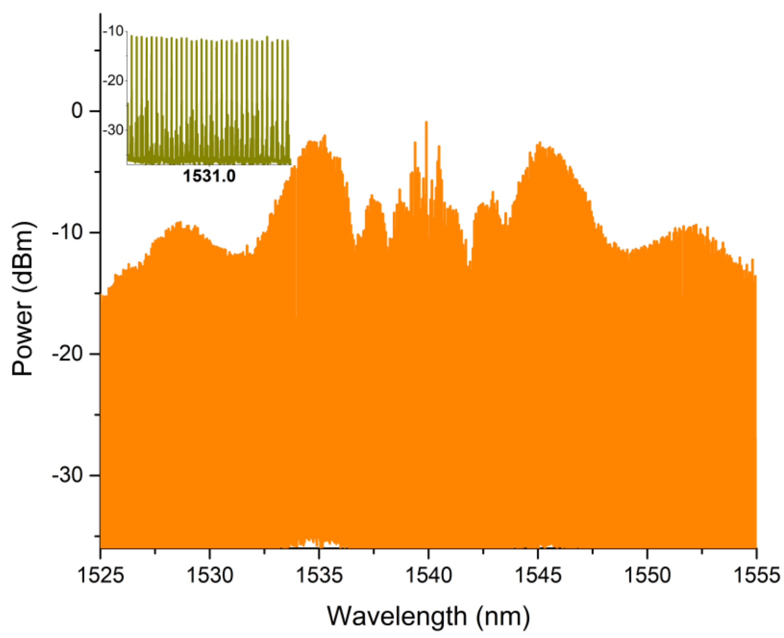

Figure 4.4. The spectrum of the 10 GHz EO frequency comb. The inset shows the zoomed in 2nm wide spectrum at 1531 nm, showing >20 dB OSNR.

The first analyzed sample is a fiber Bragg grating (FBG1) having a central wavelength of 1529.37 nm, an FWHM of 0.2 nm, and transmission depth of ~9 dB. The RF signal is swept from 10.010 GHz to 10.035 GHz in 1000 steps with a frequency step size of 25 kHz. At each frequency step, the oscilloscope records the optical power from the MZI output after passing through the sample. It forms an interferogram signal at the oscilloscope after one full scan, containing the transmission spectrum of the sample under test. A signal from the reference arm is also recorded at the oscilloscope simultaneously.

The second sample is FBG2, working in the reflection mode, thanks to a circulator. FBG2 has a central wavelength of 1529.33 nm, an FWHM of 0.3 nm and transmission depth of ~20 dB. After sweeping the RF signal, interferograms from both signal and reference arm are recorded by the oscilloscope.

The proposed spectroscopic system is also used to measure the transmission spectrum of an $H^{13}C^{14}N$ reference gas cell. For this purpose, a 16.5 cm long $H^{13}C^{14}N$ gas cell with a pressure of 25 Torr is inserted in the signal arm. A circulator and a fiber mirror are used for the incoming light to perform a double pass in the gas cell for increased sensitivity. Since each absorption line of $H^{13}C^{14}N$ has an FWHM ~2 GHz, the repetition frequency of the reference RF clock is reduced to 2 GHz and swept from 2.010 GHz to 2.050 GHz with a frequency step of 40 kHz. In this process, the total optical bandwidth gets reduced with respect to the configuration used to analyze the FBGs, resulting in an effective bandwidth of 1 nm after bandpass filtering. The central wavelength of the comb is shifted several times to cover 8 nm of spectral bandwidth, as explained in a later paragraph.

4.4 Results

Figure 4.5(a) shows the periodic interferograms recorded by an oscilloscope after passing through FBG1 in red and FBG2 in blue. The acquisition speed per interferogram is 4 seconds, which can be substantially reduced by optimizing the number of frequency scan steps or using analog frequency sweep. The acquired interferogram is low-pass filtered to filter out the noisy fluctuations by sampling at the effective time step according to equation (4.2). This is performed in MATLAB, using a moving average filter with a relative cut off frequency of 0.2. The interferogram is subsequently zero padded to smooth-out the peaks in the spectrum and apodized by multiplying with a triangular signal to minimize the oscillations of the spectral envelope. The resulting post-processed interferogram is shown in figure 4.5(b). The post-processed interferograms are then Fourier transformed to obtain the spectral response of the samples. The spectral resolution is set by the 10 GHz repetition frequency of the comb, which is fine enough to resolve the spectral signature of the FBG samples. This resolution is better than some dual comb counterparts reporting a measurement resolution of ≥ 20 GHz [26] [82].

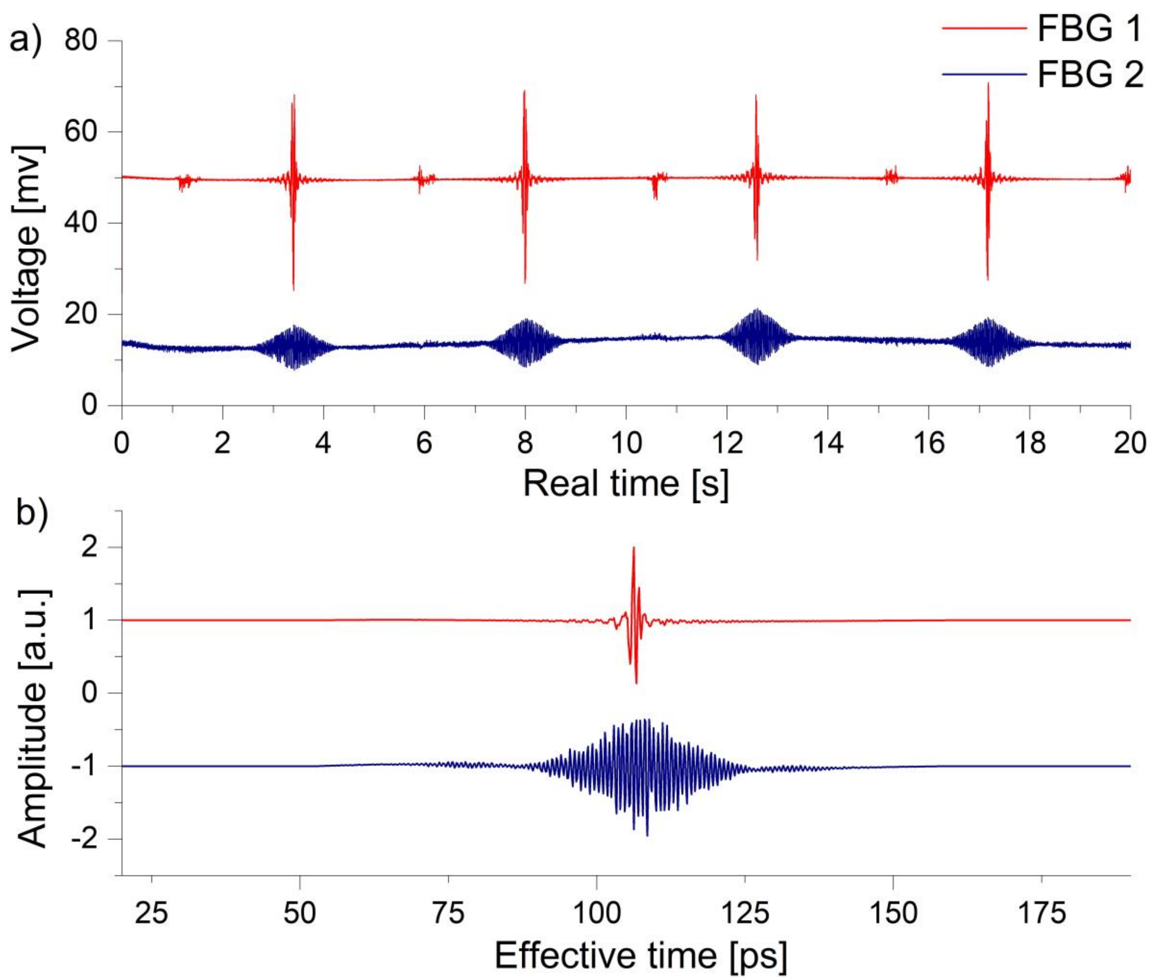

Figure 4.5. a) Periodic interferogram recorded in oscilloscope after both sample FBG1 and FBG2. b) Interferogram after low pass filtering, apodization, and zero-padding.

Figure 4.6 shows the retrieved spectra of FBG1 and FBG2 after Fourier transformation of the interferograms in figure 4.5(b). Figure 4.6(a) shows the total power transmitted by FBG1 and reflected by FBG2. The spectrum profile of FBG1 originates from the OFC envelope. The wavelength calibration is done from the carrier wavelength of 1540 nm, read directly from the CW laser module.The dip at a wavelength of 1529.37 nm with a depth of ~9 dB fits well with the expected transmission spectrum of FBG1. Multi-path interference produces small ripples observe on the spectrum but is accounted for by subtracting a reference spectrum without any sample present. Figure 4.6(b) shows the transmission spectrum of FBG1, as retrieved after subtracting a reference spectrum. The reflectance spectrum of the reference FBG2 is also provided in figure 4.6(a) with a peak at 1529.33 nm. Both center wavelengths and FWHM match well the values obtained with a high-resolution optical spectrum analyzer (*Yokogawa*), with an absolute wavelength accuracy of ±0.01 nm.

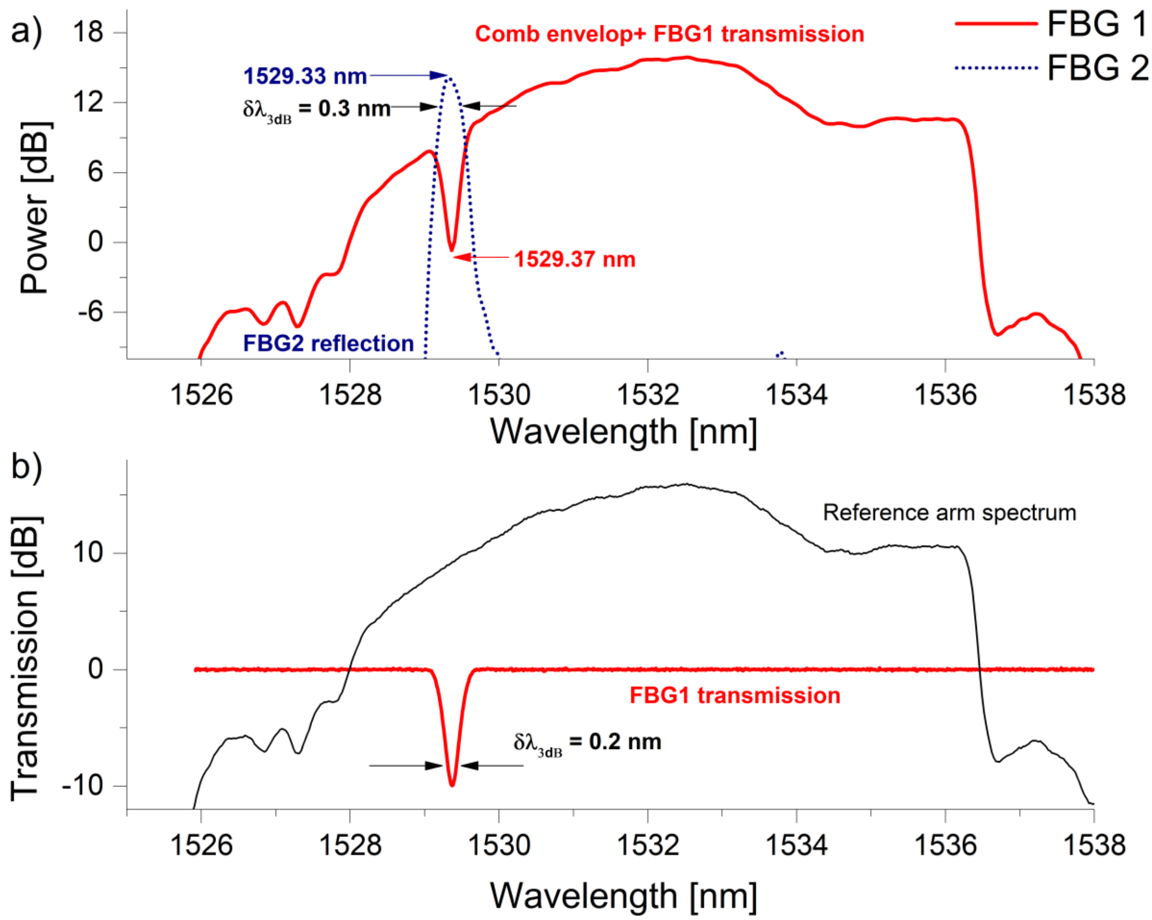

Figure 4.6. a) Resulting spectra after Fourier transforming the interferograms from figure 4.5b. FBG1 operates in transmission mode while FBG2 operates in reflection mode. b) The transmission spectrum of FBG1 is retrieved after subtracting the spectrum of the reference arm from the spectrum of the signal arm.

The calculated spectra are retrieved from a single interferogram without averaging. However, coherent averaging may be used to enhance the signal to noise ratio of the interferogram at the expense of longer acquisition time. The SNR increases as the square root of the number of averaged spectra (N_a). To measure the SNR, we consider 10 Fourier spectra with a total signal acquisition time of 40 seconds to measure the normalized standard deviation of the amplitude noise. The frequency domain SNR is inverse of the standard deviation and calculated to be SNR=50 for 10 averaged spectra over 15 nm of optical bandwidth (BW). The highest reported SNR for EO dual comb system was 2500 for 100 averaged spectra over a bandwidth of 0.5 nm [77]. When comparing the figure of merit (SNR*BW/√Na), the SCS method has almost twice the value. However, the effective acquisition speed of the dual-comb method is ~1 ms, that is faster than the

SCS method. The measurement accuracy of the wavelengths is dependent on the absolute wavelength accuracy of the carrier signal of the OFC. To increase the spectral resolution of the measurement, one must use a comb with lower repetition frequency, which ultimately limits the resolution of such a system. However, a smaller frequency spacing comes with a smaller bandwidth, leading to a tradeoff in-between spectral resolution and spectral range.

For the transmission spectrum analysis of the $H^{13}C^{14}N$ gas cell, the comb repetition frequency is set to ~2 GHz as required by the resolution of the transmission features of the sample. However, this leads to an optical bandwidth of 2 nm. To increase the wavelength range, that is, measuring the R2-R14 absorption lines of $H^{13}C^{14}N$ covering 1533-1541 nm, the carrier frequency of the OFC is shifted once every ~0.75 nm. In each section, four interferograms are coherently averaged to produce the final interferograms for both signal and reference arms. This pair of interferograms are then Fourier transformed to produce the corresponding spectra. The reference spectrum is subtracted from the signal spectrum to obtain the transmission spectrum for one section. All the sections are then combined after averaging the overlapping sections to obtain the complete transmission spectrum of the gas cell. Figure 4.7 shows the resulting transmission spectrum of the R2-R14 branches of $H^{13}C^{14}N$. The relative amplitudes of the 13 transmission dips match the transmission spectrum of the reference gas cell's datasheet [83]. After getting the transmission spectrum, the peak absorption wavelengths measured in the experiment are compared against their National Institute of Standards and Technology's (NIST) standard values. The experimental versus reference spectra differ by a maximum of ±9 pm. This discrepancy is attributed to the absolute wavelength accuracy of ±10 pm of the tunable laser that seeds the OFC. Thus, it can be assumed that with a precise measurement of carrier wavelength within ±1 pm, the measured value will match the NIST standards within an accuracy of < 1 part per million.

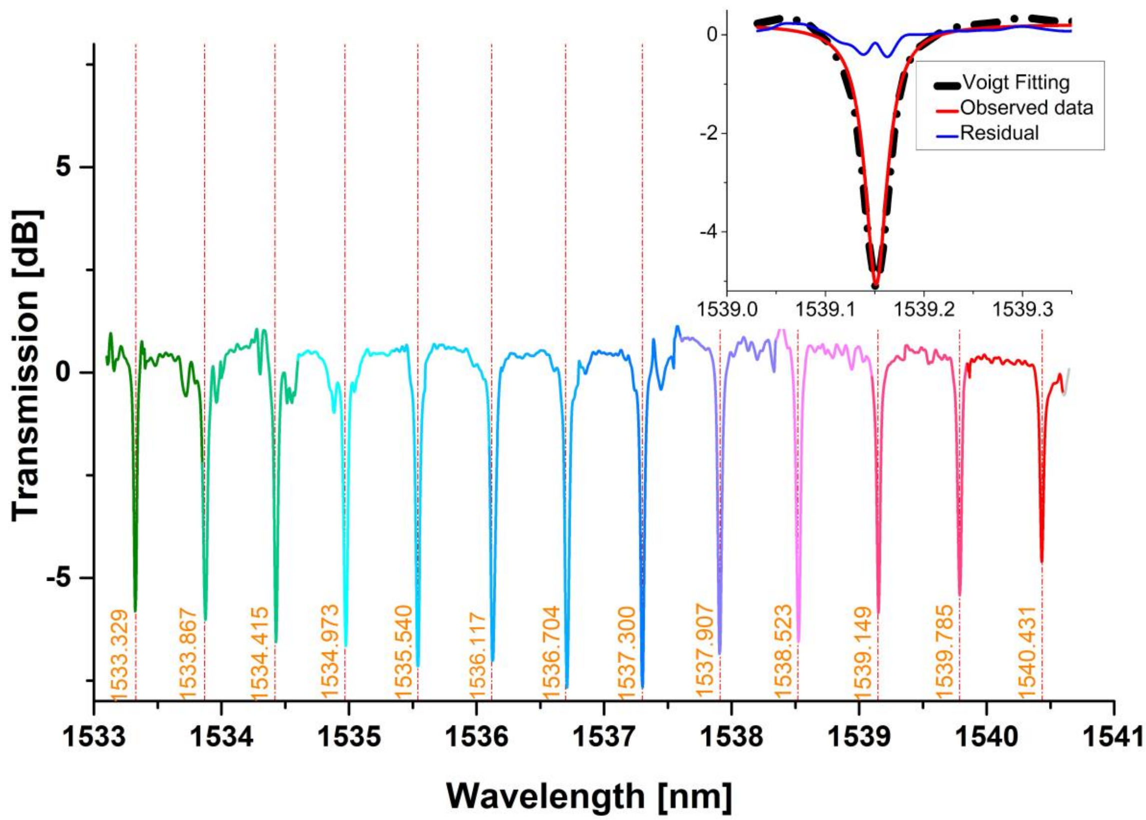

Figure 4.7. The transmission spectrum of the $H^{13}C^{14}N$ gas cell showing the absorption lines between R2-R14 branches. The vertical lines denote the true absorption wavelength value for each branch as per the NIST test data. The inset shows the Voigt fitting of the R4 branch and the corresponding residual curve. The residuals are calculated by subtracting the fitted values from the measured data.

4.5 Summary

In summary, we have shown that a spectrometer based on a single EO comb and a length imbalanced MZI successfully and accurately determines the spectral response of a chemical sample. Since it only uses one comb source, the system does not need to satisfy any strict phase-matching criterion. The use of one EO comb and a short length (~12 m) of delay fiber enable this measurement and bypass the requirement of two reference phase correction. EO combs are more flexible than mode-locked lasers in terms of tunability of the comb repetition rate and long-term stability in field deployment, which constitutes an advantage for comb-based spectroscopy. Unlike MLL based systems, the resolution of an EO comb and length imbalanced MZI system is not limited by the maximum path delay, rather by comb repetition rate like a dual-comb spectrometer.

The acquisition speed of the SCS method can be substantially improved by using analog sweep mode instead of step sweep when sweeping the frequency of the RF clock signal. In that case, the acquisition speed per interferogram will reduce to below 100 ms instead of 4 s reported in this chapter, making it comparable to a dual-comb spectrometer. In comparison with the so-called optical vector network analyzer technique [84], the SCS is faster and covers a broader spectrum. The optical sampling method involved in SCS can also be applied for distance measurement [85], glass index measurement [86], and depth-resolved imaging [87].

It should be noted that the slow drift of the effective length of the delay line in the OSCAT interferometer would cause a fringe shift in the interferogram signals if used for long term average. A time-shifted averaging of the interferograms would solve this issue because of the short length of the delay line.

Chapter V.

Dual Frequency Comb Spectroscopy

[4]In this chapter, we present a real-time dual-comb spectrometer operated from a bi-directional mode-locked fiber laser in the wavelength range of 1.9 µm. Two pulsed signals emitted from a common cavity ensures mutual coherence and common mode noise rejection. The resulting spectrometer operates without any complex electronic feedback system. High-resolution absorption lines of ambient water vapors are detected as a proof-of-concept demonstration.

5.1 Introduction

As mentioned in section 4.1, The field of Fourier transform spectroscopy has been transcended by the advent of dual-comb spectrometry (DCS) relying on a pair of OFCs with a slight mismatch in repetition rate [88]. Once superimposed, the two signals generate a cross-correlational interferogram due to pulse walk-off, analogous to traditional Fourier transform spectroscopy, as shown in figure 4.2. This allows real-time acquisition of high-resolution, time-resolved molecular spectra to detect, e.g., trace gases in the atmosphere [89]. The DCS system advantageously overcomes the need for a mechanical delay line in traditional Fourier transform spectroscopy and enables ultrafast acquisition of periodic interferograms with a high signal to

[4] The content presented in this chapter has been subjected to publication in **M. Imrul Kayes**, Nurmemet Abdukerim, Alexandre. Rekik and Martin Rochette "Free-running mode-locked laser based dual-comb spectroscopy," Optics Letters 43(23), 5809-5812 (2018).

noise ratio. The wide optical spectrum of two OFC containing the spectral signature of the sample gets mapped into the RF comb accessible by low-speed electronics. Therefore, real-time spectroscopy over a broad optical bandwidth is possible by mixing a pair of OFCs in a simple configuration. A dual-comb spectrometer combines many advantages offered by both broadband spectroscopy and tunable laser spectroscopy [39]. However, for high-resolution DCS, a strong phase relationship linking the OFC pair is required to resolve fine molecular absorption lines. The linewidth of the heterodyne beat signal of the comb pairs must be negligible with respect to the repetition rate difference (Δf_{rep}) between the two combs. To solve this problem, locking the phases of the two OFCs to a cavity-stabilized continuous wave laser was proposed in 2010 [90]. Since then, many works on DCS have followed this approach to perform high-resolution spectroscopy (50-100 MHz) with absolute frequency reference. However, this process requires an electronic phase-locking feedback system that is sophisticated, expensive, and bulky, limiting the applications when targeting out-of-lab environments.

Therefore, the need to simplify DCS systems has gained considerable attention in the past few years. Different methods like self-referenced OFCs [91], adaptive sampling [75], electro-optic comb generation [92] [93], and post-processed phase correction [94] have been used to address this issue. Electro-optic based systems like single comb spectroscopy with sweeping repetition rate also address this issue at the expense of longer acquisition time, as described in chapter 4 [67]. More recently, a novel trend that greatly simplifies the phase locking mechanism has emerged where two free-running OFCs with an offset repetition rate are produced from a single bi-directional mode-locked laser cavity [95] [96]. In another approach, phase coherent free-running dual combs are generated from a dual-wavelength mode-locked laser [97] [98]. In most of the recently reported works, such free running DCS systems have been demonstrated in the C-band using Erbium-doped fiber lasers incorporating carbon nanotubes (CNTs) as saturable absorber [16] [97]. However, dual-comb spectroscopy at longer wavelengths is more desirable since many important gases have their molecular fingerprints in the spectral region of 1.8-2.0 μm. While CNTs are nowadays widespread, one needs to deposit single well CNTs to a fiber tip to make an operational saturable absorber, which is a complex process that warrants sophistication and precision.

In this chapter, we demonstrate a dual-comb spectrometer based on a bi-directional Thulium laser that is mode-locked by a semiconductor saturable absorber mirror (SESAM). The bi-directional laser produces two counter-propagating pulse trains with an offset repetition rate. They serve as a phase-coherent optical source pair for dual-comb spectroscopy of ambient water vapor at 1.9 µm. Both the wavelength and frequency offset of the laser are adjustable, making the system flexible in terms of measurable optical bandwidth and acquisition speed.

5.2 Theory of Dual-comb Spectroscopy

When the signal of two OFCs with an offset repetition rate are superimposed, their adjacent spectral lines beat with each other upon conversion to the radio-frequency (RF) domain. As a result, optical spectrum information is transferred to the RF domain, as depicted in figure 5.1.

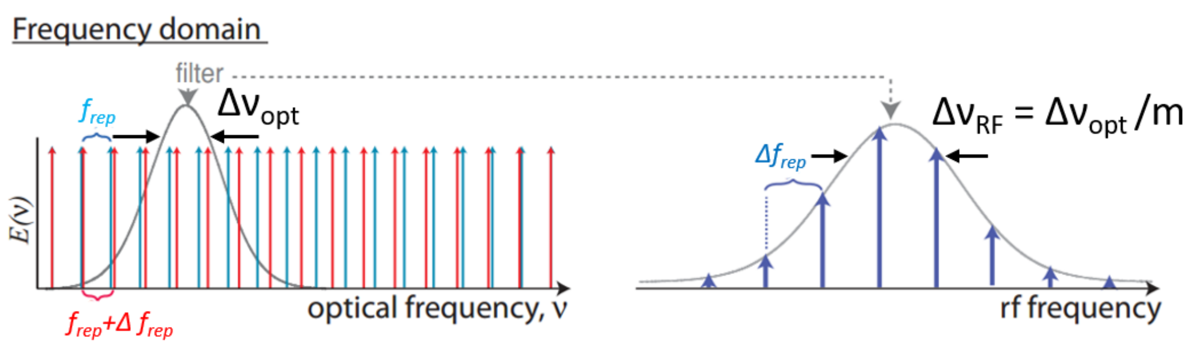

Figure 5.1. Principle of the dual-comb spectroscopy in the frequency domain [99].

If the repetition rate of the primary OFC is f_{rep} and offset repetition rate is Δf_{rep}, then the optical bandwidth $\Delta\nu_{opt}$ is compressed into an RF bandwidth of $\Delta\nu_{RF}$, which is given by,

$$\Delta\nu_{RF} = \frac{\Delta\nu_{opt}}{m} \tag{5.1}$$

where, $m = f_{rep} / \Delta f_{rep}$, is the compression factor. To maintain a one-to-one mapping between the modes of both optical and RF combs, the maximum RF comb frequency is determined by $f_{rep}/2$ (Nyquist condition), which results in the anti-aliasing optical bandwidth [88] [100],

$$\Delta\nu_{RF} < \frac{f_{rep}}{2}$$

$$\Delta\nu_{opt} < \frac{mf_{rep}}{2} = \frac{{f_{rep}}^2}{2\Delta f_{rep}} \tag{5.2}$$

On the other hand, the relative linewidth between the two OFCs must be smaller than Δf_{rep}, which sets the phase matching condition for DCS. Moreover, the resolution of the DCS is determined by the repetition rates of the OFCs. Therefore, OFCs with megahertz repetition rate offer ultra-high-resolution spectroscopy, something that is out of reach for diffraction optics or traditional FT spectroscopy. Conventionally, free-running mode-locked lasers are stabilized through a complex phase-locked loop and absolute frequency referencing to satisfy this condition. There exists a much simpler solution to satisfy the phase matching condition. If two OFCs were to source from a common laser cavity, this would induce an inherent phase relationship between them. By rejecting the common mode noise, their beat frequency would have a small relative linewidth [97]. Such passive coherence of a bi-directional mode-locked laser can be harnessed for dual-comb spectroscopy at 1.9 μm.

5.3 Bi-directional Mode-locked Laser

5.3.1 Experimental Setup

Figure 5.2 shows the experimental setup of a bidirectional mode-locked laser. Bidirectional mode-locking is enabled from the combined effects of a SESAM and nonlinear polarization rotation. The SESAM has a surface area of 16 mm^2, a modulation depth of 26% and a saturation fluence of 65 μJ/cm^2. The amplifying fiber is an 18 cm long thulium-doped double-clad silica fiber, bi-directionally pumped by C-band laser sources through wavelengths division multiplexers. Two 80/20 fiber couplers separate two propagation directions in the cavity. They also serve as output couplers to extract pulses in each direction. A polarization controller and a polarizing isolator are placed on each path for nonlinear polarization rotation. Two optical circulators are used to send light from both clockwise (CW) and counterclockwise (CCW) direction onto a common SESAM in a butt-coupled configuration. In each propagation direction, 80% of the power is coupled out while 20% is fed-back to the cavity. A 2 m long normal dispersion fiber (NDF) reduces the net group velocity dispersion of the cavity at a level of -0.67 ps^2. This anomalous dispersion enables soliton pulse shaping. The total cavity length is L=12.4 m for both directions, resulting into a free spectral range of FSR=16.57 MHz. The round-trip length of each direction can be changed independently by changing the fiber lengths in between 80/20 couplers, which consequently results in different repetition rate. The laser cavity is pumped by ~0.6 W of power in both directions, and proper adjustment of the polarization controllers leads to bidirectional mode-locking. Both spectra of the bidirectional laser are independently monitored using two optical spectrum analyzers (OSA). Temporal signals and electric spectra of the lasers are monitored using a photodetector, oscilloscope, and electric spectrum analyzer [101].

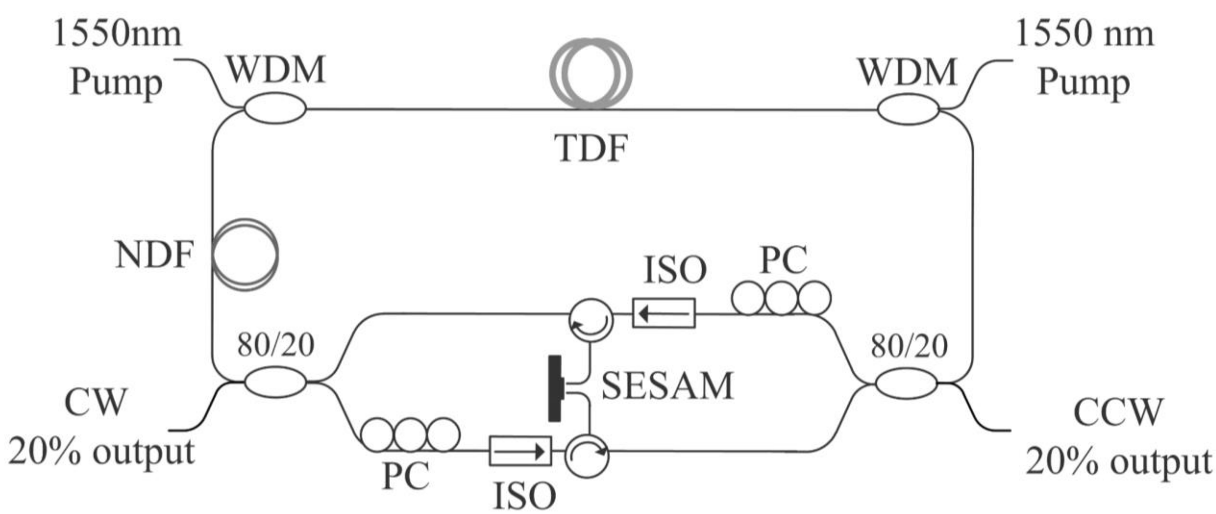

Figure 5.2. Experimental setup for dual-comb generation by bi-directional mode-locking. WDM: Wavelength division multiplexer, TDF: Thulium-doped fiber, NDF: Normal dispersion fiber, PC: Polarization controller, ISO: Polarizing isolator, SESAM: Semiconductor saturable absorber mirror.

5.3.2 Results

Figure 5.3(a) shows the superimposed output spectra of the bidirectional laser as observed from the OSAs. The central wavelengths bandwidth of the CW and CCW signals are 1911 nm and

1913 nm, respectively. The 3-dB bandwidth of the CW and CCW signals are 2.8 nm and 3 nm, respectively. Output wavelengths are slightly tunable by adjusting polarization controllers or the incidence beam angles on the SESAM.

Figure 5.3(b) shows the electrical spectra of the laser output in the CW direction. Insets show the electrical spectra at the fundamental repetition rates measured with a resolution bandwidth of 30 Hz. The repetition rates for CW and CCW direction are 16.5670 MHz, and 16.5713 MHz, respectively. The measured difference in repetition rate is ~1.3 kHz. Signals from both directions are combined with a 3-dB coupler and monitored both in time and frequency.

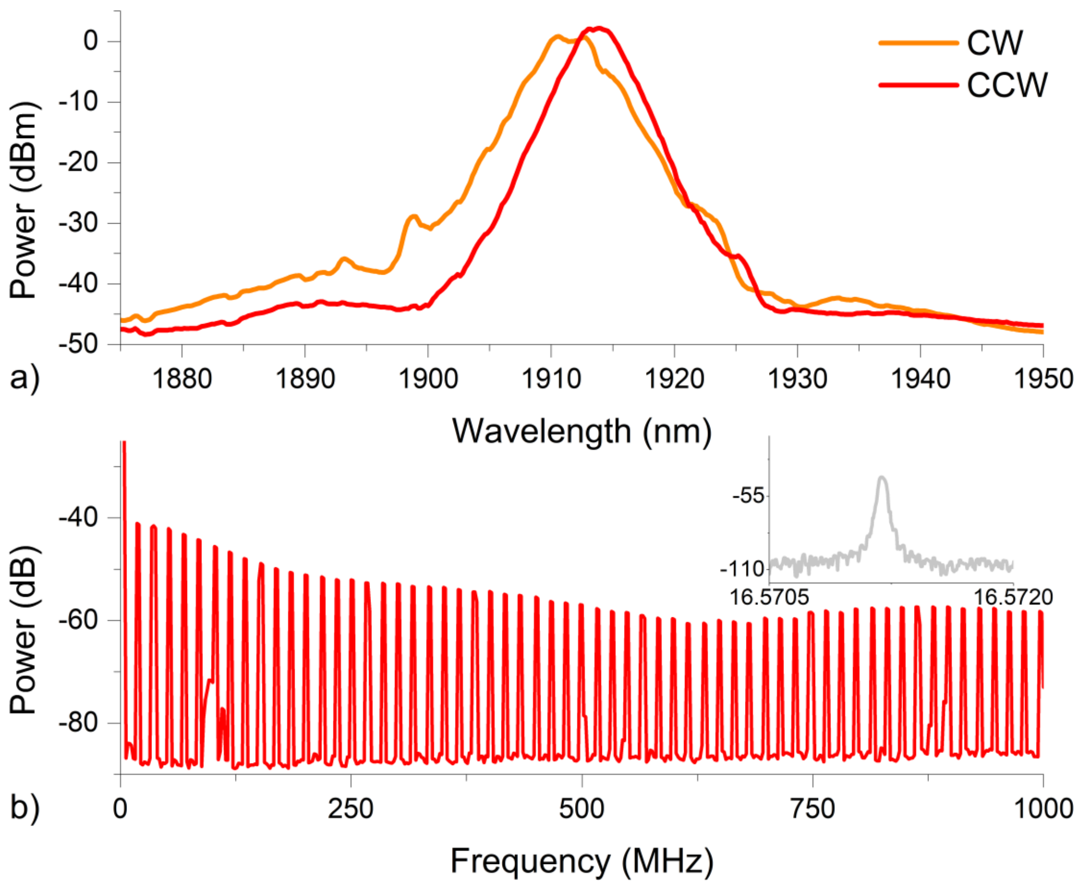

Figure 5.3. a) The optical spectrum of the lasers in both direction with 2-nm RBW. b) Electrical Spectrum of counter-clockwise laser output. The inset shows the spectrum at the fundamental repetition rate.

Figure 5.4(a) shows the spectrum of the combined signal on an electrical spectrum analyzer. The electrical spectrum shows the newly generated RF combs with a line spacing of Δf_{rep}. Figure 5.4(b) shows the stability of the beat frequency Δf_{rep} measured in one-minute intervals over 10 minutes with 1s sweep time. Even though f_{rep} for both directions changes over time, their difference (Δf_{rep}) remains stable with a standard deviation of 1.5 Hz due to common noise rejection. It shows excellent mutual coherence between the two lasers.

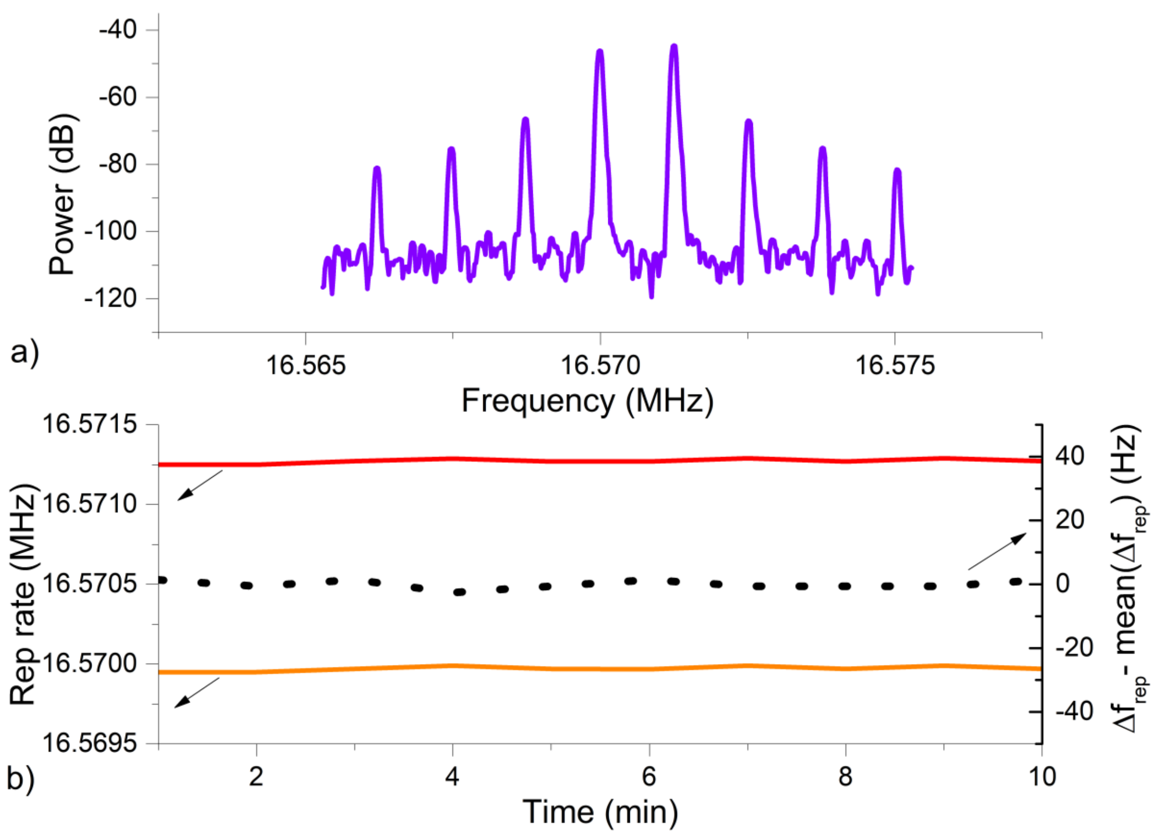

Figure 5.4. a) Electrical Spectrum of the beat signal of the two OFC. b) Stability analysis of the beat signal observed over 10 minutes.

5.4 Dual-comb Spectroscopy

5.4.1 Experimental Setup

Signals from the bi-directional laser are combined with a 3-dB coupler and then amplified using a Thulium-doped fiber amplifier. This broadens the combined spectra due to the third-order nonlinear effect and ensures an improved spectral overlap between CW and CCW signal. Since the fundamental repetition rate of the laser is ~16.57 MHz with a difference in repetition rate of 1.3 kHz, the un-aliased optical bandwidth is ~1.5 nm. To prevent aliasing, the optical bandwidth is limited by sending the dual-comb signal through a tunable bandpass filter before photodetection and interferogram recovery. The free-space portion within the optical filter also acts as an ambient air sample containing water vapor at one atmospheric pressure and 50 cm of path length. Since water vapor has strong absorption resonances in the 1.9 μm band, it serves here as a reference gas sample for the current dual-comb spectroscopy experiment. The complete dual-comb spectrometer setup is shown in figure 5.5. It should be noted that the free-space portion of the SESAM is less than 1 cm, which is negligible compared to the free-space path in the filter.

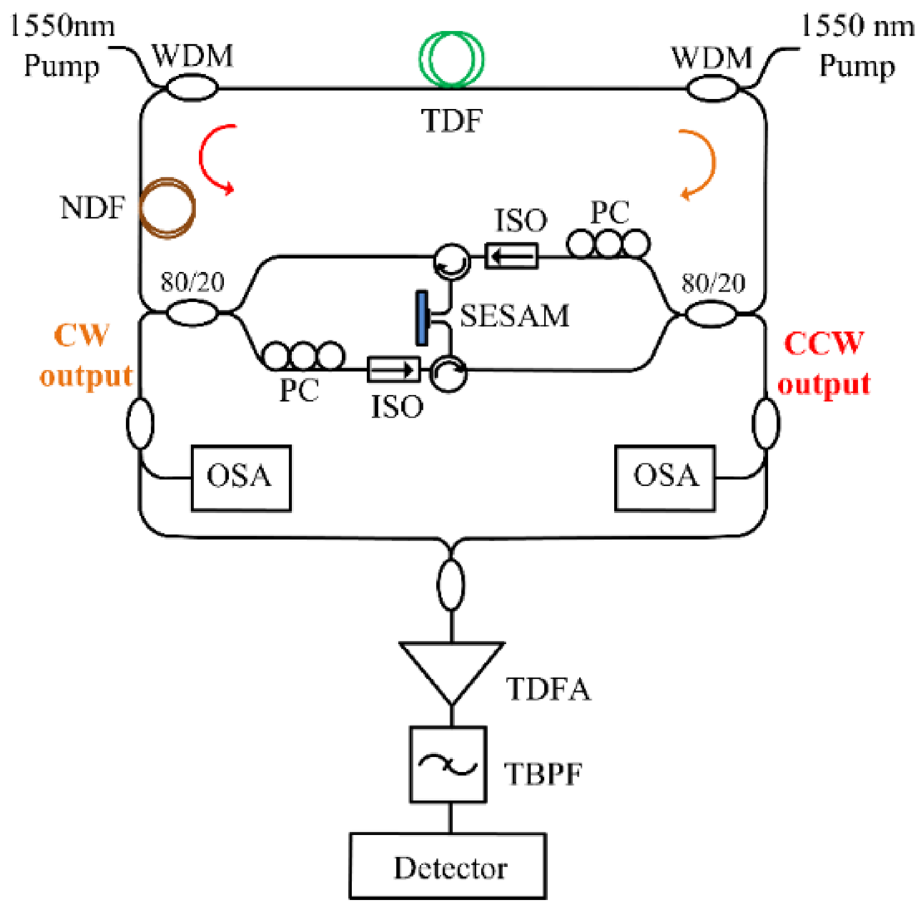

Figure 5.5. Experimental diagram of the complete dual-comb spectrometer. The free-space optical filter acts as an ambient water vapor sample for spectroscopy. TDFA: Thulium-doped fiber amplifier, TBPF: Tunable band-pass filter.

Figure 5.6(a) shows the spectrum of the combined dual-comb signal after amplification. It also shows the resulting spectra after band-pass filtering at two different central wavelengths. Figure 5.6(b) shows the periodic raw interferograms taken from the real-time oscilloscope sampled at 500 MSa/sec. The time scale of this series of interferograms is in milliseconds, characterized by a sampling interval of $1/f_{rep}$, corresponding with the RF domain.

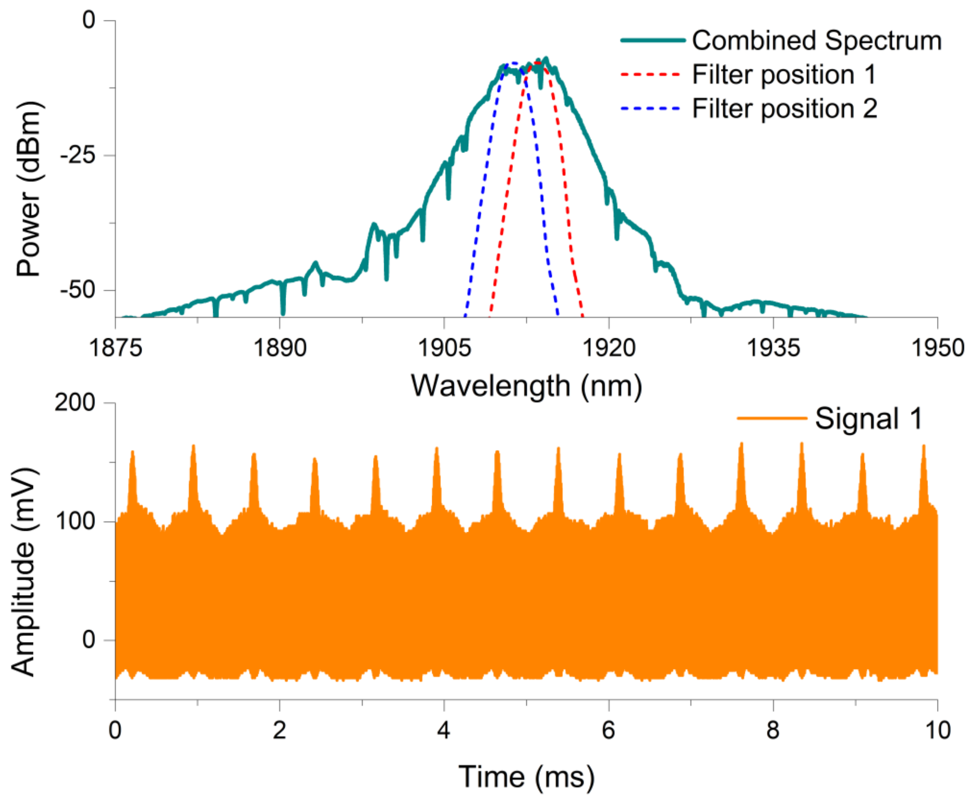

Figure 5.6. a) Optical Spectrum after combining the two lasers and the position of the passband of the tunable filter. b) Periodic interferograms recorded with a real-time oscilloscope.

5.4.2 Results

Each interferogram is truncated centrally by a 127 μs time window. These truncated interferograms are filtered and resampled in MATLAB post-processing to remove high-frequency noise. Then an effective time scale is generated by dividing the real-time scale by the compression factor, m. This time scale corresponds with the optical frequency domain, characterized by a much smaller sampling interval of $\Delta f_{rep}/f_{rep}^2$. A total of ~1300 interferogram peaks are captured within 1 sec. By taking the first peak as a reference, all the other peaks are aligned to perform time-shifted averaging. For alignment, an interferogram frame is cross-correlated with the reference frame. It gives the information by how much the frame is lagging or leading the reference frame. The alignment process is complete after shifting the frame by an appropriate amount. Figure 5.7(a) shows the final interferogram obtained upon aligning all the interferogram peaks and averaging them. The averaged interferogram has a temporal scale of 10 ns which sets the theoretical instrumental resolution to be ~100 MHz. Figure 5.7(b) shows the relationship between the number of averaging and time domain signal to noise ratio (SNR) of the interferogram. This result demonstrates excellent mutual coherence of the bidirectional laser, which is suitable for dual-comb spectroscopy. After that, the interferogram is Fourier transformed to obtain the spectrum with the spectroscopic features.

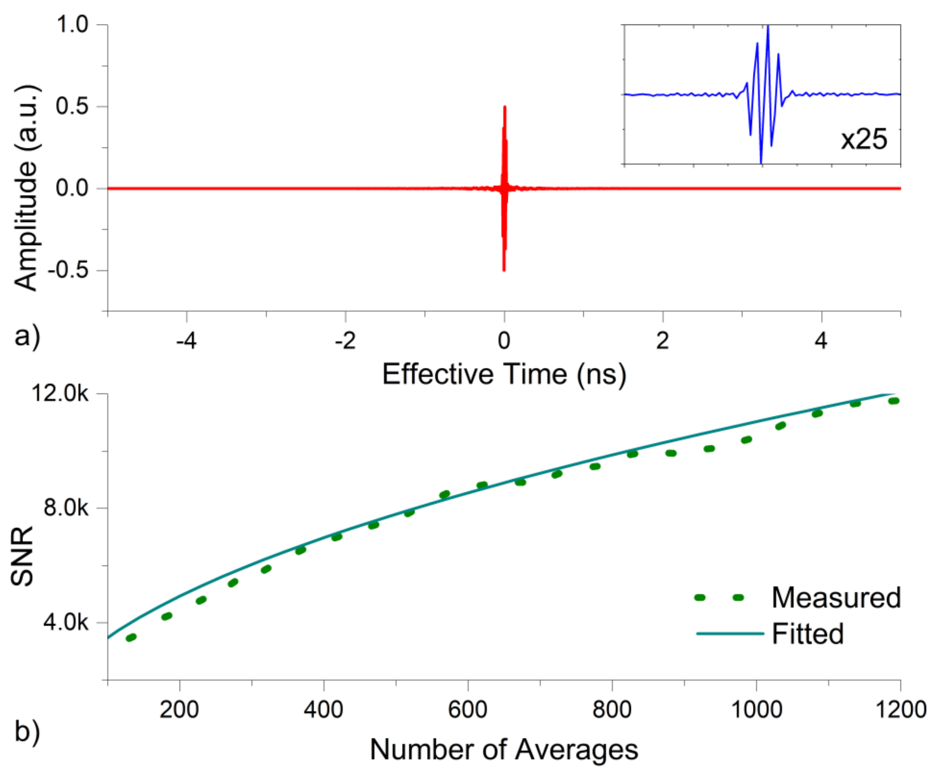

Figure 5.7. a) Final interferogram after time-shifted averaging of ~1300 interferogram frames captured in 1 s. b) Evolution of the interferogram's SNR with the number of averaged interferograms (N_{avg}). The fit shows that SNR varies with $\sqrt{(N_{avg})}$ demonstrating passive mutual coherence.

Figure 5.8 shows the Fourier transformed spectra of the post-processed interferograms for two different passbands of the tunable filter. The shape of the spectra resembles the Gaussian shape of the filter passband. The dips present on the spectrum are because of water vapor absorption line between 1910-1915 nm. Ideally, an absorption-free reference spectrum is needed to retrieve the transmission spectrum of the sample, which is not possible in our case. As an alternative, the transmission spectrum is retrieved by taking the Gaussian shape approximation of the optical filter passband and subtracting it from our calculated spectrum. However, this will distort the absolute amplitude and linewidth of the absorption lines to some extent. The inset shows the calculated transmission spectrum, where several absorption lines are present. It is important to note that this method does not have any absolute frequency referencing. So, the measured wavelength of the absorption lines will not be accurate. To retrieve the original frequency of the absorption lines, the measured transmission spectrum is calibrated with the standard HITRAN absorption data across 1909-1916 nm using cross-correlation analysis [98]. The inset also shows the corresponding absorption lines from the HITRAN database [102].

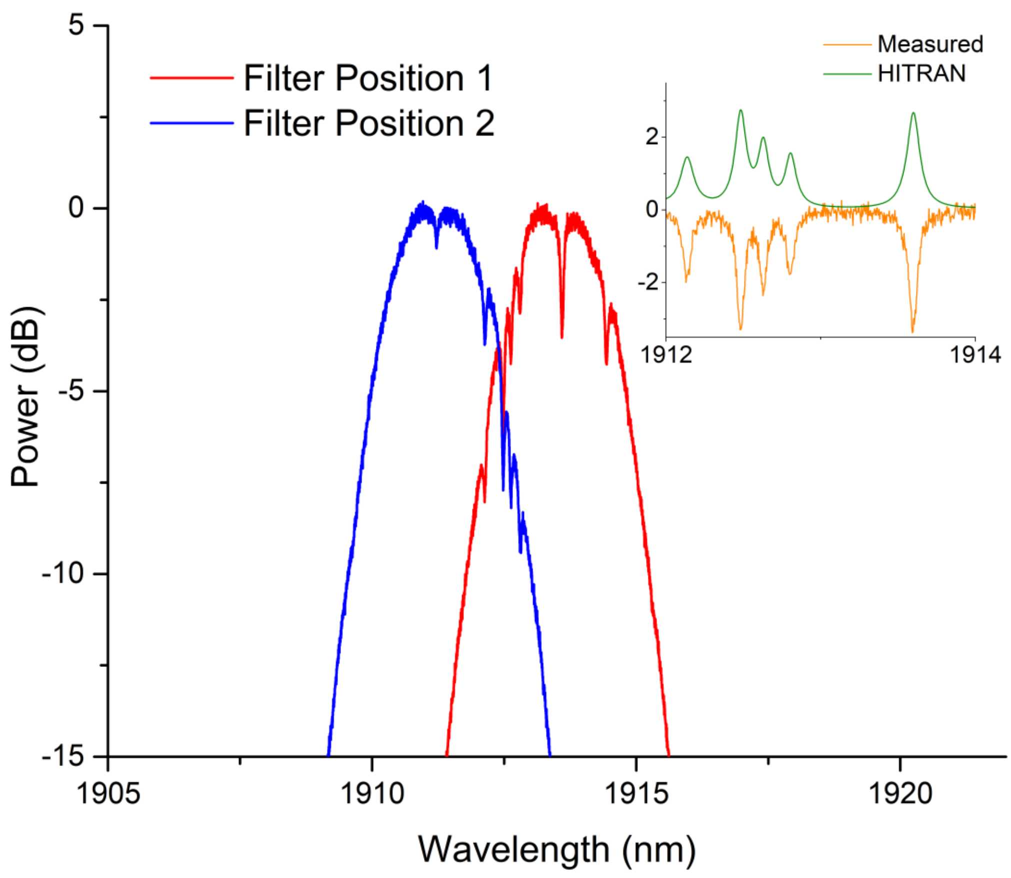

Figure 5.8. Calculated spectrum after Fourier transforming the interferogram. The spectrum shows the Gaussian shape of the filter passband containing water absorption lines. The inset shows the transmission spectrum of the water vapor along with corresponding HITRAN spectrum.

5.5 Summary

In summary, we have demonstrated the application of a dual-comb spectrometer at 1.91 μm using a free-running bidirectional thulium fiber laser. Because they share a common cavity, laser signals from both directions reject the common mode noise to produce a stable beat frequency over a long period of time. Therefore, high-resolution dual-comb spectroscopy is made possible with such free-running combs without resorting to complex and expensive electronic feedback systems. Our method achieves 100 MHz spectral resolution with a detectable optical bandwidth of 5 nm. The SNR is calculated to be 12000 when averaging 1300 interferograms in 1 s of acquisition time. There is only one other reported work on free running dual-comb spectroscopy around 2 μm, based on a dual-wavelength MLL. It reported a resolution of 72 MHz with 4 nm optical bandwidth. The SNR was reported to be 10400 after averaging 3000 interferogram frames in 1s. Therefore, our method performs better in terms of SNR and bandwidth.

It should be noted that, since we are using free-running combs without active stabilization, the slow drift of f_{rep} may affect the maximum achievable resolution, despite a stable Δf_{rep}. This method can be modified to access longer wavelengths by a nonlinear broadening of the combs' spectra. For a single-shot measurement of such broadband optical coverage, the offset frequency should be in the Hz level—easily realizable by matching the optical path lengths of both propagation directions. With long-term averaging and nonlinear broadening, this method holds great promise for molecular spectroscopy in the mid-infrared.

Chapter VI

Conclusion & Future Works

This thesis represents the author's research endeavors over the past four and a half years on developing frequency combs and finding their application in spectroscopy and optical metrology. The mutual coherence among the spectral lines of a frequency comb makes it a perfect tool for numerous applications. The objective of the author's doctoral research was to investigate novel methods of synthesizing frequency combs at different wavelengths and find suitable applications harnessing the unique characteristics of each type of frequency combs. Even though there has been some breakthrough with the frequency combs in the field of optical clocks and dual-comb spectroscopy, its potential for other applications are still untapped and nonetheless, promising. Hopefully, this thesis will serve as a forerunner towards unlocking the full potential of frequency combs in the near future.

In this thesis, firstly, the synthesis of an electro-optic frequency comb from a low-noise Brillouin fiber laser was presented. The linewidth narrowing effect of stimulated Brillouin scattering was exploited to create a CW seed laser with ultra-narrow linewidth for the synthesis of the comb. Then, the combined effect of phase modulation, chirp compensation, and nonlinear mixing converted the CW laser into a 32-nm wide frequency comb with a repetition frequency of 8 GHz. The narrow linewidth of the seed laser improved the linewidth of the resulting frequency comb, which was characterized using a self-heterodyne technique. Secondly, the application of such EO frequency combs for precision distance measurement was demonstrated. A combination of repetition rate modulation and length imbalance interferometer was used in a modified OSCAT configuration to determine the absolute length of a delay module. The advantages of EO combs over MLLs for this technique were explained in terms of the broader dynamic range of repetition rate sweeping, which enables improved and faster measurement of distance. This technique also enabled motion tracking of moving objects, as demonstrated by measuring the speed of a motorized delay module. The accuracy of the distance measurement method was limited by the uncertainty of the repetition frequency and measured to be 5 μm. Thirdly, the application of EO combs in Fourier transform spectroscopy was explored using a length imbalance interferometer. The proposed method was capable to successfully measure the spectral response of an HCN gas sample between 1533-1541 nm using a single EO comb without any phase matching requirement. The broad sweeping range of repetition frequency and use of a short delay fiber enabled this spectrometer to perform high-resolution measurement without any phase-correction of the interferograms. The resolution of the proposed method was limited by the repetition frequency of the comb, unlike MLL based systems. The comparison between the measured absorption lines of the gas sample with the reference data indicated excellent agreement. Finally, a dual-comb spectrometer at 1.9 μm was presented that uses a free-running bi-directional MLL laser to bypass the stringent phase matching requirement of dual-comb spectroscopy. Using a combination of Thulium doped gain medium, nonlinear polarization rotation and semiconductor saturable absorber, a novel MLL resonator was designed which is capable of mode-locking two counter-propagating fiber lasers. Due to sharing a common cavity, both lasers had a passive mutual coherence resulting from common mode noise rejection. Therefore, high-resolution dual-comb spectroscopy was made possible with a free-running mode-locked laser that does not require any active stabilization scheme to satisfy the phase matching criterion. This method enabled a simplified and inexpensive implementation of dual-comb spectroscopy to detect absorption lines of the water molecules in ambient air.

The comb generation technique described in this thesis is in the near infrared region-mainly at the wavelengths of 1.55 μm and 1.91 μm. The most attractive window for molecular spectroscopy is in the mid-infrared (> 2.5 μm) region which contains the molecular fingerprints of many greenhouse gases. Therefore, it would be useful to synthesize EO combs and bi-directional MLLs in the mid-infrared region for spectroscopy. However, it is challenging to generate EO combs at longer wavelength due to the unavailability of suitable EO modulator and fibers. One suggestion is to use a specialty optical fiber with engineered dispersion and nonlinearity to transfer the 1.55 μm EO combs to longer wavelength using parametric wavelength conversion. For bi-directional MLLs, it is possible to use ZBLAN fibers as a gain medium, and spin coated CNTs as a saturable absorber for generating MLLs at 2.7 μm. This will enable dual-comb spectroscopy in mid-infrared, and possibly even longer wavelengths. It is possible to generate a 3D image of a target using the high-resolution LIDAR system described in chapter 3. A 2D mechanical raster scanning setup for beam steering and lens system for optimum beam focusing are two of the major challenges for building such an imaging system. Applications like surface roughness modeling and depth sensing would greatly benefit from such 3D mapping systems.

Appendix A.

Frequency comb generation in optical fiber-1

```
%%%%%%%%%%%%%%%%%%%%%%%%%%%%%%%%%%%%%%%%%%%%%%%%%%%%%%%%%%%%%%%%%%%%%%%%%
clear all, close all

%% This is the latest code for frequency comb simulation

% SETTINGS
DimEcran = get(0,'ScreenSize');
Dx = 0.40; Dy = 0.7;
PosFig  = [(1-Dx)*DimEcran(3),(0.9-
Dy)*DimEcran(4),Dx*DimEcran(3),Dy*DimEcran(4)];
set(0,'DefaultFigurePosition',PosFig)
AFS = 18;   LFS = 18;   TFS = 18;   %Axis, label and title font size
set(0,'DefaultLineLineWidth',2)

% FUNCTIONS
FT = inline('DTime*fftshift(fft(ifftshift(AtIn)))','AtIn','DTime'); %Fourier
transform
Pf = inline('DFreq*(abs(AfIn)).^2','AfIn','DFreq');                %Power
spectral density (in frequency)
IFT = inline('1/DTime*fftshift(ifft(ifftshift(AfIn)))','AfIn','DTime');
%Inverse Fourier transform
Pt = inline('(abs(AtIn)).^2','AtIn');                              %Power
(in time)
%%%%%%%%%%%%%%%%%%%%%%%%%%%%%%%%%%%%%%%%%%%%%%%%%%%%%%%%%%%%%%%%%%%%%%%%%
%% Features

amp_mod=11;  %% put 1 for Quasi CW

c0 = 3e8;
```

```
%%%%%%%%%%%%%%%%%%%%%%%%%%%%%%%%%%%%%%%%%%%%%%%%%%%%%%%%%%%
% EXPERIMENTAL CONDITIONS
%%%%%%%%%%%%%%%%%%%%%%%%%%%%%%%%%%%%%%%%%%%%%%%%%%%%%%%%%%%
% Input signal : Clock pulses
Lambda0 = 1550e-9;      Freq0 = c0/Lambda0;         k0 = 2*pi/Lambda0;
Tfwhm = 10e-12;         T0 = Tfwhm/(2*sqrt(log(2)));
RepRate = 10e9;


PeakPowerIn = 500e-3;         %W

%%%%%%%%%%%%%%%%%%%%%%%%%%%%%%%%%%%%%%%%%%%%%%%%%%%%%%%%%%%
% TIME-FREQUENCY VECTORS
%%%%%%%%%%%%%%%%%%%%%%%%%%%%%%%%%%%%%%%%%%%%%%%%%%%%%%%%%%%
NSamp = 5e4+1;
DTime = 0.25e-12;
VTime = (-(NSamp-1)/2:(NSamp-1)/2)'*DTime;
TWindow = NSamp*DTime;

MaxFreq = 0.5/DTime;
DFreq = 2*MaxFreq/(NSamp-1);  % originally was 2
VFreq = (-(NSamp-1)/2:(NSamp-1)/2)'*DFreq;
VLambda = VFreq*Lambda0^2/c0;


%%%%%%%%%%%%%%%%%%%%%%%%%%%%%%%%%%%%%%%%%%%%%%%%%%%%%%%%%%%
% GAUSSIAN PULSE DEFINITION
%%%%%%%%%%%%%%%%%%%%%%%%%%%%%%%%%%%%%%%%%%%%%%%%%%%%%%%%%%%

UtIn=ones(size(VTime));           % CW signal

%UtIn = exp(-0.5*(VTime./T0).^2);        % Unitary field envelope
EtIn = sqrt(PeakPowerIn)*UtIn;          % Field envelope
%EtIn= sqrt(EtIn.*EtIn+1*PeakPowerIn/10);

%EtIn=EtIn+circshift(EtIn,25)+circshift(EtIn,-
25)+circshift(EtIn,50)+circshift(EtIn,-50);




%% Amplitude modulation
if amp_mod==1
famp=50e6;
%EtIn=EtIn.*cos()
Samp=(square(2*pi*famp*VTime)+1)/2;
EtIn=EtIn.*Samp;
end

PhaseInT = unwrap(angle(EtIn));
ChirpIn = diff(PhaseInT)/(DTime);   ChirpIn(NSamp)=0;
```

```
PowerIn = Pt(EtIn);

EfIn = FT(EtIn,DTime);


PsdIn = Pf(EfIn,DFreq);                    %W/Hz

    figure,set(gca,'FontSize',AFS)
    subplot(2,1,1),plot(VTime,PowerIn,'k-')
    title('Temporal signal','fontsize',TFS)
    xlabel('Time [s]','fontsize',LFS), ylabel('Power [W]','fontsize',LFS)
    ylim([0 1]),xlim([-1.5e-8 1.5e-8])
    subplot(2,1,2),plot(VFreq,dB(PsdIn),'k-')
    title('Spectral signal','fontsize',TFS)
    %xlim([-1e11 1e11])
    xlabel('Frequency [Hz]','fontsize',LFS), ylabel('PSD
[dB]','fontsize',LFS)


%% phase modulation
frf=1*8e9; % Phase modulation frequency
m=1;   % modulation depth

Etpm=EtIn.*exp(-1i*pi*m*sin(2*pi*frf*VTime));  % E field after PM
PowerIn = Pt(Etpm);
Efpm = FT(Etpm,DTime);
PsdIn = Pf(Efpm,DFreq);

figure,set(gca,'FontSize',AFS)
    subplot(2,1,1),plot(VTime,PowerIn,'k-')
    title('Temporal Phase modulated signal','fontsize',TFS)
    xlabel('Time [s]','fontsize',LFS), ylabel('Normalized Power
[W]','fontsize',LFS)
  %  ylim([0 1]),
   %xlim([-4e-9 4e-9])
    subplot(2,1,2),plot(VFreq,dB(PsdIn/max(PsdIn)),'k-')
    title('Spectrum of Phase modulated signal','fontsize',TFS)
   % xlim([0 2e9])
    ylim([-30 1])
    xlabel('Frequency [Hz]','fontsize',LFS), ylabel('Power
[dB]','fontsize',LFS)


EtOut=Etpm;
EfOut=Efpm;
PowerOut=PowerIn;
PsdOut=PsdIn;
% %%%%%%%%%%%%%%%%%%%%%%%%%%%%%%%%%%%%%%%%%%%%%%%%%%%%%%%%%%
% % Chirp Calculation
% %%%%%%%%%%%%%%%%%%%%%%%%%%%%%%%%%%%%%%%%%%%%%%%%%%%%%%%%%%
%
PhaseOut = unwrap(angle(EtOut));
ChirpOut = diff(PhaseOut)/(DTime);   ChirpOut(NSamp)=0;
```

```
figure;
plot(VTime,ChirpOut*T0,VTime,PowerOut)
legend('Chirpout*T0','PowerOut')
xlabel('Time[S]'),ylabel('Amplitude')
%xlim([-1e-10 1e-10]),ylim([-3 3])
grid on

%%%%%%%%%%%%%%%%%%%%%%%%%%%%%%%%%%%%%%%%%%%%%%%%%%%%%%%%%%%%
% Compression
%%%%%%%%%%%%%%%%%%%%%%%%%%%%%%%%%%%%%%%%%%%%%%%%%%%%%%%%%%%%
L =3200;                                      %Medium length [m]

Alpha_dB = 0.2e-3;                            %Linear attenuation in dB/m
Alpha = 0.1*log(10)*Alpha_dB;
LEff = (1-exp(-Alpha*L))/Alpha; if Alpha <= 1e-4; LEff = L; end

Beta2 =-2.17e-26;            D = -Beta2*(2*pi*c0/Lambda0^2);         %
Beta2_smf = -2.17e-26 s.s/m, D_smf = 17e-6 s/m.m = 17 ps/nm.km
                             %Beta2 = -D/(2*pi*c0/Lambda0^2);
Beta3 = -0*5.2e-43;           S = Beta3*(2*pi*c0/Lambda0^2)^2;        % S_hnlf
= 32 s/m^2.m = 0.032 ps/nm^2.km, Beta3 = 58e-42;
                             %Beta3 = S/(2*pi*c0/Lambda0^2)^2;

% n2 = 0.9e-17;   AEff = 37e-12;
% Gamma = n2*2*pi/(AEff*Lambda0Las);
Gamma = 2e-3;
Nz=20;
[EtOut1,EfOut1] = FoSFMBasic(EtOut,EfOut,DTime,Gamma,Beta2,Beta3,Alpha,L,Nz);


PowerOut1 = Pt(EtOut1);
PsdOut1 = Pf(EfOut1,DFreq);

figure;
subplot(2,1,1),plot(VTime,PowerOut1,'k-')   %VTime,PowerIn,'k-+',
%legend('Before','After')
xlabel('Time[Hz]','fontsize',LFS), ylabel('Power [W]','fontsize',LFS)
title('Temporal output after compression','fontsize',TFS)
xlim([-1e-9 1e-9])
grid on
subplot(2,1,2),plot(VFreq,(PsdIn),'k-',VFreq,(PsdOut1),'k-')
xlim([-1.5e11 1.5e11])
title('Spectrum after compression','fontsize',TFS)
xlabel('Frequency [Hz]','fontsize',LFS), ylabel('PSD [W/Hz]','fontsize',LFS)

%% Parametric Comb generation in HNLF
Gain=1.0;

EtOut1=Gain*EtOut1;
EfOut1=Gain*EfOut1;
```

```
L =1000;                                %Medium length [m]
Nz=20;
Alpha_dB = 1e-3;                        %Linear attenuation in dB/m
Alpha = 0.1*log(10)*Alpha_dB;
LEff = (1-exp(-Alpha*L))/Alpha; if Alpha <= 1e-4; LEff = L; end

Beta2 =+1.595e-28;  %         D = -Beta2*(2*pi*c0/Lambda0^2);         %
Beta2_smf = -2.17e-26 s.s/m, D_smf = 17e-6 s/m.m = 17 ps/nm.km
                            %Beta2 = -D/(2*pi*c0/Lambda0^2);
Beta3 =  0*32.5e-42;%+0*4.0613e-41;           S = Beta3*(2*pi*c0/Lambda0^2)^2;
% S_hnlf = 32 s/m^2.m = 0.032 ps/nm^2.km, Beta3 = 58e-42;
                            %Beta3 = S/(2*pi*c0/Lambda0^2)^2;

% n2 = 0.9e-17;   AEff = 37e-12;
% Gamma = n2*2*pi/(AEff*Lambda0Las);
Gamma = 12e-3;  % 12e-3;

[EtOut2,EfOut2] =
FoSFMBasic(EtOut1,EfOut1,DTime,Gamma,Beta2,Beta3,Alpha,L,Nz);
PowerOut2 = Pt(EtOut2);
PsdOut2 = Pf(EfOut2,DFreq);

figure;
subplot(2,1,1),plot(VTime,PowerOut2,'k-')%,VTime,PowerOut1,'b-')
xlabel('Time','fontsize',LFS), ylabel('Power [W]')
title('Temporal output after Nonlinear Mixing stage','fontsize',TFS)
xlim([-1e-9 1e-9])
grid on
%figure;
subplot(2,1,2),plot(VLambda+Lambda0,dB(PsdOut2/max(PsdOut2)),'b-')
xlabel('Wavelength [um]'),ylabel('Power [dB]')
%plot(VFreq/1e9,dB(PsdOut2),'k-')
%xlabel('Frequency','fontsize',LFS),ylabel('PSD [dB]')
title('Spectrum of Frequency comb','fontsize',TFS)

grid on
```

Appendix B.

Frequency comb generation in optical fiber-2

```
clear all
clc
close all
% SETTINGS
DimEcran = get(0,'ScreenSize');
Dx = 0.40; Dy = 0.7;
PosFig  = [(1-Dx)*DimEcran(3),(0.9-
Dy)*DimEcran(4),Dx*DimEcran(3),Dy*DimEcran(4)];
set(0,'DefaultFigurePosition',PosFig)
AFS = 12;   LFS = 14;   TFS = 18;   %Axis, label and title font size
set(0,'DefaultLineLineWidth',1)

% FUNCTIONS
FT = inline('DTime*fftshift(fft(ifftshift(AtIn)))','AtIn','DTime'); %Fourier
transform
Pf = inline('DFreq*(abs(AfIn)).^2','AfIn','DFreq');                %Power
spectral density (in frequency)
IFT = inline('1/DTime*fftshift(ifft(ifftshift(AfIn)))','AfIn','DTime');
%Inverse Fourier transform
Pt = inline('(abs(AtIn)).^2','AtIn');                              %Power
(in time)
dB=  inline('10*log10(x)','x');

c0 = 3e8;

% Input signal : Clock pulses
Lambda0 = 1550e-9;      Freq0 = c0/Lambda0;         k0 = 2*pi/Lambda0;
Tfwhm = 10e-11;         T0 = Tfwhm/(2*sqrt(log(2)));
RepRate = 10e9;
```

```
Alpha_dB = 0.20e-3;                     %Linear attenuation in dB/m
Alpha = 0.1*log(10)*Alpha_dB;
%LEff = (1-exp(-Alpha*L))/Alpha; if Alpha <= 1e-4; LEff = L; end

Beta2 = -2e-26;            D = -Beta2*(2*pi*c0/Lambda0^2);         % Beta2_smf
= -2.17e-26 s.s/m, D_smf = 17e-6 s/m.m = 17 ps/nm.km
                            %Beta2 = -D/(2*pi*c0/Lambda0^2);
Beta3 = 1*58e-42;           S = Beta3*(2*pi*c0/Lambda0^2)^2;        % S_hnlf =
32 s/m^2.m = 0.032 ps/nm^2.km, Beta3 = 58e-42;
                            %Beta3 = S/(2*pi*c0/Lambda0^2)^2;

PeakPowerIn = 10e-3;        %W  %average CW power


%%%%%%%%%%%%%%%%%%%%%%%%%%%%%%%%%%%%%%%%%%%%%%%%%%%%%%%%%%
% TIME-FREQUENCY VECTORS
%%%%%%%%%%%%%%%%%%%%%%%%%%%%%%%%%%%%%%%%%%%%%%%%%%%%%%%%%%
NSamp = 1e5+1;
DTime = 1e-13;
VTime = (-(NSamp-1)/2:(NSamp-1)/2)'*DTime;
TWindow = NSamp*DTime;

MaxFreq = 0.5/DTime;
DFreq = 2*MaxFreq/(NSamp-1);  % originally was 2
VFreq = (-(NSamp-1)/2:(NSamp-1)/2)'*DFreq;

VLambda = VFreq*Lambda0^2/c0;
%% Modulator Properties
Vpi=3.75;
V0=3.5;
fm=8e9;
wm=2*pi*fm;
U0=PeakPowerIn;
Ut=U0*exp(-1i*pi*(V0/Vpi)*sin(wm*VTime));

Ct=pi*(V0/Vpi)*wm^2*sin(wm*VTime);

L=10400  % Compressive Fiber length

V0=(Vpi/L)/pi/wm^2/Beta2
EtIn=Ut;
PowerIn = Pt(EtIn);
EfIn = FT(EtIn,DTime);
PsdIn = Pf(EfIn,DFreq);                 %W/Hz
MeanPowerFreqTest = trapz(VFreq,PsdIn);
    figure,set(gca,'FontSize',AFS)
    subplot(2,1,1),plot(VTime,PowerIn,'b-')
    title('Temporal signal I/P','fontsize',TFS)
    xlabel('Time [s]','fontsize',LFS), ylabel('Power [W]','fontsize',LFS)
    ylim([0 2*max(PowerIn)]),
    xlim([-1e-11 1e-11])
    subplot(2,1,2),plot(VFreq,dB(PsdIn),'b-')
```

```
    title('Spectrum I/P','fontsize',TFS)
    xlim([-5e11 5e11])
    xlabel('Frequency [Hz]','fontsize',LFS), ylabel('PSD
[W/Hz]','fontsize',LFS)



%%%%%%%%%%%%%%%%%%%%%%%%%%%%%%%%%%%%%%%%%%%%%%%%%%%%%%%%%%%
% PROPAGATION PARAMETERS READINGS
%%%%%%%%%%%%%%%%%%%%%%%%%%%%%%%%%%%%%%%%%%%%%%%%%%%%%%%%%%%
% LD = abs(T0^2/Beta2);
% LN = 1/(Gamma*PeakPowerIn);
% PhiMax = LEff/LN
% N = sqrt(LD/LN)

%%%%%%%%%%%%%%%%%%%%%%%%%%%%%%%%%%%%%%%%%%%%%%%%%%%%%%%%%%%
% Propagating in \smf28 compressive fiber
%%%%%%%%%%%%%%%%%%%%%%%%%%%%%%%%%%%%%%%%%%%%%%%%%%%%%%%%%%%
Nz = 10;                                        % Number of z subdivisions
[EtOut,EfOut] = FoSFMBasic(EtIn,EfIn,DTime,Gamma,Beta2,Beta3,Alpha,L,Nz);

PowerOut = Pt(EtOut);
PsdOut = Pf(EfOut,DFreq);          % W/Hz
PsdOutdBm = 10*log10(125e9*PsdOut/1e-3); % dBm/nm
    figure,set(gca,'FontSize',AFS)
    subplot(2,1,1),plot(VTime,PowerIn,'b-+',VTime,PowerOut,'g-')
   % axis([-2e-10 2e-10 0 1])
    legend('In','Out')
    title('Temporal signal','fontsize',TFS)
    xlabel('Time [s]','fontsize',LFS), ylabel('Power [W]','fontsize',LFS)
    xlim([-1e-10 1e-10])
    ylim([0 max(PowerOut)])
    subplot(2,1,2),plot(VFreq,dB(PsdIn),'b-',VFreq,dB(PsdOut),'g-')
    title('Spectrum','fontsize',TFS)
    xlabel('Frequency [Hz]','fontsize',LFS), ylabel('PSD
[W/Hz]','fontsize',LFS)
    xlim([-5e11 5e11])


%%%%%%%%%%%%%%%%%%%%%%%%%%%%%%%%%%%%%%%%%%%%%%%%%%%%%%%%%%%
% Chirp Calculation
%%%%%%%%%%%%%%%%%%%%%%%%%%%%%%%%%%%%%%%%%%%%%%%%%%%%%%%%%%%

PhaseOut = unwrap(angle(EtOut));
ChirpOut = diff(PhaseOut)/(DTime);   ChirpOut(NSamp)=0;

figure;
plot(VTime,ChirpOut*T0/100,VTime,PowerOut*1000)
legend('Chirpout*T0/5','PowerOut')
xlabel('Time[S]'),ylabel('Amplitude')
xlim([-10e-11 10e-11])
%ylim([-10 10])
```

```
grid on

%%%%%%%%%%%%%%%%%%%%%%%%%%%%%%%%%%%%%%%%%%%%%%%%%%%%%%%%%%%
% Propagation in HNLF 2
%%%%%%%%%%%%%%%%%%%%%%%%%%%%%%%%%%%%%%%%%%%%%%%%%%%%%%%%%%%


edfa=50;                                   % EDFA gaub
L=1000;                                   %Medium length [m]

Alpha_dB = 0.80e-3;                            %Linear attenuation in dB/m
Alpha = 0.1*log(10)*Alpha_dB;
LEff = (1-exp(-Alpha*L))/Alpha; if Alpha <= 1e-4; LEff = L; end

Beta2 =+5.1e-29;
 %Beta2 =+0*0.02e-26;           D = -Beta2*(2*pi*c0/Lambda0^2);         %
Beta2_smf = -2.17e-26 s.s/m, D_smf = 17e-6 s/m.m = 17 ps/nm.km
%                             Beta2 = -D/(2*pi*c0/Lambda0^2);
% Beta3 =  -1*3e-42;          S = Beta3*(2*pi*c0/Lambda0^2)^2;        %
S_hnlf = 32 s/m^2.m = 0.032 ps/nm^2.km, Beta3 = 58e-42;
 Beta3= 3.24e-41;             %Beta3 = S/(2*pi*c0/Lambda0^2)^2;

% n2 = 0.9e-17;   AEff = 37e-12;
% Gamma = n2*2*pi/(AEff*Lambda0Las);
Gamma = 10e-3;

[EtOut2,EfOut2] =
FoSFMBasic(edfa*EtOut,edfa*EfOut,DTime,Gamma,Beta2,Beta3,Alpha,L,Nz);
PowerOut2 = Pt(EtOut2);
PsdOut2 = Pf(EfOut2,DFreq);

figure;
plot(VTime,PowerOut2,'k-+',VTime,PowerOut,'b-')
xlabel('Time[s]'), ylabel('Power [W]')
title('Temporal output after parametric stage')
legend('After','Before')
 xlim([-10e-11 10e-11])
 grid on

figure;
% subplot(2,1,1),plot(VLambda/1e-9+1550,dB(PsdOut2/max(PsdOut2)),'b-')
% xlabel('Wavelength [nm]'),ylabel('PSD [dB]')
% xlim([1530 1570]),ylim([-80 0])
plot(VFreq/1e9,dB(PsdOut2),'b-')
xlabel('Freq [GHz]'),ylabel('PSD [dB]')
title('Spectrum of Parametric comb for Brillouin frequency beating')
% str = {'Input power 600mW','Spacing 10.86 GHz'};
% text(1558,-15,str)
grid on


PhaseOut2 = unwrap(angle(EtOut2));
ChirpOut2 = diff(PhaseOut2)/(DTime);   ChirpOut2(NSamp)=0;
```

```
figure;
plot(VTime,ChirpOut2*T0,VTime,PowerOut2*1000)
legend('Chirpout*T0/5','PowerOut')
xlabel('Time[S]'),ylabel('Amplitude')
xlim([-10e-11 10e-11])
%ylim([-10 10])
grid on

%%%%%%%%%%%%%%%%%%%%%%%%%%%%%%%%%%%%%%%%%%%%%%%%%%%%%%%%%%
% Propagation in second SMF fiber
%%%%%%%%%%%%%%%%%%%%%%%%%%%%%%%%%%%%%%%%%%%%%%%%%%%%%%%%%%
L=200;
Alpha_dB = 0.20e-3;                          %Linear attenuation in dB/m
Alpha = 0.1*log(10)*Alpha_dB;
%LEff = (1-exp(-Alpha*L))/Alpha; if Alpha <= 1e-4; LEff = L; end

Beta2 = -2e-26;            D = -Beta2*(2*pi*c0/Lambda0^2);         % Beta2_smf
= -2.17e-26 s.s/m, D_smf = 17e-6 s/m.m = 17 ps/nm.km
                                %Beta2 = -D/(2*pi*c0/Lambda0^2);
Beta3 = 1*58e-42;           S = Beta3*(2*pi*c0/Lambda0^2)^2;

Gamma=2e-3;
[EtOut3,EfOut3] =
FoSFMBasic(EtOut2,EfOut2,DTime,Gamma,Beta2,Beta3,Alpha,L,Nz);
PowerOut3 = Pt(EtOut3);
PsdOut3 = Pf(EfOut3,DFreq);

figure;
plot(VTime,PowerOut3,'k-+')
xlabel('Time[s]'), ylabel('Power [W]')
title('Temporal output ')
xlim([-10e-11 10e-11])
grid on
figure;

plot(VFreq/1e9,dB(PsdOut3),'b-')
xlabel('Freq [GHz]'),ylabel('PSD [dB]')
title('Spectrum')
grid on

figure;
plot(VLambda+Lambda0,dB(PsdOut3),'b-')
xlabel('Freq [GHz]'),ylabel('PSD [dB]')
title('Spectrum')

%%%%%%%%%%%%%%%%%%%%%%%%%%%%%%%%%%%%%%%%%%%%%%%%%%%%%%%%%%
% Propagation in HNLF 3
%%%%%%%%%%%%%%%%%%%%%%%%%%%%%%%%%%%%%%%%%%%%%%%%%%%%%%%%%%

edfa=1.0;
L=200;                            %Medium length [m]
```

```
Alpha_dB = 0.80e-3;                      %Linear attenuation in dB/m
Alpha = 0.1*log(10)*Alpha_dB;
LEff = (1-exp(-Alpha*L))/Alpha; if Alpha <= 1e-4; LEff = L; end

Beta2 =+5.1e-29;

Beta3= 1*3.24e-42;              %Beta3 = S/(2*pi*c0/Lambda0^2)^2;
Gamma = 13e-3;
[EtOut4,EfOut4] =
FoSFMBasic(edfa*EtOut3,edfa*EfOut3,DTime,Gamma,Beta2,Beta3,Alpha,L,Nz);
PowerOut4 = Pt(EtOut4);
PsdOut4 = Pf(EfOut4,DFreq);

figure;
plot(VTime,PowerOut4,'k-+',VTime,PowerOut,'b-')
xlabel('Time[s]'), ylabel('Power [W]')
title('Temporal output after parametric stage')
legend('After','Before')
 xlim([-10e-11 10e-11])
 grid on

figure;

plot(VFreq/1e9,dB(PsdOut4),'b-')
xlabel('Freq [GHz]'),ylabel('PSD [dB]')
title('Spectrum of Parametric comb for Brillouin frequency beating')

grid on

figure;
plot(VLambda+Lambda0,dB(PsdOut4)+100,'b-')
xlim([1534e-9 1566e-9])
xlabel('Wavelength [m]'),ylabel('Power [dB]')
title('Spectrum')

wavelength=VLambda+Lambda0;
spectrum=dB(PsdOut4)+100; % normalization
```

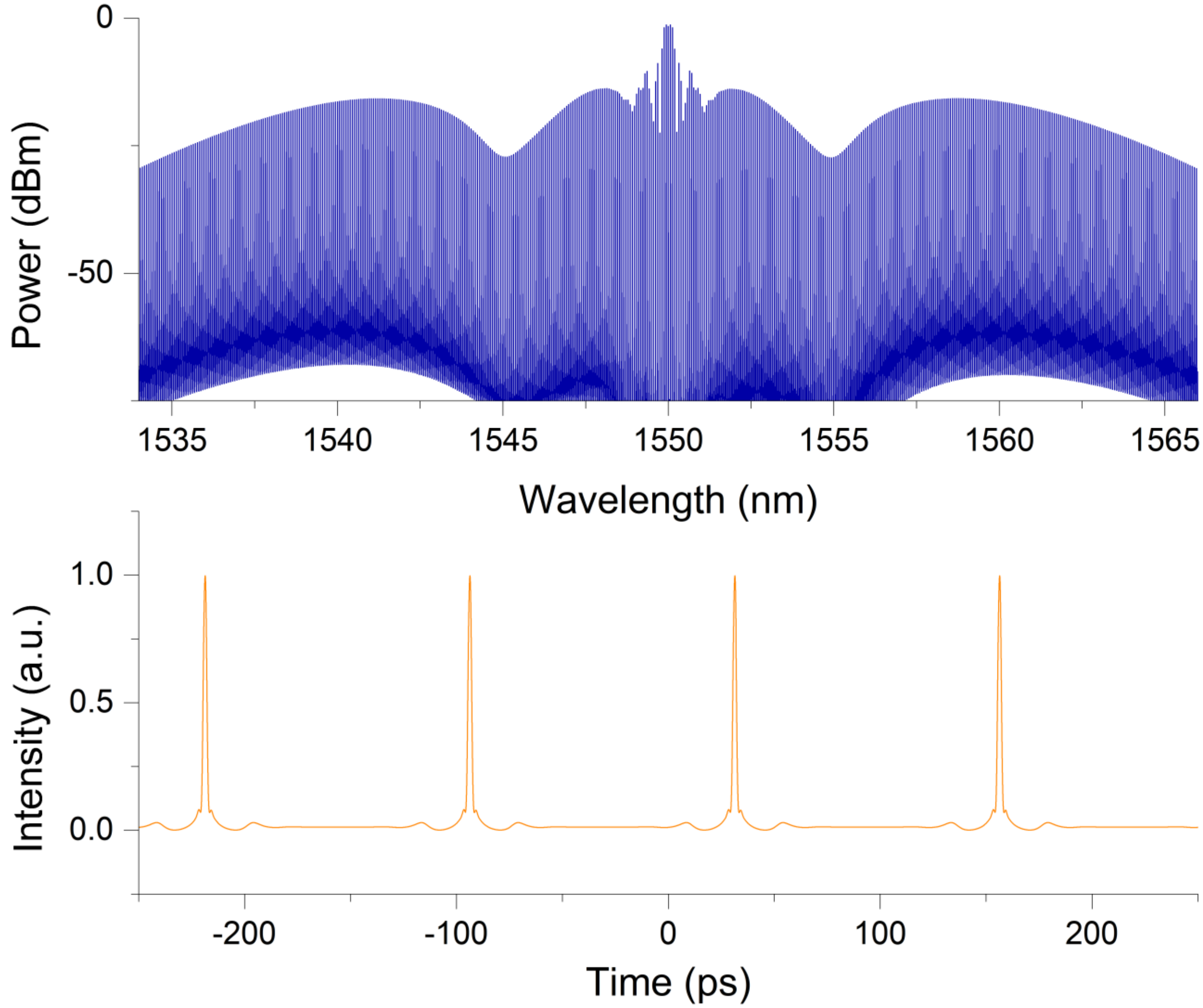

Figure B1. Simulated spectrum and time-domain representation of an EO frequency comb, generated by the experimental setup shown in figure 2.6.

Appendix C.

Simulation of the transmittance of a fiber Fabry–Pérot filter

```
clc
clear all
close all

lambda=linspace(1549.9995e-9,1550.0005e-9,2000);
c=3e8;
lambda_ctr=1550e-9;
freq=c./lambda;


n=1.5;
alpha=0.2e-3/4.343;
l=5;

del=2*n*l*2*pi./lambda;



R=0.5*exp(-(alpha*l));
F=4*R/(1-R)^2;
T=1./(1+F*(sin(del/2)).^2); % Transmittance.

figure
plot((freq-mean(freq))/1e6,(T),'linewidth',2)
xlabel('Frequency [MHz]'); ylabel('Transmittance')
title('Transmittance of FP cavity')
```

```
set(gca, "linewidth", 4, "fontsize", 20)
```

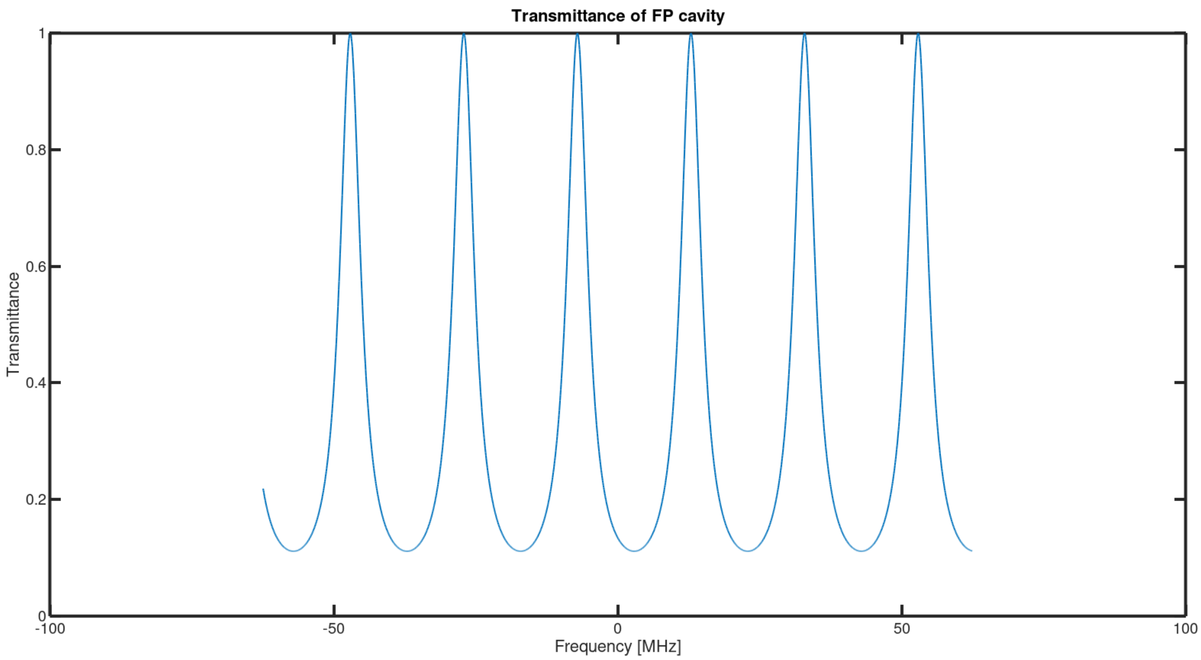

Figure C1. Transmittance of a fiber Fabry–Pérot filter.

Bibliography

1. J. Ye and S. T. Cundiff, *Femtosecond Optical Frequency Comb: Principle, Operation and Applications* (Springer Science & Business Media, 2005).

2. T. Udem, J. Reichert, R. Holzwarth, and T. W. Hänsch, "Absolute optical frequency measurement of the cesium D 1 line with a mode-locked laser," Phys. Rev. Lett. **82**, 3568 (1999).

3. A. Cingöz, D. C. Yost, T. K. Allison, A. Ruehl, M. E. Fermann, I. Hartl, and J. Ye, "Direct frequency comb spectroscopy in the extreme ultraviolet," Nature **482**, 68 (2012).

4. G. B. Rieker, F. R. Giorgetta, W. C. Swann, J. Kofler, A. M. Zolot, L. C. Sinclair, E. Baumann, C. Cromer, G. Petron, C. Sweeney, P. P. Tans, I. Coddington, and N. R. Newbury, "Frequency-comb-based remote sensing of greenhouse gases over kilometer air paths," Optica **1**, 290 (2014).

5. S. Fukushima, C. F. C. Silva, Y. Muramoto, and A. J. Seeds, "Optoelectronic Millimeter-Wave Synthesis Using an Optical Frequency Comb Generator, Optically Injection Locked Lasers, and a Unitraveling-Carrier Photodiode," J. Light. Technol. **21**, 3043 (2003).

6. J. Pfeifle, V. Brasch, M. Lauermann, Y. Yu, D. Wegner, T. Herr, K. Hartinger, P. Schindler, J. Li, D. Hillerkuss, R. Schmogrow, C. Weimann, R. Holzwarth, W. Freude, J. Leuthold, T. J. Kippenberg, and C. Koos, "Coherent terabit communications with microresonator Kerr frequency combs," Nat Phot. **8**, 375–380 (2014).

7. D. J. Jones, S. A. Diddams, J. K. Ranka, A. Stentz, R. S. Windeler, J. L. Hall, and S. T. Cundiff, "Carrier-Envelope Phase Control of Femtosecond Mode-Locked Lasers and Direct Optical Frequency Synthesis," Science (80-.). **288**, 635 LP – 639 (2000).

8. W. E. Lamb, "Theory of an Optical Maser," Phys. Rev. **134**, A1429–A1450 (1964).

9. F. C. Cruz, D. L. Maser, T. Johnson, G. Ycas, A. Klose, F. R. Giorgetta, I. Coddington, and S. A. Diddams, "Mid-infrared optical frequency combs based on difference frequency generation for molecular spectroscopy," Opt. Express **23**, 26814–26824 (2015).

10. N. Leindecker, A. Marandi, R. L. Byer, and K. L. Vodopyanov, "Broadband degenerate OPO for mid-infrared frequency comb generation," Opt. Express **19**, 6296–6302 (2011).

11. T. Herr, V. Brasch, J. D. Jost, C. Y. Wang, N. M. Kondratiev, M. L. Gorodetsky, and T. J. Kippenberg, "Temporal solitons in optical microresonators," Nat. Photonics **8**, 145 (2013).

12. S. T. Cundiff and J. Ye, "\textit{Colloquium} : Femtosecond optical frequency combs," Rev. Mod. Phys. **75**, 325–342 (2003).

13. A. Schliesser, N. Picque, and T. W. Hansch, "Mid-infrared frequency combs," Nat Phot. **6**, 440–449 (2012).

14. H. A. Haus, "Mode-locking of lasers," IEEE J. Sel. Top. Quantum Electron. **6**, 1173–1185 (2000).

15. M. A. Solodyankin, E. D. Obraztsova, A. S. Lobach, A. I. Chernov, A. V Tausenev, V. I. Konov, and E. M. Dianov, "Mode-locked 1.93 μm thulium fiber laser with a carbon nanotube absorber," Opt. Lett. **33**, 1336–1338 (2008).

16. R. L. Carman, R. Y. Chiao, and P. L. Kelley, "Observation of Degenerate Stimulated Four-Photon Interaction and Four-Wave Parametric Amplification," Phys. Rev. Lett. **17**, 1281–1283 (1966).

17. R. Stolen, "Phase-matched-stimulated four-photon mixing in silica-fiber waveguides," IEEE J. Quantum Electron. **11**, 100–103 (1975).

18. G. Agrawal, "Chapter 10 - Four-Wave Mixing," in *Optics and Photonics*, G. B. T.-N. F. O. (Fifth E. Agrawal, ed. (Academic Press, 2013), pp. 397–456.

19. P. Del'Haye, A. Schliesser, O. Arcizet, T. Wilken, R. Holzwarth, and T. J. Kippenberg, "Optical frequency comb generation from a monolithic microresonator," Nature **450**, 1214–1217 (2007).

20. P. Del'Haye, T. Herr, E. Gavartin, M. L. Gorodetsky, R. Holzwarth, and T. J.

Kippenberg, "Octave Spanning Tunable Frequency Comb from a Microresonator," Phys. Rev. Lett. **107**, 63901 (2011).

21. V. Ataie, B. P.-P. Kuo, E. Myslivets, and S. Radic, "Generation of 1500-tone, 120nm-wide ultraflat frequency comb by single CW source," Opt. Fiber Commun. Conf. Fiber Opt. Eng. Conf. 2013 PDP5C.1 (2013).

22. Z. Tong, A. O. J. Wiberg, E. Myslivets, B. P. P. Kuo, N. Alic, and S. Radic, "Spectral linewidth preservation in parametric frequency combs seeded by dual pumps," Opt. Express **20**, 17610–17619 (2012).

23. E. Myslivets, B. P. P. Kuo, N. Alic, and S. Radic, "Generation of wideband frequency combs by continuous-wave seeding of multistage mixers with synthesized dispersion," Opt. Express **20**, 3331 (2012).

24. L. Huo, H. Li, D. Wang, Q. Wang, and C. Lou, "Multiwavelength 25-GHz picosecond pulse generation with phase modulation and double-side Mamyshev reshaping," Appl. Opt. **54**, 5703 (2015).

25. G. Millot, S. Pitois, M. Yan, and T. Hovannysyan, "Frequency-agile dual-comb spectroscopy," Nat. Photonics **10**, 27–30 (2016).

26. V. Durán, P. A. Andrekson, and V. Torres-Company, "Electro-optic dual-comb interferometry over 40 nm bandwidth," Opt. Lett. **41**, 4190–4193 (2016).

27. G. Agrawal, "Chapter 4 - Self-Phase Modulation," in *Optics and Photonics*, G. B. T.-N. F. O. (Fifth E. Agrawal, ed. (Academic Press, 2013), pp. 87–128.

28. L. Brillouin, "Diffusion de la lumière et des rayons X par un corps transparent homogène-Influence de l’agitation thermique," in *Annales de Physique* (EDP Sciences, 1922), Vol. 9, pp. 88–122.

29. A. Debut, S. Randoux, and J. Zemmouri, "Linewidth narrowing in Brillouin lasers: Theoretical analysis," Phys. Rev. A **62**, 1–4 (2000).

30. M. I. Kayes and M. Rochette, "Optical frequency comb generation via cascaded Brillouin scattering in a nonlinear media," in *Photonics North*, *2015* (2015), p. 1.

31. C Chatfield, "The Analysis of Time Series—An Introduction," in *The Analysis of Time Series—An Introduction (Fourth Ed.)*, 4th ed. (Chapman and Hall, 1989), pp. 94–95.

32. A. L. Oldenburg, J. J. Reynolds, D. L. Marks, and S. A. Boppart, "Fast-Fourier-domain delay line for in vivo optical coherence tomography with a polygonal scanner," Appl. Opt. **42**, 4606–4611 (2003).

33. T. Hochrein, R. Wilk, M. Mei, R. Holzwarth, N. Krumbholz, and M. Koch, "Optical sampling by laser cavity tuning.," Opt. Express **18**, 1613–1617 (2010).

34. L. Yang, J. Nie, and L. Duan, "Dynamic optical sampling by cavity tuning and its application in lidar," Opt. Express **21**, 3850–3860 (2013).

35. H. Wu, F. Zhang, T. Liu, F. Meng, J. Li, and X. Qu, "Absolute distance measurement using optical sampling by cavity tuning," IEEE Photonics Technol. Lett. **28**, 1275–1278 (2016).

36. K. Lee, J. Lee, Y.-S. Jang, S. Han, H. Jang, Y.-J. Kim, and S.-W. Kim, "Fourier-transform spectroscopy using an Er-doped fiber femtosecond laser by sweeping the pulse repetition rate," Sci. Rep. **5**, 15726 (2015).

37. G. Horlick, "Introduction to Fourier Transform Spectroscopy," Appl. Spectrosc. **22**, 617–626 (1968).

38. B. Bernhardt, J. Mandon, P. Jacquet, M. Jacquey, A. Ozawa, R. Holzwarth, G. Guelachvili, G. Hänsch, and N. Picqué, "Laser frequency combs for molecular fingerprinting," in *2009 IEEE LEOS Annual Meeting Conference Proceedings* (IEEE, 2009), pp. 619–620.

39. I. Coddington, N. Newbury, and W. Swann, "Dual-comb spectroscopy," Optica **3**, 414 (2016).

40. E. Temprana, E. Myslivets, B. P.-P. Kuo, L. Liu, V. Ataie, N. Alic, and S. Radic, "Overcoming Kerr-induced capacity limit in optical fiber transmission," Science (80-.). **348**, 1445–1448 (2015).

41. N. Alic, E. Myslivets, E. Temprana, B. P.-P. Kuo, and S. Radic, "Nonlinearity Cancellation in Fiber Optic Links Based on Frequency Referenced Carriers," J. Light. Technol. **32**, 2690–2698 (2014).

42. E. Temprana, E. Myslivets, B. P.-P. Kuo, L. Liu, V. Ataie, N. Alic, and S. Radic, "Overcoming Kerr-induced capacity limit in optical fiber transmission," Science (80-.). **348**, 1445 LP – 1448 (2015).

43. T. Udem, R. Holzwarth, and T. W. Hänsch, "Optical frequency metrology.," Nature **416**, 233–237 (2002).

44. S. A. Diddams, "The evolving optical frequency comb [Invited]," J. Opt. Soc. Am. B **27**, B51–B62 (2010).

45. H. Murata, A. Morimoto, T. Kobayashi, and S. Yamamoto, "Optical pulse generation by electrooptic-modulation method and its application to integrated ultrashort pulse

generators," IEEE J. Sel. Top. Quantum Electron. **6**, 1325–1331 (2000).

46. V. Ataie, E. Myslivets, B. P. P. Kuo, N. Alic, and S. Radic, "Spectrally equalized frequency comb generation in multistage parametric mixer with nonlinear pulse shaping," J. Light. Technol. **32**, 840–846 (2014).

47. R. Wu, V. Torres-Company, D. E. Leaird, and A. M. Weiner, "Supercontinuum-based 10-GHz flat-topped optical frequency comb generation," Opt. Express **21**, 6045–6052 (2013).

48. J. Zhao, C. Zhang, Z. Ji, C. Miao, H. Gu, Z. Tong, X. Sun, and J. Bai, "Widely tunable ultra-narrow linewidth single-longitudinal-mode Brillouin fiber laser with low threshold," Laser Phys. **24**, 105102 (2014).

49. J. Zhang, C.-Y. Yue, G. W. Schinn, W. R. L. Clements, and J. W. Y. Lit, "Stable single-mode compound-ring erbium-doped fiber laser," J. Light. Technol. **14**, 104–109 (1996).

50. Y. Cheng, J. T. Kringlebotn, W. H. Loh, R. I. Laming, and D. N. Payne, "Stable single-frequency traveling-wave fiber loop laser with integral saturable-absorber-based tracking narrow-band filter," Opt. Lett. **20**, 875–877 (1995).

51. Y. Peng, "A Novel Scheme for Hundred-Hertz Linewidth Measurements with the Self-Heterodyne Method," Chinese Phys. Lett. **30**, 084208 (2013).

52. Dennis Derickson, *Fiber Optic Test and Measurement* (Prentice Hall, 1997).

53. Keysight Technologies, "81940A Compact Tunable Laser Source with Continuous Sweep Mode, 1520nm to 1630nm," https://www.keysight.com/en/pd-1281761-pn-81940A/compact-tunable-laser-source-with-continuous-sweep-mode-1520nm-to-1630nm?pm=PL&nid=-32364.740611&cc=CA&lc=eng.

54. S. Huang, T. Zhu, Z. Cao, M. Liu, M. Deng, J. Liu, and X. Li, "Laser linewidth measurement based on amplitude difference comparison of coherent envelope," IEEE Photonics Technol. Lett. **28**, 759–762 (2016).

55. A. Ishizawa, T. Nishikawa, A. Mizutori, H. Takara, A. Takada, T. Sogawa, and M. Koga, "Phase-noise characteristics of a 25-GHz-spaced optical frequency comb based on a phase- and intensity-modulated laser," Opt. Express **21**, 1343–1344 (2013).

56. S. D. Saliba and R. E. Scholten, "Linewidths below 100 kHz with external cavity diode lasers," Appl. Opt. **48**, 6961–6966 (2009).

57. B. P. P. Kuo, E. Myslivets, V. Ataie, E. G. Temprana, N. Alic, and S. Radic, "Wideband Parametric Frequency Comb as Coherent Optical Carrier," J. Light. Technol. **31**, 3414–3419 (2013).

58. M. I. Kayes and M. Rochette, "Low noise frequency comb generator," in *2016 Photonics North (PN)* (IEEE, 2016), p. Nonlinear-10-6.

59. W. Gao, S.-W. Kim, H. Bosse, H. Haitjema, Y. L. Chen, X. D. Lu, W. Knapp, A. Weckenmann, W. T. Estler, and H. Kunzmann, "Measurement technologies for precision positioning," CIRP Ann. **64**, 773–796 (2015).

60. N. R. Newbury, "Searching for applications with a fine-tooth comb," Nat. Photonics **5**, 186–188 (2011).

61. K. Minoshima and H. Matsumoto, "High-accuracy measurement of 240-m distance in an optical tunnel by use of a compact femtosecond laser," Appl. Opt. **39**, 5512–5517 (2000).

62. M. Cui, M. G. Zeitouny, N. Bhattacharya, S. A. Van den Berg, H. P. Urbach, and J. J. M. Braat, "High-accuracy long-distance measurements in air with a frequency comb laser," Opt. Lett. **34**, 1982–1984 (2009).

63. S. H. and Y.-J. K. and Y. K. and J. J. and S.-W. Kim, "Absolute length measurement with the frequency comb of a femtosecond laser," Meas. Sci. Technol. **20**, 95302 (2009).

64. S. A. van den Berg, S. T. Persijn, G. J. P. Kok, M. G. Zeitouny, and N. Bhattacharya, "Many-Wavelength Interferometry with Thousands of Lasers for Absolute Distance Measurement," Phys. Rev. Lett. **108**, 183901 (2012).

65. I. Coddington, W. C. Swann, L. Nenadovic, and N. R. Newbury, "Rapid and precise absolute distance measurements at long range," Nat. Photonics **3**, 351 (2009).

66. H. Wu, T. Zhao, Z. Wang, K. Zhang, B. Xue, J. Li, M. He, and X. Qu, "Long distance measurement up to 1.2 km by electro-optic dual-comb interferometry," Appl. Phys. Lett. **111**, 251901 (2017).

67. M. Imrul Kayes and M. Rochette, "Fourier transform spectroscopy by repetition rate sweeping of a single electro-optic frequency comb," Opt. Lett. **43**, 967–970 (2018).

68. S. Boudreau and J. Genest, "Range-resolved vibrometry using a frequency comb in the OSCAT configuration," Opt. Express **22**, 8101–8113 (2014).

69. L. Yang and L. Duan, "Depth-resolved imaging based on optical sampling by cavity tuning," IEEE Photonics Technol. Lett. **27**, 1761–1764 (2015).

70. H. W. U. Anzhong, F. U. Z. Hang, T. I. L. Iu, P. E. T. R. B. Alling, and J. L. I. Ianshuang, "Long distance measurement using optical sampling by cavity tuning," **41**, 2366–2369 (2016).

71. M. Imrul Kayes and M. Rochette, "Optical frequency comb generation with ultra-narrow

spectral lines," Opt. Lett. **42**, 2718–2721 (2017).

72. B. Xue, Z. Wang, K. Zhang, J. Li, and H. Wu, "Absolute distance measurement using optical sampling by sweeping the repetition frequency," Opt. Lasers Eng. **109**, 1–6 (2018).

73. H. Wu, F. Zhang, T. Liu, P. Balling, J. Li, and X. Qu, "Long distance measurement using optical sampling by cavity tuning," Opt. Lett. **41**, 2366–2369 (2016).

74. S. A. Diddams, L. Hollberg, and V. Mbele, "Molecular fingerprinting with the resolved modes of a femtosecond laser frequency comb," Nature **445**, 627–630 (2007).

75. T. Ideguchi, A. Poisson, G. Guelachvili, N. Picqué, and T. W. Hänsch, "Adaptive real-time dual-comb spectroscopy," Nat. Commun. **5**, 21932–21939 (2014).

76. A. J. Fleisher, D. A. Long, Z. D. Reed, J. T. Hodges, and D. F. Plusquellic, "Coherent cavity-enhanced dual-comb spectroscopy," Opt. Express **24**, 10424 (2016).

77. G. Millot, S. Pitois, M. Yan, T. Hovhannisyan, A. Bendahmane, T. W. Hänsch, and N. Picqué, "Frequency-agile dual-comb spectroscopy," Nat. Photonics **10**, 27–30 (2015).

78. C. Mohr, A. Romann, A. Ruehl, I. Hartl, and M. E. Fermann, "Fourier Transform Spectrometry Using a Single Cavity Length Modulated Mode-Locked Fiber Laser," in *Advances in Optical Materials*, OSA Technical Digest (CD) (Optical Society of America, 2011), p. FWA2.

79. S. Potvin, S. Boudreau, J.-D. Deschênes, and J. Genest, "Fully referenced single-comb interferometry using optical sampling by laser-cavity tuning.," Appl. Opt. **52**, 248–55 (2013).

80. R. Wilk, T. Hochrein, M. Koch, M. Mei, and R. Holzwarth, "OSCAT : Novel Technique for Time-Resolved Experiments Without Moveable Optical Delay Lines pulse source," 596–602 (2011).

81. M. Imrul Kayes and M. Rochette, "Optical frequency comb generation with ultra-narrow spectral lines," Opt. Lett. **42**, 2718–2721 (2017).

82. P. Martín-Mateos, B. Jerez, and P. Acedo, "Dual electro-optic optical frequency combs for multiheterodyne molecular dispersion spectroscopy," Opt. Express **23**, 21149–21158 (2015).

83. Wavelength References, "C-Band Wavelength Calibrator Hydrogen Cyanide Gas Cell H 13C 14N," http://www.wavelengthreferences.com/pdf/Data HCN.pdf.

84. J. E. Román, M. Y. Frankel, and R. D. Esman, "Spectral characterization of fiber gratings with high resolution," Opt. Lett. **23**, 939–941 (1998).

85. P. Balling, K. Petr, P. Mašika, and S. A. Van Den Berg, "Femtosecond frequency comb based distance measurement in air," **17**, 9300–9313 (2009).

86. H. Wu, F. Zhang, T. Liu, and X. Qu, "Glass thickness and index measurement using optical sampling by cavity tuning," Appl. Opt. **55**, 9756 (2016).

87. L. Yang, L. Yang, and L. Duan, "Depth-Resolved Imaging Based on Optical Sampling by Cavity Tuning Depth-Resolved Imaging Based on Optical Sampling by Cavity Tuning," IEEE Photonics Technol. Lett. **27**, 1761–1764 (2015).

88. I. Coddington, W. C. Swann, and N. R. Newbury, "Coherent multiheterodyne spectroscopy using stabilized optical frequency combs," Phys. Rev. Lett. **100**, 11–14 (2008).

89. E. M. Waxman, K. C. Cossel, G.-W. Truong, F. R. Giorgetta, W. C. Swann, I. Coddington, and N. R. Newbury, "Dual Frequency Comb Spectroscopy for Trace Gas Monitoring Over Open-Air Paths," in *Light, Energy and the Environment*, OSA Technical Digest (Online) (Optical Society of America, 2017), p. ETu1B.2.

90. I. Coddington, W. C. Swann, and N. R. Newbury, "Coherent dual-comb spectroscopy at high signal-to-noise ratio," Phys. Rev. A - At. Mol. Opt. Phys. **82**, 1–13 (2010).

91. H. S. and F.-L. H. Sho Okubo, Kana Iwakuni , Hajime Inaba , Kazumoto Hosaka, Atsushi Onae, "Ultra-broadband dual-comb spectroscopy across 1.0–1.9 µm," Appl. Phys. Express **8**, 82402 (2015).

92. D. A. Long, A. J. Fleisher, K. O. Douglass, S. E. Maxwell, K. Bielska, J. T. Hodges, and D. F. Plusquellic, "Multiheterodyne spectroscopy with optical frequency combs generated from a continuous-wave laser," Opt. Lett. **39**, 2688 (2014).

93. P. Martin-Mateos, M. Ruiz-Llata, J. Posada-Roman, and P. Acedo, "Dual-Comb Architecture for Fast Spectroscopic Measurements and Spectral Characterization," IEEE Photonics Technol. Lett. **27**, 1309–1312 (2015).

94. J. Roy, J.-D. Deschênes, S. Potvin, and J. Genest, "Continuous real-time correction and averaging for frequency comb interferometry," Opt. Express **20**, 21932–21939 (2012).

95. S. Mehravar, R. A. Norwood, N. Peyghambarian, and K. Kieu, "Real-time dual-comb spectroscopy with a free-running bidirectionally mode-locked fiber laser," Appl. Phys. Lett. **108**, 1–6 (2016).

96. T. Ideguchi, T. Nakamura, Y. Kobayashi, and K. Goda, "Kerr-lens mode-locked bidirectional dual-comb ring laser for broadband dual-comb spectroscopy," Optica **3**, 748 (2016).

97. X. Zhao, G. Hu, B. Zhao, C. Li, Y. Pan, Y. Liu, T. Yasui, and Z. Zheng, "Picometer-resolution dual-comb spectroscopy with a free-running fiber laser," Opt. Express **24**, 21833 (2016).

98. R. Liao, Y. Song, W. Liu, H. Shi, L. Chai, and M. Hu, "Dual-comb spectroscopy with a single free-running thulium-doped fiber laser," Opt. Express **26**, 11046–11054 (2018).

99. I. Coddington, N. Newbury, and W. Swann, "Dual-comb spectroscopy," Optica **3**, 414–426 (2016).

100. H. S. and F.-L. H. Sho Okubo, Kana Iwakuni , Hajime Inaba , Kazumoto Hosaka, Atsushi Onae, "Ultra-broadband dual-comb spectroscopy across 1.0–1.9 µm," Appl. Phys. Express **8**, 82402 (2015).

101. N. Abdukerim, M. I. Kayes, A. Rekik, and M. Rochette, "Bidirectional mode-locked thulium-doped fiber laser," Appl. Opt. **57**, 7198–7202 (2018).

102. I. Gordon, L. Rothman, C. Hill, R. Kochanov, Y. Tan, P. Bernath, V. Boudon, A. Campargue, B. Drouin, J. M. Flaud, R. Gamache, J. Hodges, V. Perevalov, K. Shine, and M. Smith, "The HITRAN2016 Molecular Spectroscopic Database," J. Quant. Spectrosc. Radiat. Transf. **6**, 3–69 (2017).